NASA CONTRACTOR REPORT




NASA CR-720

# EXPERIMENTAL CASSEGRAIN-FED MONOPULSE ANTENNA SYSTEM

*by R. T. Clark and P. A. Jensen*

*Prepared by*
HUGHES AIRCRAFT COMPANY
Fullerton, Calif.
*for Goddard Space Flight Center*

NATIONAL AERONAUTICS AND SPACE ADMINISTRATION • WASHINGTON, D. C. • MAY 1967

NASA CR-720

# EXPERIMENTAL CASSEGRAIN-FED MONOPULSE ANTENNA SYSTEM

By R. T. Clark and P. A. Jensen



Prepared under Contract No. NAS 5-9880 by
HUGHES AIRCRAFT COMPANY
Fullerton, Calif.

for Goddard Space Flight Center

NATIONAL AERONAUTICS AND SPACE ADMINISTRATION

For sale by the Clearinghouse for Federal Scientific and Technical Information
Springfield, Virginia 22151 – Price $3.25

## ABSTRACT

The purpose of this program was to design a five horn monopulse feed with ultimate capability of high efficiency, low noise performance at both 6 and 4 GHz when utilized in a Cassegrain antenna. The program covered feed component design, fabrication of a feed capable of operation at 4 GHz, and design and assembly of a 15-foot Cassegrain antenna using a dish supplied by NASA. A principal item of the study was detailed primary and secondary measurements to evaluate the feed performance.

A technique of making five horn feeds was developed which is a definite advancement in the state of the art. A feed capable of providing greater than 50 percent efficiency at both 6 and 4 GHz, monopulse tracking at 4 GHz, and low antenna noise temperature was developed.

It is recommended that this approach be utilized to design a feed capable of operation at both 6 and 4 GHz and evaluated in a larger (30 foot diameter or larger) Cassegrain antenna.

CONTENTS

LIST OF ILLUSTRATIONS

LIST OF ILLUSTRATIONS (Continued)

LIST OF TABLES

# 1.0 INTRODUCTION

## 1.1 PURPOSE

The purpose of this study was to develop a five horn feed with the utlimate capability of efficient simultaneous operation at 6 GHz for transmit and at 4 GHz for receive and monpulse tracking which can be used in a cassegrain antenna system.

## 1.2 SUMMARY OF WORK PERFORMED

The work accomplished during this study included the following tasks:

(1) A five horn feed was designed and fabricated that operates over the minimum frequency band, 3990 – 4210 MHz, and uses all five horns for the receive sum channel, the outer four horns for the error channels and ultimately the center horn for transmitting at 6 GHz.

(2) The feed system was integrated with a 15-foot paraboloidal reflector having an F/D = .40 and secondary characteristics were evaluated.

(3) A low noise parametric amplifier was designed and fabricated.

(4) The parametric amplifier was integrated and thoroughly checked out with the cassegrain antenna system and the noise temperature of the antenna was measured.

(5) A technique of producing rotatable linear polarization was experimentally demonstrated.

# 2.0 FIVE HORN FEED

## 2.1 FEED DESCRIPTION

The feed developed under this study has the ultimate capability of efficient simultaneous operation at 6 GHz for transmit and at 4 GHz for receive and monopulse tracking. The final feed package, shown in Figure 1, delivered under this contract includes only the 4 GHz capability and operates over the band 3900 – 4300 MHz. Experimental evidences discussed in Section 2.5 demonstrates the ultimate capability of operation at 6 GHz for transmit.

The aperture consists of five horns. The receive sum channel aperture utilizes all five horns. The four outside horns form the aperture for the two error channels. Transmitting at 6 GHz uses only the center horn aperture. Control of the aperture size of the individual horns, and amplitude and phase at the common aperture of the five horns resulted in an average beamwidth at 6 GHz from the center horn equal to the average beamwdith at 4 GHz from all five horns. Further detailed analysis of the aperture is discussed in Section 2.2.

The feed circuitry consists of a power divider feeding a diagonal plane monopulse bridge and a center horn. Five circular polarizers are used to convert to right circular polarization. The various combining operations of the circuitry are shown in Figure 2 where the normalizing coefficients are dropped. The bridge combines the signals from the four outside horns to form the two error channels and a sum. The power divider adds the signal from the center horn after it has been properly phased to the sum signal from the bridge to obtain the receive sum channel. The necessary components of the feed circuitry and their operation are discussed in detail in Section 2.3.

The feed package was sealed at the flanges using cho-seals or RTV 102 in specially milled grooves in the flanges. The horns were sealed using a thin sheet of mylar at the common aperture. The measured leakage rate with the feed pressurized at 0.5 psi (gage) was 0.25 $ft^3/hr$.

All components of the feed are painted with a white epoxy paint (laminar X-500).

The overall length of the feed from the radome to the sum channel output is 52 inches. The weight of the assembled feed is 130 lbs.

## 2.2 APERTURE

The ultimate capability of efficient simultaneous operation at 6 GHz for transmit and at 4 GHz for receive and monopulse tracking depends directly on the ability to control the amplitude distribution and phase at the common aperture of the five

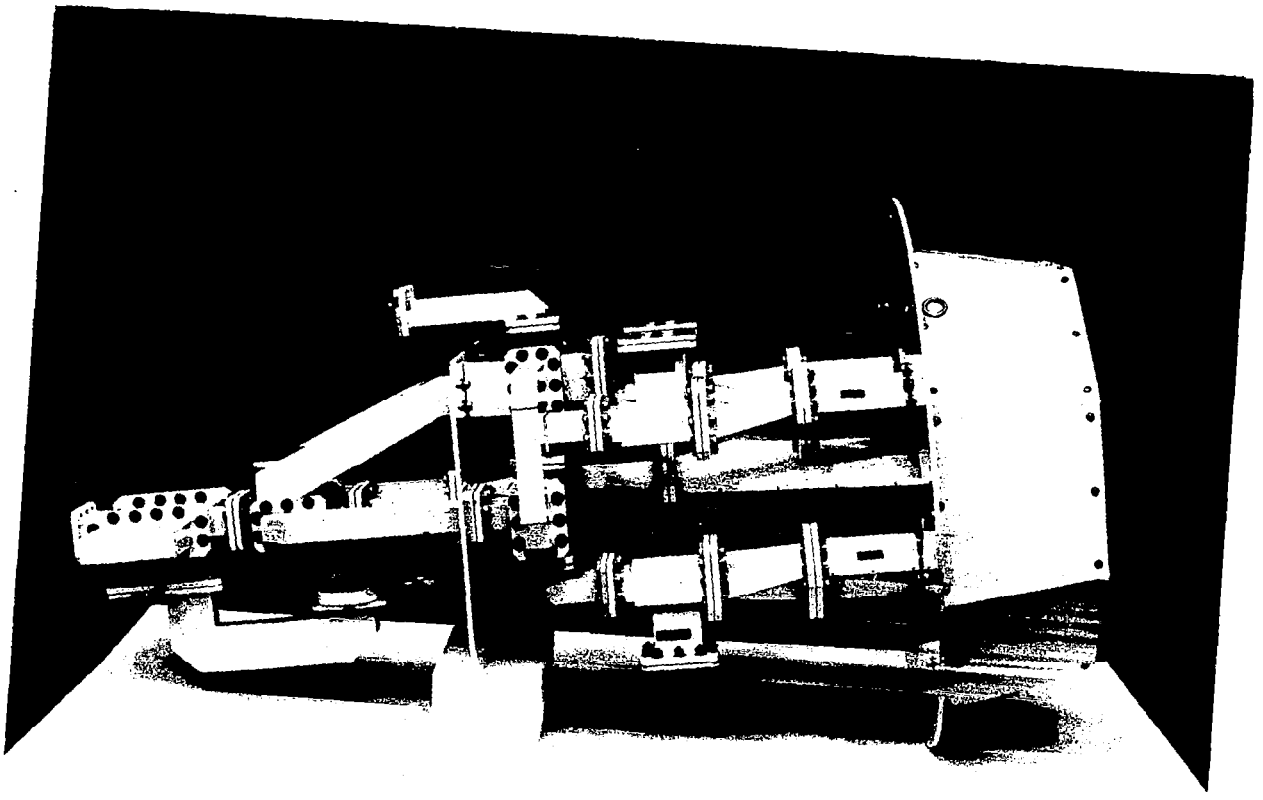

Figure 1. Final 4 GHz Feed System

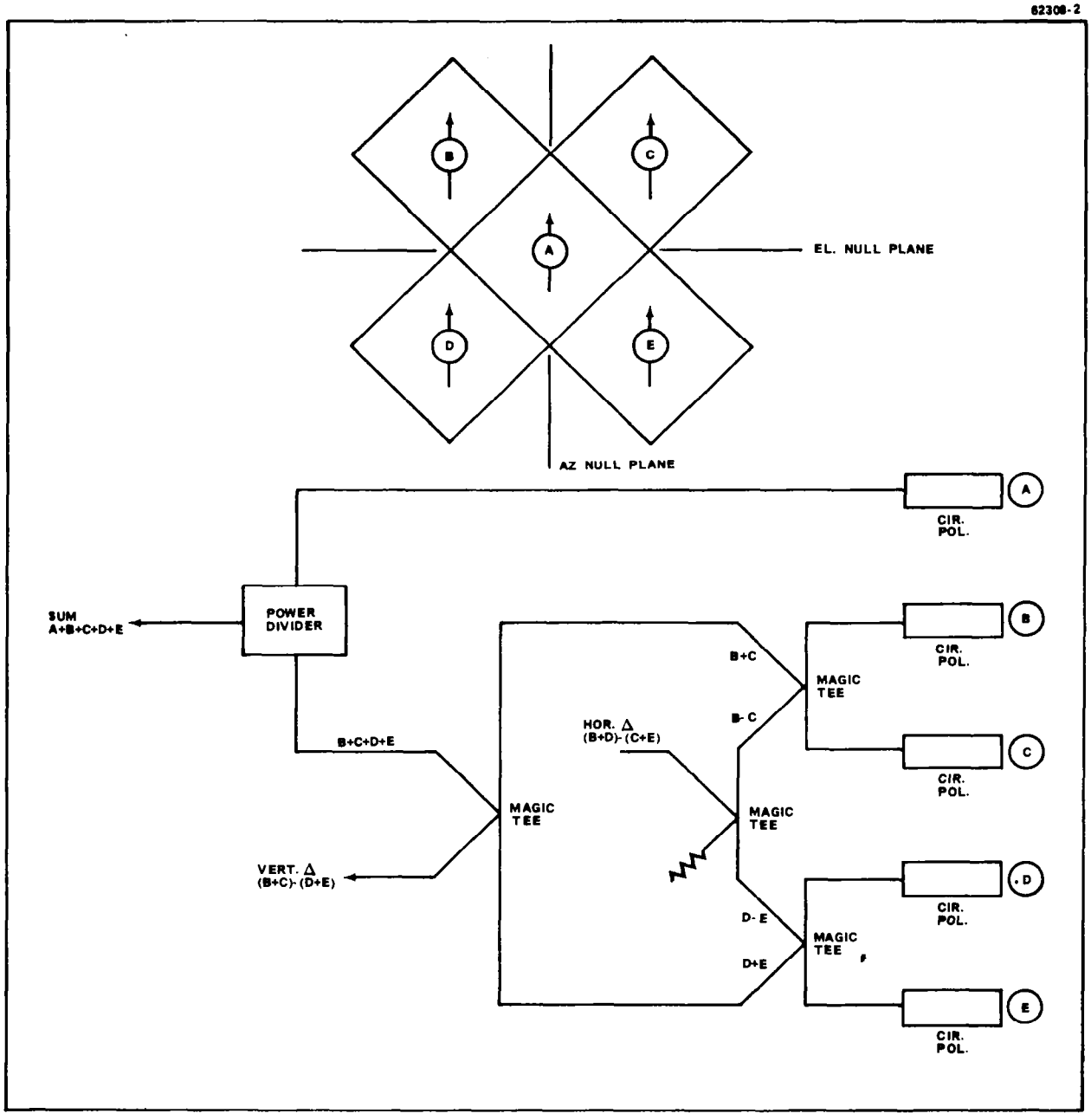


Figure 2. Diagonal Plane Monopulse Feed Circuitry

horns. The difficulty arises from having to equalize the beamwidths for two frequencies that have a ratio of 3:2 from apertures that have a ratio of 3:1, resulting in a beamwidth ratio of 2:1. The wide variation in amplitude distribution of the various planes complicates the problem further. These problems are in addition to obtaining low sidelobe levels, constant phase across the main beam, etc.

After considerable theoretical and experimental investigation, the most promising approach taken was to consider the aperture as an array of five elements. To investigate this technique, a computer program was set up to calculate the radiation patterns of a given horn configuration (Figure 3) for the parameters; "E" (ratio of E field amplitude in the outside horns to the amplitude in the center horn), "D" (center-to-center spacing between center and outside horns), "S" (aperture size of outside horns), and "A" (aperture size of center horn). For polarization along the diagonal of the horns, the element factor for the outside horns is given approximately in all planes by:

$$E_o = \left(\frac{S}{\lambda}\right)^2 \left[\frac{\sin \frac{v}{\sqrt{2}}}{\frac{v}{\sqrt{2}}}\right]\left[\frac{\cos \frac{v}{\sqrt{2}}}{1 - \frac{2v^2}{\pi^2}}\right] \qquad (1)$$

where

$$v = \frac{kS}{2} \sin \theta$$

and for the center horn by:

$$E_c = \left(\frac{A}{\lambda}\right)^2 \left[\frac{\sin \frac{w}{\sqrt{2}}}{\frac{w}{\sqrt{2}}}\right]\left[\frac{\cos \frac{W}{\sqrt{2}}}{1 - \frac{2v^2}{\pi^2}}\right] \qquad (2)$$

where

$$w = \frac{kA}{2} \sin \theta$$

The array factor for a general field distribution in the diagonal planes may be expressed as follows:

$$A_D = E_c + 2E_o + E_o \left[\exp (jkD \sin \theta) + \exp (-jkD \sin \theta)\right]$$

letting

$$u = \frac{kD}{2} \sin \theta$$

then

$$A_D = E_c + 2 E_o (1 + \cos 2u) \qquad (3)$$

In the principal planes,

$$A_P = E_c + 2E_o \left[\exp (jkD \sin\theta/\sqrt{2}) + \exp (-jkD \sin \theta/\sqrt{2})\right]$$

or

$$A_P = E_c + 4\,E_o \cos\sqrt{2}u \tag{4}$$

Combining the array and element factors, normalizing and setting $E_c = 1$, the resulting equations are:

Diagonal Plane

$$E_D = \left[ 2E\left(\frac{S}{\lambda}\right)^2 (1 + \cos 2u)\, \frac{\sin\frac{v}{\sqrt{2}}}{\frac{v}{\sqrt{2}}}\, \frac{\cos\frac{v}{\sqrt{2}}}{1 - \frac{2v^2}{\pi^2}} + \left(\frac{A}{\lambda}\right)^2 \frac{\sin\frac{w}{\sqrt{2}}}{\frac{w}{\sqrt{2}}}\, \frac{\cos\frac{w}{\sqrt{2}}}{1 - \frac{2w^2}{\pi^2}} \right] \cdot \left[ \frac{1}{4E\left(\frac{S}{\lambda}\right)^2 + \left(\frac{A}{\lambda}\right)^2} \right] \tag{5}$$

Principal Plane

$$E_P = \left[ 4E\left(\frac{S}{\lambda}\right)^2 \cos\sqrt{2}u\, \frac{\sin\frac{v}{\sqrt{2}}}{\frac{v}{\sqrt{2}}}\, \frac{\cos\frac{v}{\sqrt{2}}}{1 - \frac{2v^2}{\pi^2}} + \left(\frac{A}{\lambda}\right)^2 \frac{\sin\frac{w}{\sqrt{2}}}{\frac{w}{\sqrt{2}}}\, \frac{\cos\frac{w}{\sqrt{2}}}{1 - \frac{2w^2}{\pi^2}} \right] \vdots \left[ \frac{1}{4E\left(\frac{S}{\lambda}\right)^2 + \left(\frac{A}{\lambda}\right)^2} \right] \tag{6}$$

Center Horn

$$E_c = \left[ \frac{\sin\frac{w}{\sqrt{2}}}{\frac{w}{\sqrt{2}}} \right] \left[ \frac{\cos\frac{w}{\sqrt{2}}}{1 - \frac{2w^2}{\pi^2}} \right] \tag{7}$$

Radiation patterns were computed for a number of configurations including some that were physically unrealizable (horn apertures overlap). Radiation patterns of a configuration (although physically unrealizable) that appeared to produce an efficient feed are shown in Figures 4 through 6. This configuration was approximated as shown in Figure 7. An X-band five horn feed model was fabricated to this configuration and sum radiation patterns measured. Adjustment of the parameters for the best performance resulted in patterns as shown in Figures 8 through 13. It is interesting to note the close correlation between the computed patterns and the measured patterns of the approximating configuration. Pattern integration was made for this configuration to determine the feed spillover efficiency. The results appear in Table 1. This configuration has resulted in an aperture capable of efficient simultaneous operation at 6 GHz for transmit and 4 GHz for receive and monopulse tracking.

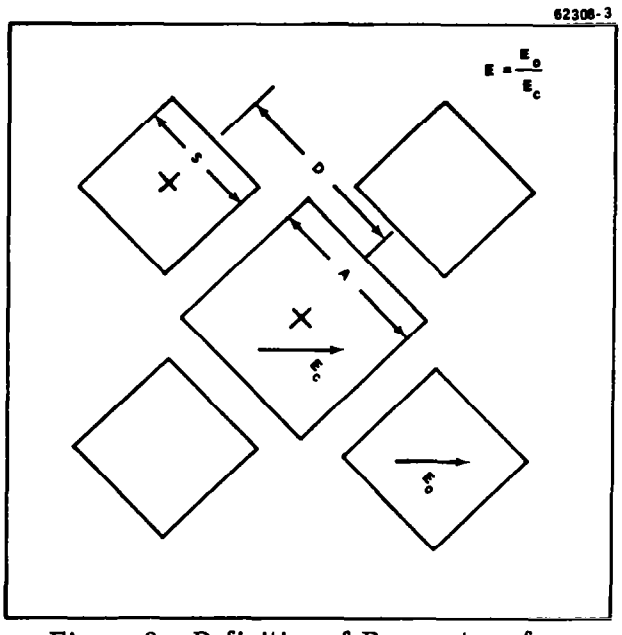


Figure 3. Definition of Parameters for Computer Analysis

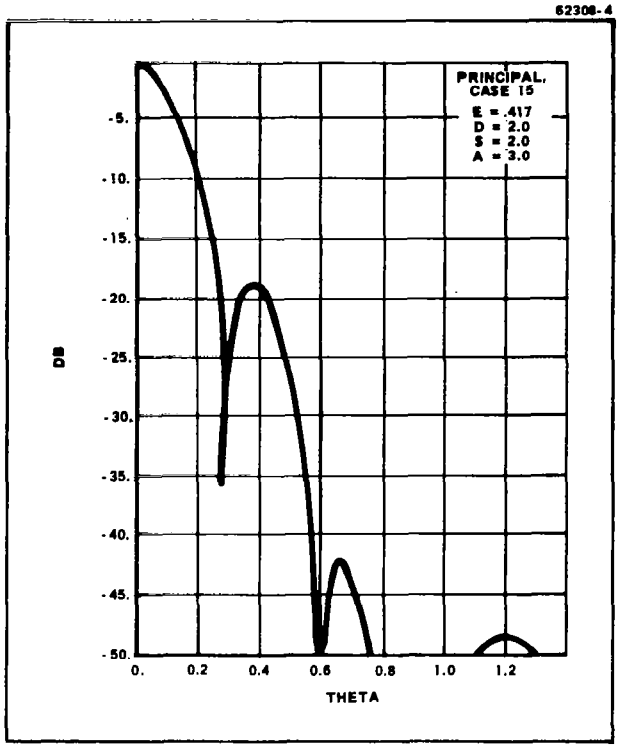


Figure 4. Theoretical Radiation Pattern of Five Horn Feed, Principal Plane

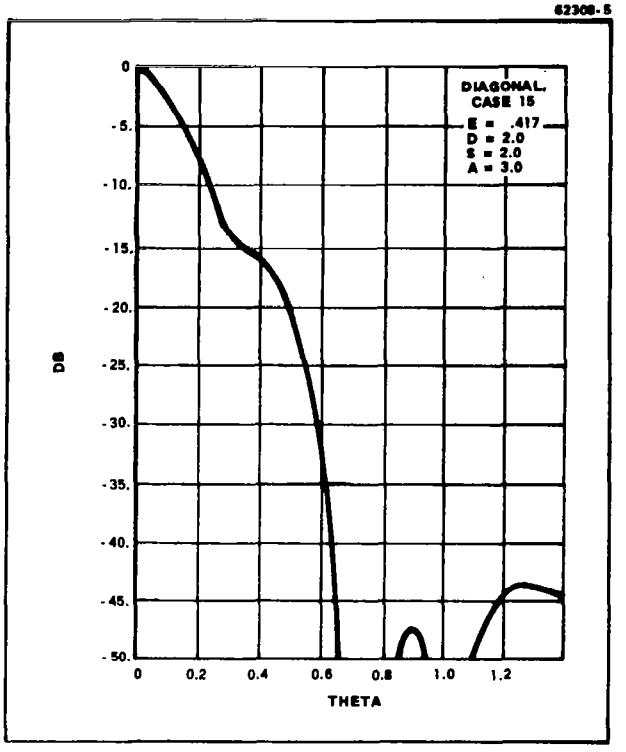


Figure 5. Theoretical Radiation Pattern of Five Horn Feed, Diagonal Plane

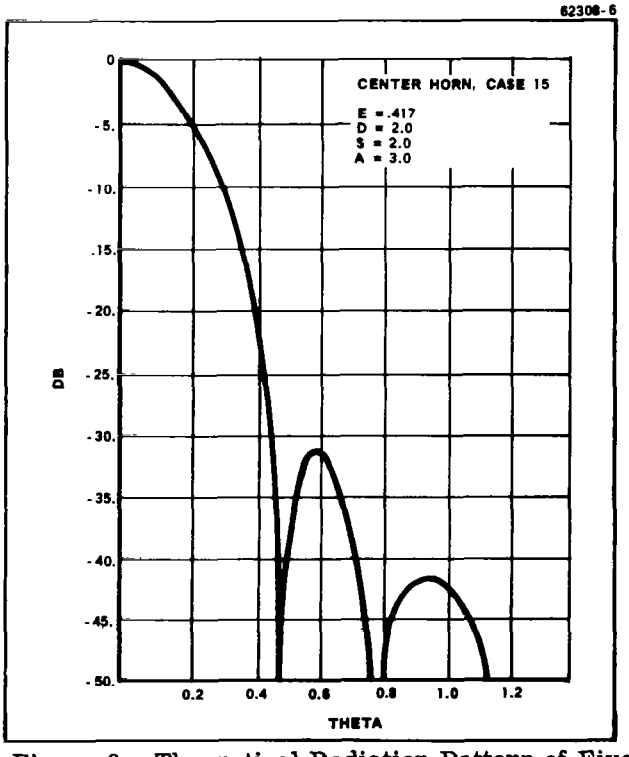


Figure 6. Theoretical Radiation Pattern of Five Horn Feed, Center Horn Only

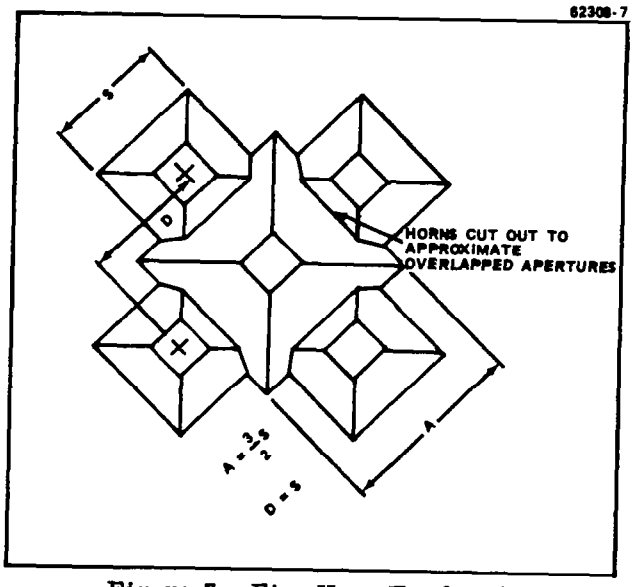


Figure 7. Five Horn Feed with Overlapped Apertures

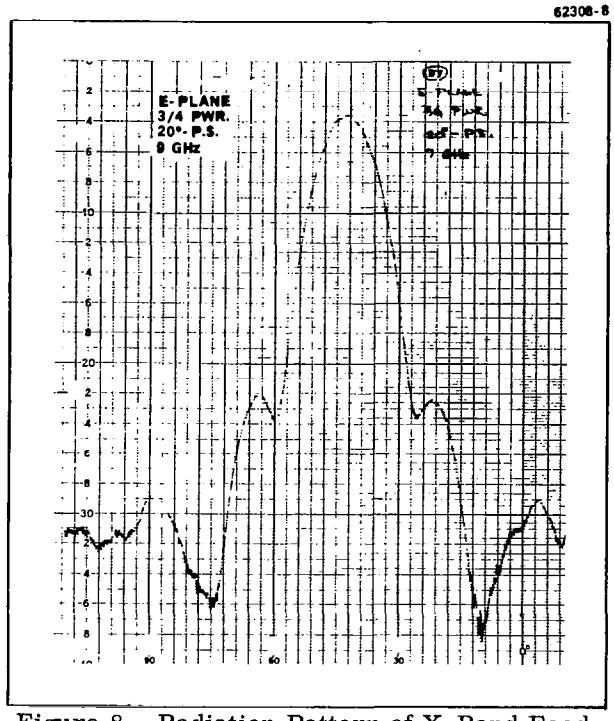


Figure 8. Radiation Pattern of X-Band Feed Model, E-Plane

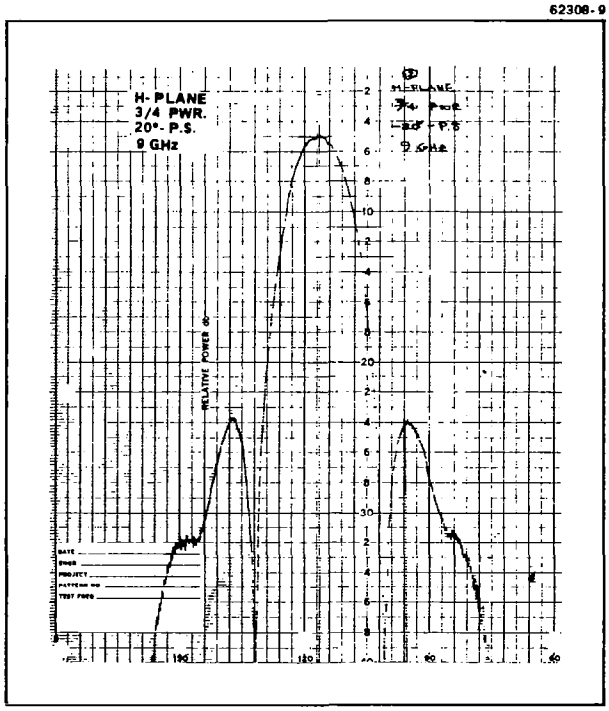


Figure 9. Radiation Pattern of X-Band Feed Model, H-Plane

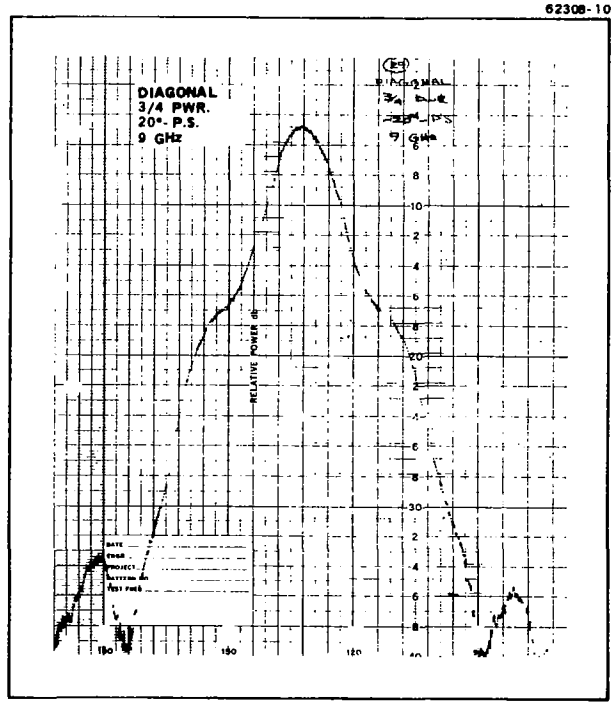


Figure 10. Radiation Pattern of X-Band Feed Model, Diagonal Plane

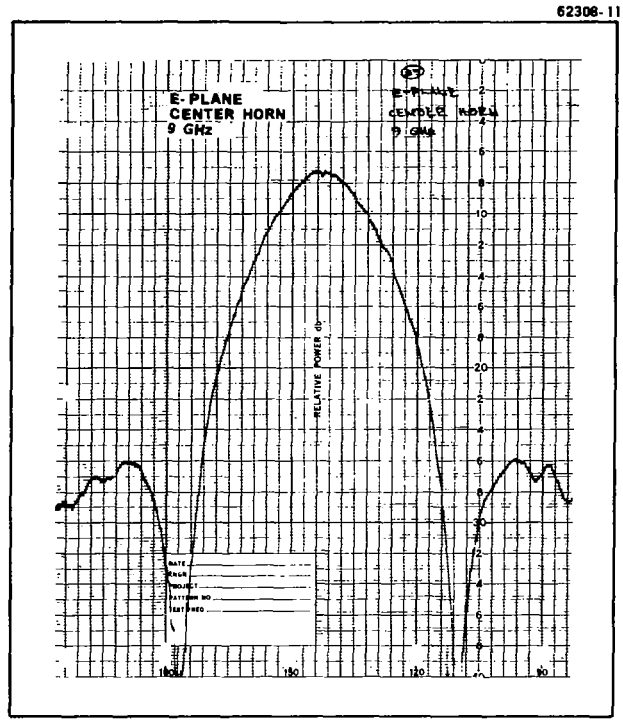


Figure 11. Radiation Pattern of X-Band Feed Model, Center Horn, E-Plane

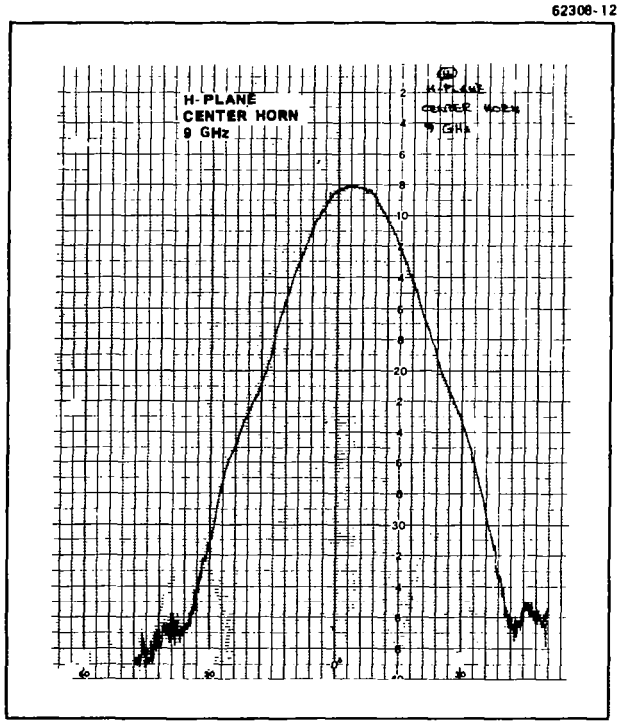


Figure 12. Radiation Pattern of X-Band Feed Model, Center Horn, H-Plane

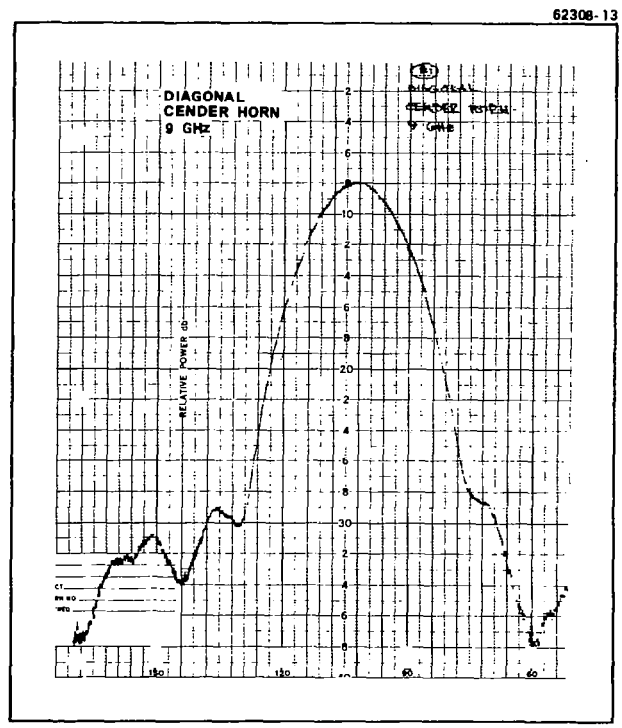


Figure 13. Radiation Pattern of X-Band Feed Model, Center Horn, Diagonal Plane

TABLE 1. FEED SPILLOVER EFFICIENCY X-BAND MODEL

| Configuration | Energy Within 12 dB BW – 9 GHz<br>Ave. of E, H, and Diagonal Planes | Corresponding Energy Intercepted by Hyperboloid at 13.5 GHz<br>Ave. of E, H, and Diagonal Planes |
|---|---|---|
| $A = \frac{3}{2} S$ | | |
| $D = S$ | 76.5 percent | 77.4 percent |
| $\frac{E_o}{E_c} = .289$ | | |

Since the feed is to be used in a cassegrain system, it was necessary to determine whether a phase center existed and to locate its position. Phase center measurements were made at 8 GHz on the X-band five horn feed model with the use of a serrodyne phase bridge. The phase center of the sum channel in each of the three planes – E, H, and Diagonal – was measured and typical sum channel phase patterns are shown in Figures 14 through 16. In all three planes the apparent phase center was within ±1 inch of the common aperture plane. Since the difference channel utilizes only the four outer horns, it was necessary to locate its phase center to determine if it was significantly different from that of the sum channel.

Phase center measurements show that the difference channel phase center lies (Figure 17) between 0 and 1/2 inch behind the aperture plane. Specific data on the phase center of both the sum and difference channels appears in Table 2. At 4 GHz the phase center can be considered to be at the aperture.

TABLE 2. PHASE CENTER MEASUREMENT ON X-BAND FEED MODEL AT 8 GHz

| Sum Channel | Phase Center |
|---|---|
| E | 0 to 1" F* |
| H | 0 to 1" B** |
| Diag | 3/4 to 1-1/4" F |
| Difference Channel | |
| -- | 0 - 1/2" B |

*F – in front of common aperture
**B – in back of common aperture

Further measurements – cross polarization, difference channel radiation patterns, etc. – were made on the X-Band model to evaluate the overall performance of this configuration. Based on the performance of the X-Band feed model, an aperture design capable of efficient simultaneous operation at two frequencies that have a ratio of 3:2 has been achieved. The design of the 4 GHz aperture was based on this configuration.

The 4 GHz feed package was designed to minimize the length of the feed extending behind the rear mounting plate of the reflector. As the feed is moved forward,

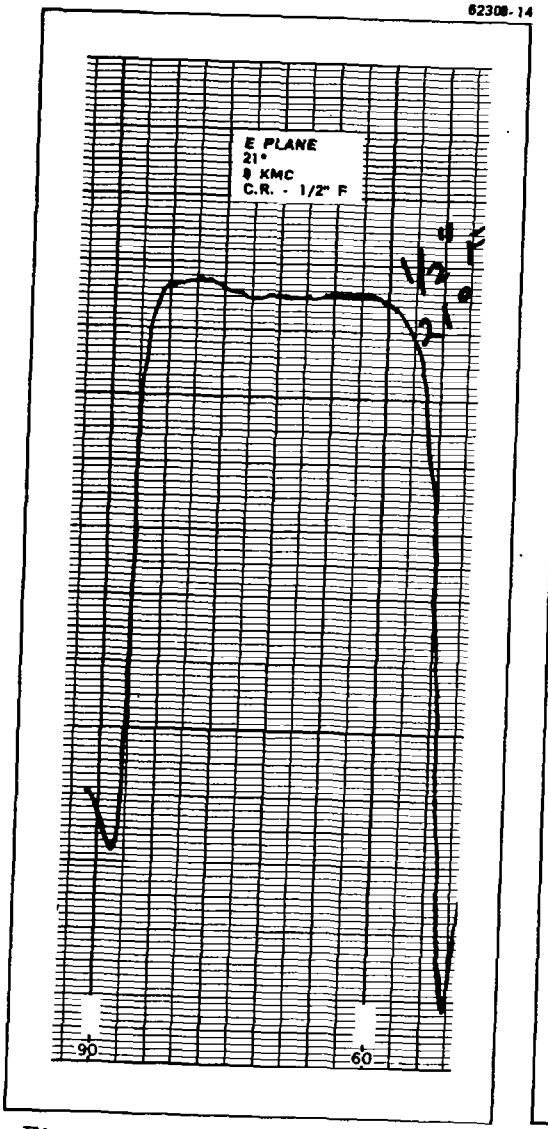


Figure 14. E-Plane Sum Channel Phase Pattern

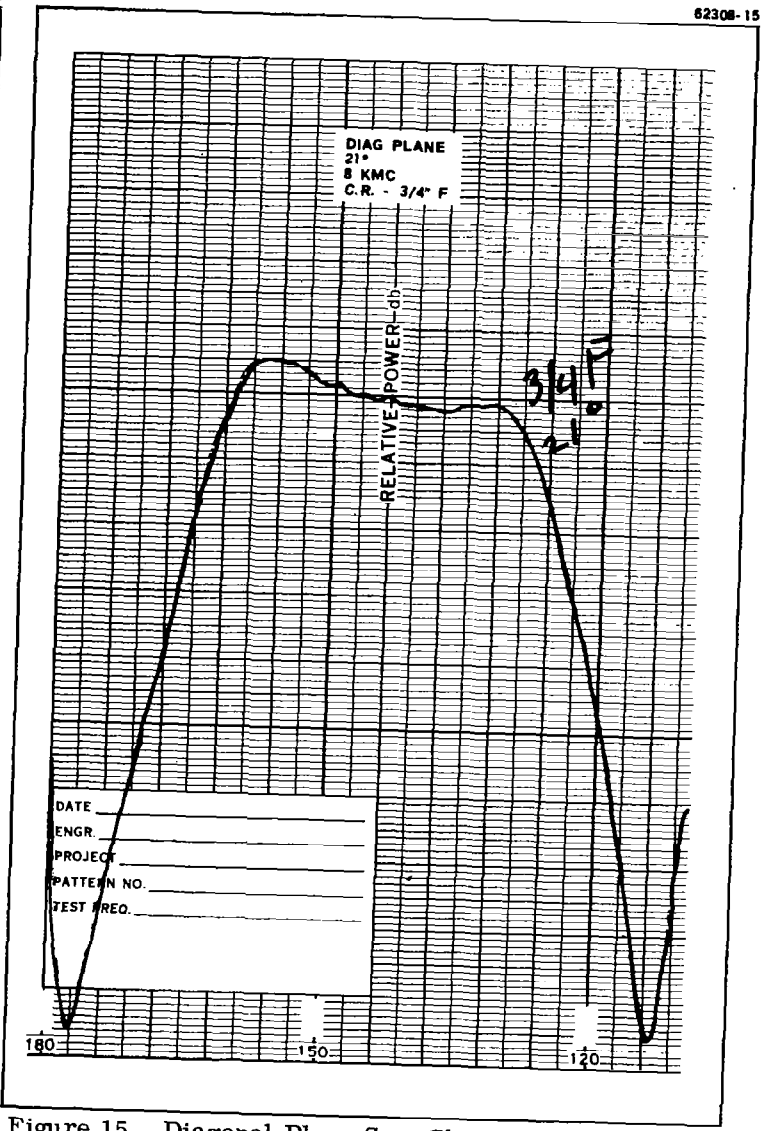


Figure 15. Diagonal Plane Sum Channel Phase Pattern

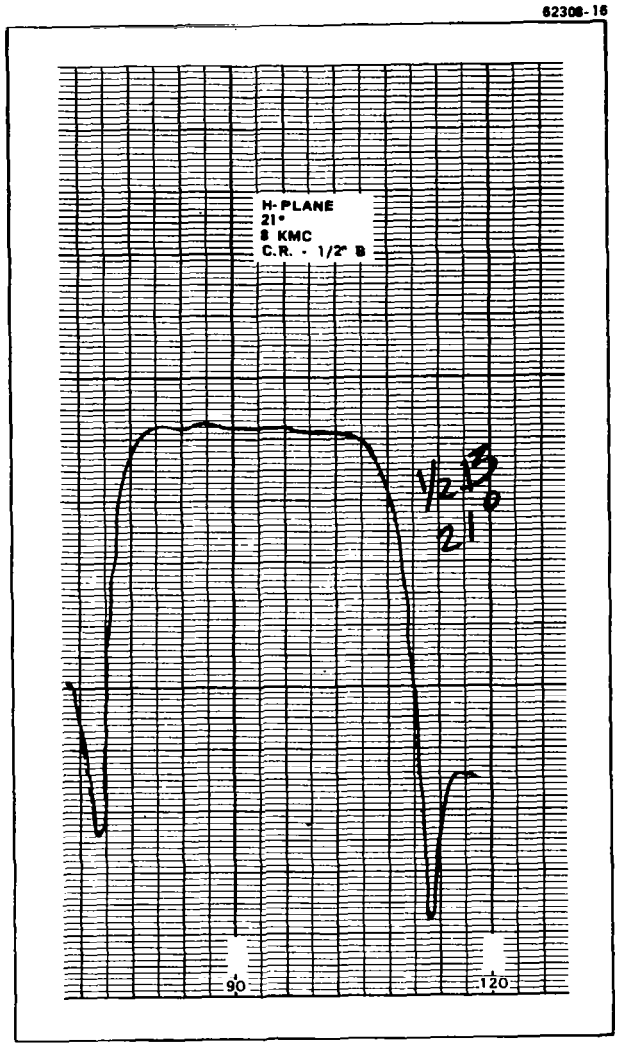


Figure 16. H-Plane Sum Channel Phase Pattern

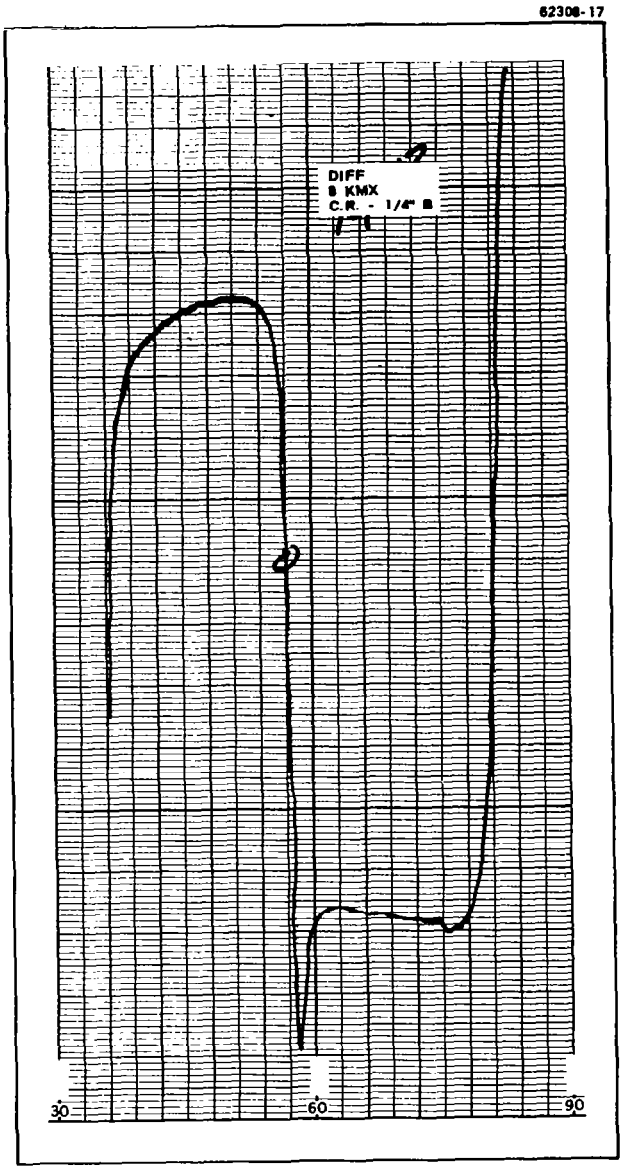


Figure 17. Difference Channel Phase Pattern

the spacing between the monopulse bridge orthomodes feeding the horns decreases. The minimum spacing which could be obtained is 8.260 inches. This results in a center-to-center spacing, "D", (referring to Figure 3) of 5.840 inches. Following the design configuration of Figure 7, the outer horn aperture size, "S", is 5.840 inches and the center horn aperture size, "A", is 8.760 inches. The resultant overall aperture size is 17.520 inches which gives a beamwidth of 23.8 degrees. Continuing the attempt to minimize any extension of the feed past the hub, the horns were designed as short as possible. This was accomplished by specifying a maximum phase error of an eighth of a wavelength at 4100 MHz across the aperture of each of the five horns. If the center horn had been designed for 6 GHz, the length would have to be longer than if designed at 4 GHz, and would have defeated the attempt to minimize the feed length. The complete design of the 4 GHz aperture is tabulated in Table 3.

TABLE 3. 4 GHz APERTURE DESIGN

| | Center Horn | Outer Horn |
|---|---|---|
| Aperture Size | 8.760" | 5.840" |
| Flare Angle | $9.46^{o}$ | $14.27^{o}$ |
| Length | 20.591" | 7.746" |
| | Overall aperture size = 17.520" | |
| | Beamwidth = $23.8^{o}$ | |

## 2.3 FEED COMPONENTS

### 2.3.1 ORTHOMODE TRANSDUCER

The orthomode transducer (OMT) is a four terminal microwave device consisting of two rectangular waveguide inputs (normal and orthogonal arms) and a square waveguide output that supports the two orthogonal modes – $TE_{10}$ and $TE_{01}$. The higher order modes must be suppressed for proper operation of the OMT. The next higher order modes that are usually encountered are the $TE_{11}$ and $TM_{11}$. The cutoff wavelength for these modes is given by:

$$\lambda_{c11} = \sqrt{2}\, a \qquad (8)$$

where

$\lambda_{c11}$ = cutoff wavelength

a = dimension of square waveguide

To insure suppression of these modes over the entire design bandwidth, "a" must be less than the dimension that would just cut off these modes at the high frequency extreme of the design bandwidth – 3900 to 4300 MHz. At 4300 MHz,

$a_{c11} = 1.941$ inches.

At the same time, the square waveguide must not cut off the $TE_{10}$ and $TE_{01}$ modes of the low frequency extreme of the design bandwidth. This condition is

$a_{c10} = 1.531$ inches

at 3900 MHz. The final choice of the square waveguide dimension which must lie between 1.941 and 1.531 inches is based on the following factors:

1. Resistive loss increases as the cut off dimension for the $TE_{10}$ is approached.
2. Difficulty in matching over a bandwidth increases as the cut off dimension for the $TE_{10}$ is approached.
3. Since this dimension will be the throat dimension of the horns, the mismatch of the horns will be high if "a" is close to the cutoff dimension of the $TE_{10}$. The large mismatch would result from a rapid change in the guide wavelength at the throat of the horns.
4. If the $TE_{10}$ is forced close to cut off, the guide wavelength becomes sensitive to the "a" dimension; the total phase shift through the OMT is more likely to vary from unit to unit and the location of matching elements become more critical which requires undesirable tightening of mechanical tolerances.

These criteria resulted in a square waveguide dimension of 1.900 inches for operation over the frequency band 3900 – 4300 MHz. The 4 GHz OMT is shown in Figure 18. The resulting isolation between the normal and orthogonal arms is better than 40 dB and typical data on VSWR is given in Table 4.

TABLE 4. VSWR FOR 4 GHz OMT

| Frequency (MHz) | Normal Arm | Ortho Arm |
|---|---|---|
| 3900 | 1.09 | 1.11 |
| 4000 | 1.08 | 1.04 |
| 4100 | 1.04 | 1.08 |
| 4200 | 1.04 | 1.06 |
| 4300 | 1.02 | 1.07 |

### 2.3.2 CIRCULAR POLARIZER

The circular polarizer converts the linear polarized wave from the square waveguide output of the monopulse bridge into right hand circular polarization. Circular polarization is characterized by two fields that are in space and time quadrature. Space quadrature was obtained from a transistion from square waveguide to a 45 degree rotated square waveguide (see Figure 19). With the incident polarization at 45 degrees to the sides of the output square waveguide, the output fields consist of two space orthogonal modes – $TE_{10}$ and $TE_{01}$ – as shown in Figure 20. Time quadrature was obtained by periodically loading one of these modes with capacitive elements. Broadband operation was achieved by choosing an array of six capacitive elements whose total transmission phase shift is $90^{\circ}$ and whose total reflection, $\rho$, is proportional to an appropriate Tchebychef polynomial. This can be expressed mathematically.

$$\rho = \alpha T_5(x) = A_1 + A_2\, e^{-j2\phi} + A_3\, e^{-j4\phi} + A_4\, e^{-j6\phi} + A_5\, e^{-j8\phi} + A_6\, e^{-j10\phi} \quad (9)$$

$$\frac{\pi}{2} = \sum_{m=1}^{m=n} \theta_{\tau m} \quad (10)$$

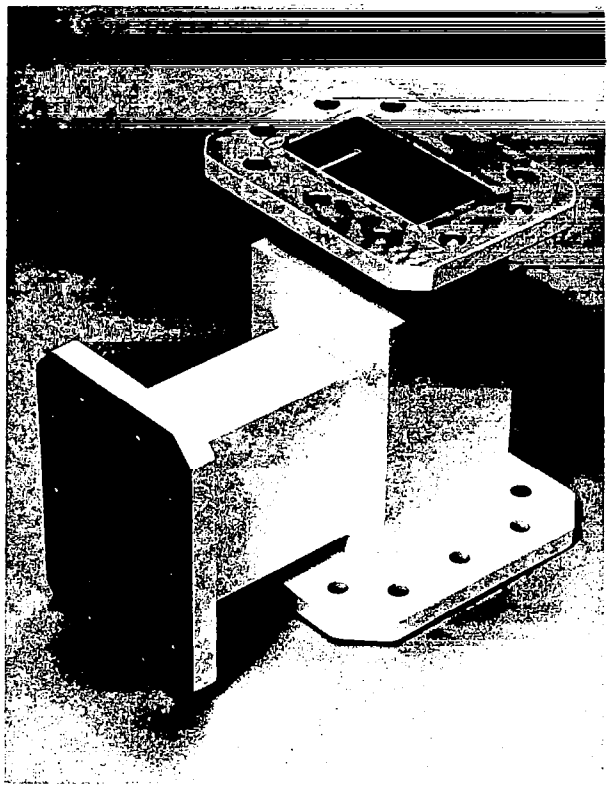

Figure 18. 4 GHz OMT

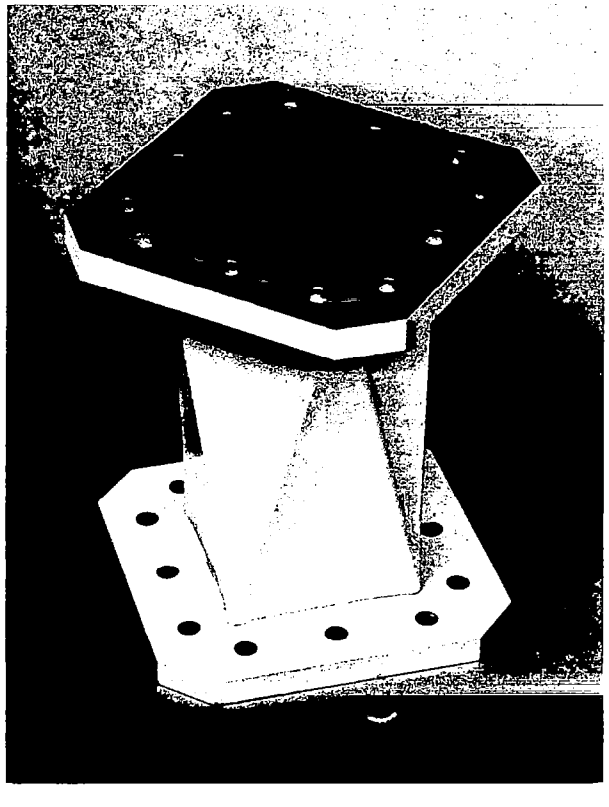

Figure 19. 4 GHz 45° Diagonal Twist

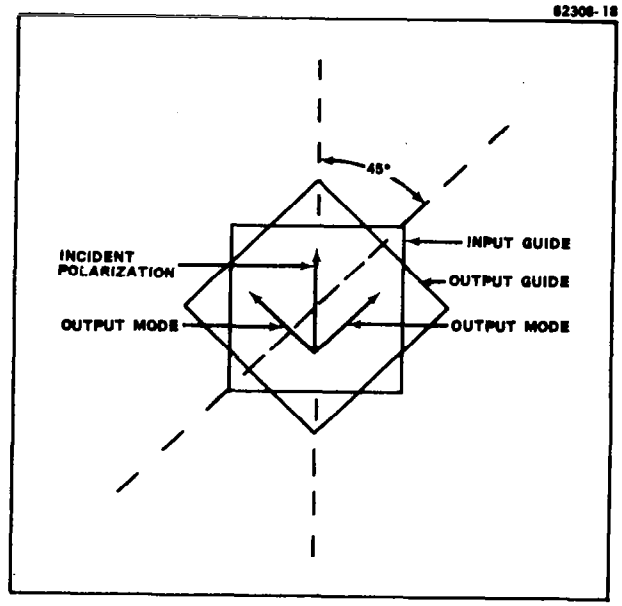


Figure 20. Input and Output Fields of $45^{\circ}$ Diagonal Twist

where

$T_5(x)$ = 5th order Tchebychef polynomial

$x = \frac{\cos \phi}{\cos \phi_1}$

$\phi$ = electrical length between elements

$\phi_1$ = electrically length between elements at low frequency

$\theta_\tau$ = individual element transmission phase shift

$A_n$ = individual element reflection coefficients

In addition, the expression relating the individual transmission phase shift to the individual reflection coefficient is needed which is given by

$$\left| A_n \right| = \sin \theta_{\tau n} \tag{11}$$

The phase shift of each element was calculated using equations (9), (10), and (11). Knowing the required phase shift of each element, the physical size of these elements was determined by measuring the phase shift of different size elements. This data appears in Figure 21. The spacing between elements, $\phi$, was made a quarter-wavelength and then adjusted to remove the additional phase shift introduced by the elements. The 4 GHz CIRCULAR POLARIZER was matched and a 90 degree differential phase shift obtained. Typical performance data appears in Table 5.

TABLE 5. 4 GHz CIRCULAR POLARIZER PERFORMANCE DATA

| Freq (MHz) | VSWR C | VSWR L | Difference Phase Shift | Axial Ratio (dB) |
|---|---|---|---|---|
| 3900 | 1.08 | 1.05 | 91 degrees | .6 |
| 4000 | 1.07 | 1.05 | 90 degrees | .5 |
| 4100 | 1.04 | 1.05 | 91 degrees | .6 |
| 4200 | 1.04 | 1.05 | 91 degrees | .8 |
| 4300 | 1.03 | 1.05 | 94 degrees | 1.1 |

* C is capacitively loaded mode and L is inductively loaded mode (Figure 21)

### 2.3.3 MAGIC TEE AND BENDS

The monopulse bridge circuitry requires four magic tees to accomplish the necessary combining operations. All four magic tees are the same and are of the conventional design shown in Figure 22. Typical performance data appears in Table 6.

TABLE 6. VSWR OF 4 GHz MAGIC TEE

| Frequency (MHz) | Sum | Difference |
|---|---|---|
| 3900 | 1.08 | 1.13 |
| 4000 | 1.04 | 1.07 |
| 4100 | 1.03 | 1.04 |
| 4200 | 1.04 | 1.06 |
| 4300 | 1.09 | 1.13 |

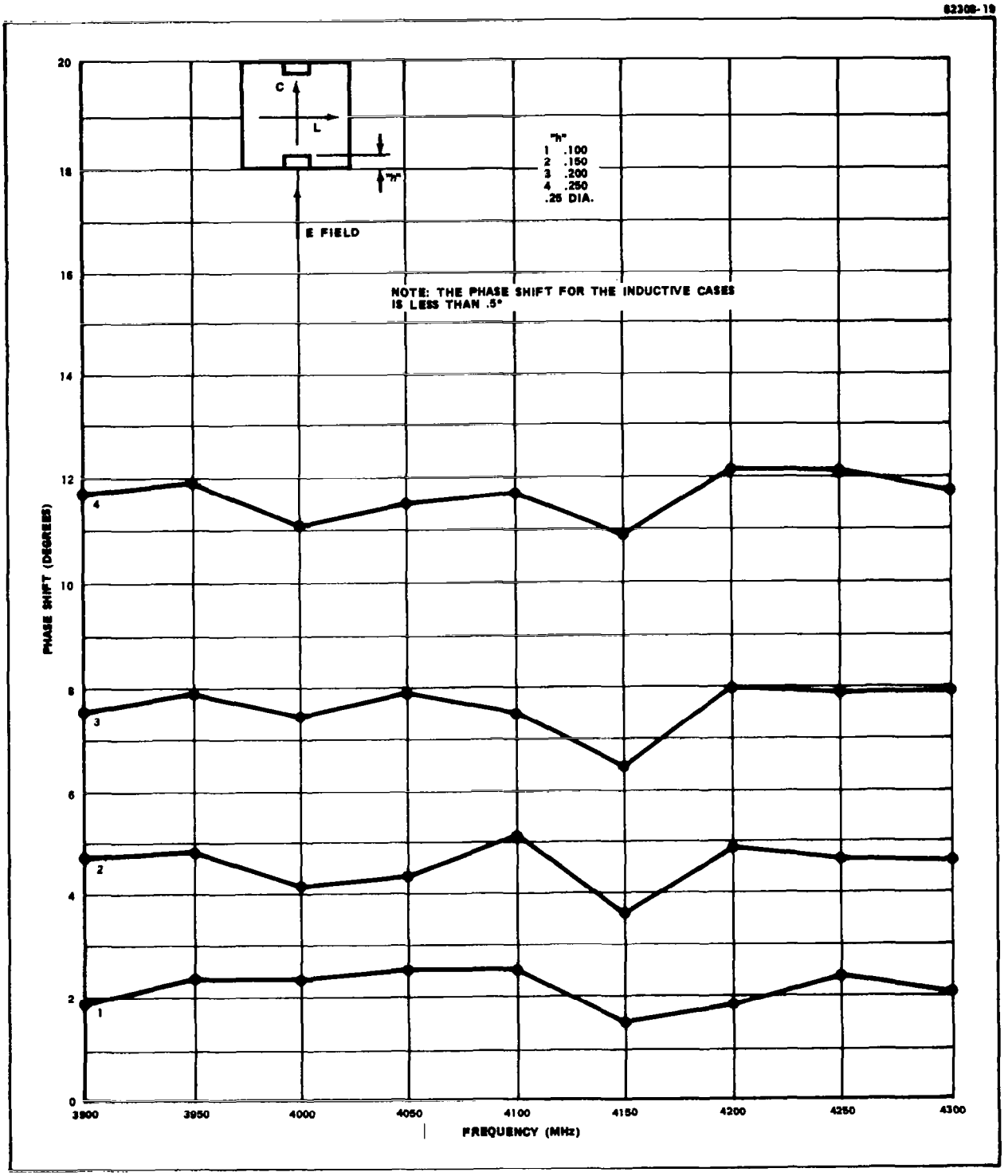


Figure 21. Measured Phase Shift of Capacitive Buttons

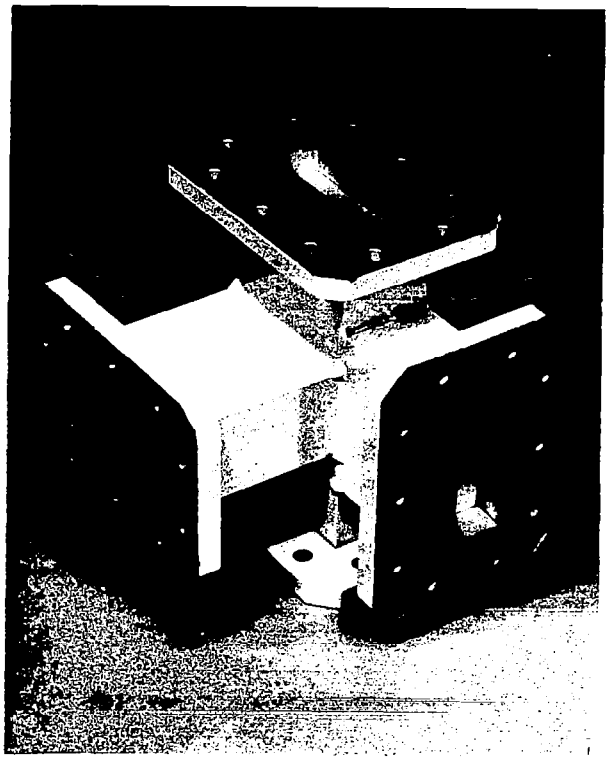

Figure 22. 4 GHz Magic Tee

Mitred E- and H-plane bends were used in preference to radius bends. This allowed a more compact feed package. Figure 23 shows a typical E-plane bend. A VSWR of less than or equal to 1.10 was obtained for all mitred bends used in the monopulse bridge circuitry.

### 2.3.4 POWER DIVIDER

Proper operation of the feed requires an E-field amplitude ratio between the center and outer horns ($E_{outer}/E_{center}$) of 0.289. This results in 75 percent of the power entering the center horn. This power division is accomplished with the power divider. The power divider consists of two magic tees (shown in Figure 24) connected with two 180 degree H-plane mitred bends of different phase length. Control of the differential phase shift produces the correct power split. Referring to Figure 25, the sum arm of the first magic tee is the input arm and splits the E-field according to

$$E_1 = \frac{E_{IN}}{\sqrt{2}}$$

$$E_2 = \frac{E_{IN}}{\sqrt{2}}$$

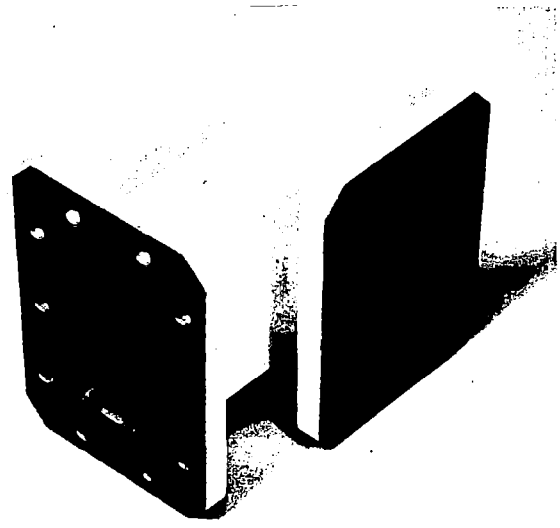

Figure 23. 4 GHz Mitered-E-Plane Bend

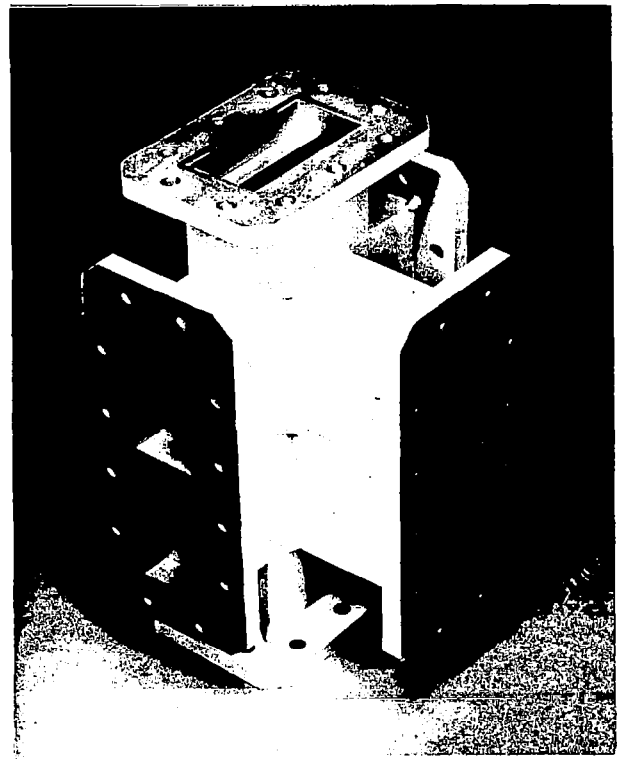

Figure 24. Magic Tee Assembly for Power Divider

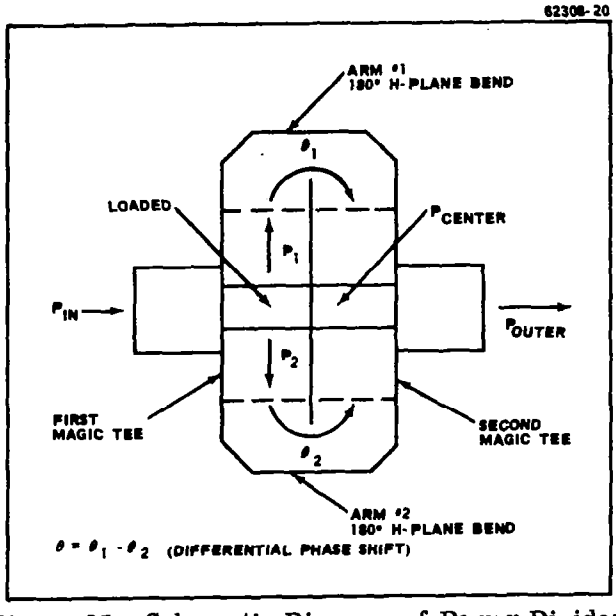


Figure 25. Schematic Diagram of Power Divider

The field in each arm is shifted in phase by the amounts $\theta_1$ and $\theta_2$ respectively before entering the second magic tee.

$$E_1 = \frac{E_{IN}}{\sqrt{2}} e^{j\theta} 1 = \frac{E_{IN}}{\sqrt{2}} \cos \theta_1 + j \frac{E_{IN}}{\sqrt{2}} \sin \theta_1$$

$$E_2 = \frac{E_{IN}}{\sqrt{2}} e^{j\theta} 2 = \frac{E_{IN}}{\sqrt{2}} \cos \theta_2 + j \frac{E_{IN}}{\sqrt{2}} \sin \theta_2$$

The field in the difference arm of the second magic tee which feeds the center horn is given by:

$$E_{center} = \frac{E_{IN}}{2} e^{j \theta_1} - \frac{E_{IN}}{2} e^{j \theta_2}$$

or the percent power feeding the center horn is;

$$\frac{P_{center}}{P_{IN}} = \sin^2 \frac{\theta}{2} \qquad (12)$$

where

$$\theta = \theta_1 - \theta_2$$

The field in the sum arm of the second magic tee which feeds the outer horn is given by:

$$E_{outer} = \frac{E_{IN}}{2} e^{j \theta_1} + \frac{E_{IN}}{2} e^{j \theta_2}$$

or the percent power feeding the outer horns is;

$$\frac{P_{outer}}{P_{IN}} = \cos^2 \frac{\theta}{2} \qquad (13)$$

If 75 percent of the power is to enter the center horn the differential phase shift, $\theta$, must be 120 degrees. Since the H-plane bends are in waveguide, phase dispersion will cause the power split to vary with frequency. Table 7 gives the theoretical and measured percent power feeding the center horn.

TABLE 7. POWER DIVIDER PERFORMANCE

| Freq. (MHz) | Measured Percent Power to Center | Theoretical Percent Power to Center |
|---|---|---|
| 3900 | 69.4% | 68.7% |
| 4100 | 74.5% | 75.0% |
| 4200 | 81.3% | 81.6% |

2.3.5 PHASING WAVEGUIDE

The five horn feed is operated with constant phase across the aperture. This requires that the outside four horns remain in phase with the center horn over the entire frequency band. This is not easily accomplished because the center and outer horns are not the same electrical length and do not have the same phase versus frequency response. Since a waveguide has phase dispersion and can be adjusted for any phase shift, it should be possible to control the phase variation between the horns over the frequency band. This waveguide section must meet the following requirements:

1. Phase all five horns for an in-phase condition

2. Minimize or eliminate any phase variation with frequency that would produce any untolerable degradation in the radiation patterns.

These two conditions can be expressed mathematically as:

In-Phase

$$\left[\phi_{\Sigma}^{PD} + \phi_{oc} + \phi_{o}\right]_{4100} = \left[\phi_{\Delta}^{PD} + \phi_{cc} + \phi_{c}\right]_{4100} \pm n2\pi \qquad (14)$$

Zero-Phase Variation

$$\left[\phi_{\Sigma}^{PD} + \phi_{oc} + \phi_{o}\right]_{4300} - \left[\phi_{\Sigma}^{PD} + \phi_{oc} + \phi_{o}\right]_{3900} =$$
$$\left[\phi_{\Delta}^{PD} + \phi_{cc} + \phi_{c}\right]_{4300} - \left[\phi_{\Delta}^{PD} + \phi_{cc} + \phi_{c}\right]_{3900} \qquad (15)$$

where

$\phi_{\Sigma}^{PD}$ = Phase shift of sum arm of power divider feeding outer horns

$\phi_{\Delta}^{PD}$ = Phase shift of difference arm of power divider feeding center horns

$\phi_{oc}$ = Phase shift of outer horn circuitry

$\phi_{cc}$ = Phase shift of center horn circuitry

$\phi_{o}$ = Phase shift of outer horn

$\phi_{c}$ = Phase shift of center horn

These equations were re-written in terms of equivalent waveguide lengths of the various components as:

In-Phase

$$\left[(\ell_{\Delta} - \ell_{\Sigma}) - \frac{\pi}{2} + \ell_{oc} + \frac{\lambda_g}{2\pi}(\phi_o - \phi_c)\right]_{4100} \pm n\lambda_{g4100} = \ell_{cc} \qquad (16)$$

Zero-Phase Variation

$$\ell_{\Delta} - \ell_{\Sigma} + \ell_{oc} + \frac{\Delta\phi_o - \Delta\phi_c}{2\pi} \frac{\lambda_{g4300}\lambda_{g3900}}{\lambda_{g3900} - \lambda_{g4300}} = \ell_{cc} \qquad (17)$$

where

$\ell_\Delta$ = Equivalent waveguide length of difference arm of power divider feeding center horn

$\ell_\Sigma$ = Equivalent waveguide length of sum arm of power divider feeding outer horns

$\ell_{oc}$ = Equivalent waveguide length of outer horn circuitry

$\ell_{cc}$ = Equivalent waveguide length of center horn circuitry

$\Delta\phi_o$ = Phase variation of outer horn over design bandwidth – 3900 to 4300 MHz

$\Delta\phi_c$ = Phase variation of center horn over design bandwidth – 3900 to 4300 MHz

The answer to the phasing problem is a simultaneous solution of equations (16) and (17) for "$l_{cc}$." The other values of phase shift and equivalent waveguide length appearing in equations (16) and (17) are needed before solution can be obtained. The phase shifts through the center and outer horns were calculated (for which a computer program had been written). The phase shift through the remaining components was measured by the double frequency method. Table 8 tabulates the calculated and measured phase shifts necessary to solve for the equivalent waveguide length of the center horn circuitry. Equation (16) was solved for various lengths depending on the value of "n" chosen. Equation (17) was solved for the exact length necessary to eliminate any phase variation. As anticipated, there was no simultaneous solution. Maintaining zero-phase variation over the frequency band with all five horns in phase is impossible without going to a waveguide of a different (non-standard) broadwall dimension.

TABLE 8. MEASURED PHASE LENGTH

A. Outer Circuitry

| Item | Phase length |
|---|---|
| Outer Circuitry | 27.04 inches |
| Sum Arm of Power Divider | 5.17 inches |
| Outer Horn | 817.15° at 3900 MHz<br>923.22° at 4300 MHz |

B. Center Circuitry

| | |
|---|---|
| Center Circuitry | 6.63 inches |
| Diff. Arm of Power Divider | 5.51 inches |
| Center Horn | 2266.55° at 3900 MHz<br>2537.67° at 4300 MHz |

Zero phase variation was compromised to accommodate the in-phase condition which resulted in a 29 degree theoretical phase variation between the center and outer horns from one end of the band (3900 MHz) to the other (4300 MHz).

A waveguide phasing section was fabricated in accordance with the theoretical design. Sum channel radiation patterns were taken at 4100 MHz and the phasing section adjusted to optimize the patterns. This required a shortening of the section by .364 inches. Sum patterns were then taken at 3900 and 4300 MHz and at each frequency the length of the phasing section was adjusted to optimize the patterns. The difference in lengths indicates the phase variation with frequency.

This was found to be approximately 24 degrees which agreed well with the theoretically predicted 29 degrees. This phase error (24 degrees) did not appreciably degrade the radiation patterns and the final length of the waveguide phasing section was chosen to optimize the radiation patterns at 4100 MHz.

## 2.4 PRIMARY FEED PERFORMANCE AT 4 GHz

Primary feed characteristics were evaluated on the 4 GHz five horn feed over the frequency band 3900 to 4300 MHz. This included measurements of circularly polarized radiation patterns, VSWR, isolation, etc. Patterns of the center horn at 6 GHz were also measured and are discussed in Section 2.5.

Sum channel radiation patterns were taken in each of the three planes: azimuth (AZ), elevation (EL), and diagonal – over the frequency band 3900 to 4300 MHz. These patterns appear in the Appendix. The average 10 dB beamwidth is 23.8 degrees. The sidelobe level (SLL) in the AZ and EL planes varies between 16 and 27 dB while the diagonal SLL varies between 11 and 15 dB. The SLL are higher at the band edges due to phase error between the center and outer horns at these frequencies. The SLL is lower at 4300 MHz than at 3900 MHz. This results because the power divider is frequency sensitive as discussed in Section 2.3.4 which gives the theoretical and measured percent power feeding the center horn. At 4300 MHz a greater portion of the power is going to the center horn than at 3900 MHz which produces a higher tapered aperture distribution and lower SLL in the far field.

Cross polarized radiation patterns were taken at 4100 MHz and are included in the Appendix. The cross polarization is down 24 dB in both the AZ and EL planes while in the diagonal planes it measures 20 dB in the sidelobe region. Within the 10 dB beamwidth the cross polarization is sufficiently small that no problem is anticipated.

Azimuth and elevation channel error patterns were taken over the frequency band 3900 to 4300 MHz. These patterns appear in the Appendix. The pertinent characteristics are tabulated in Table 9.

TABLE 9. PRIMARY ERROR CHANNEL CHARACTERISTICS (AVERAGE OF AZ AND EL)

| | |
|---|---|
| Peak-to-Peak Separation | 18.6 degrees |
| SLL from Peak of Sum | 11 - 13 dB |
| Unbalance in Main Lobes | 0.2 dB or less |
| Null Depth from Peak of Sum | 30 dB or greater |
| Peak of Sum-to-Peak of Error | 1 - 2 dB |

In order to calculate a representative spillover efficiency of the sum channel a more complete picture of the radiated power pattern is required. This was accomplished by measuring the power pattern at 4100 MHz at 22-1/2 degree increments from 0 degree to 180 degrees as shown in Figure 26. Due to symmetry, pattern integration was carried out only for the AZ, diagonal and 22-1/2 degree planes. The spillover efficiency was calculated for the two hyperboloids that will be tested with the 15-foot reflector (one with a splash ring and one without). The results are tabulated in Table 10.

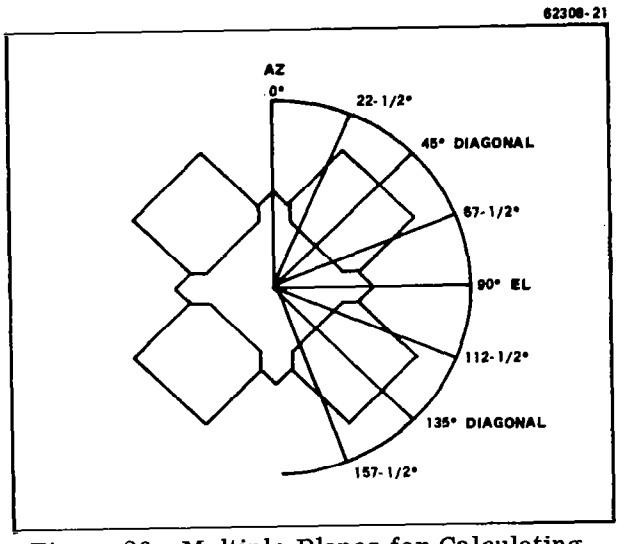


Figure 26. Multiple Planes for Calculating Spillover Efficiency

TABLE 10. SPILLOVER EFFICIENCY AT 4100 MHz

| Plane | Hyperboloid Without Splash Ring (11.9° Half Angle) Efficiency, % | Hyperboloid With Splash Ring (16.3° Half Angle) Efficiency, % |
|---|---|---|
| AZ and EL | 92.4 | 98.1 |
| Diagonal | 57.9 | 64.4 |
| 22-1/2°, 67-1/2°, 112-1/2°, and 157-1/2° | 78.4 | 86.9 |
| Average | 76.8% | 85.3% |

Axial ratio measurements were made at the peaks of sum and error channel radiation patterns over the frequency band 3900 – 4300 MHz. The feed axial ratio agreed quite closely with the axial ratio of a single polarizer. Specific data is given in Table 11.

TABLE 11. FEED AXIAL RATIO

| Frequency | Sum (dB) | AZ (dB) | EL (dB) |
|---|---|---|---|
| 3900 | .5 | .8 | .7 |
| 4000 | .7 | .8 | .3 |
| 4100 | .9 | .6 | .6 |
| 4200 | 1.1 | 1.4 | .9 |
| 4300 | 1.5 | 1.5 | 1.1 |

The VSWR was measured at the outputs of sum, azimuth, and elevation channels over the frequency band 3900 to 4300 MHz. The results appear in Table 12.

TABLE 12. FEED VSWR

| Frequency | Sum | AZ | EL |
|---|---|---|---|
| 3900 | 1.08 | 1.18 | 1.45 |
| 4000 | 1.17 | 1.16 | 1.04 |
| 4100 | 1.07 | 1.02 | 1.09 |
| 4200 | 1.04 | 1.17 | 1.28 |
| 4300 | 1.08 | 1.11 | 1.07 |

The intercoupling or isolation between ports was measured over the frequency band 3900 to 4300 MHz. Isolation between the sum channel and the remaining ports is of particular interest for noise temperature contributions and the lowest value measured was 32.5 dB with an average of 36 dB.

It was anticipated the isolation would decrease after the feed was installed in the cassegrain system. This is due to the incident power in the region of the vertex of the subreflector being reflected back into the feed. Anticipation of this led to a theoretical design of a vertex matching plate. Evaluation of the vertex matching plate and the noise temperature contribution due to the intercoupling was based on measured secondary performance. Specific data on isolation of the feed in free space is presented in the Appendix.

## 2.5 CAPABILITY AT 6 GHz

Simultaneous operation of transmit at 6 GHz and receive at 4 GHz utilizing the five horn feed requires the development of a dual frequency orthomode transducer. The

approach taken to design a dual frequency orthomode transducer required for extension to 6 GHz transmit capability is shown in Figure 27.

The 6 GHz input is in WR-112 waveguide which is transitioned to a 1.122 inch square waveguide. The 1.122 inch dimension cuts off the $TE_{11}$ and $TM_{11}$ modes over the entire design bandwidth – 5800 to 6200 MHz. The 4 GHz input is a single reduced height WR-187 waveguide which enters on a side wall. The dominant modes of 6 GHz and 4 GHz are space orthogonal in the output waveguide. The output of the dual frequency orthomode transducer is 1.870 inches square. This dimension cuts off the $TE_{12}$ and $TM_{12}$ modes at 6 GHz and all higher order modes at 4 GHz. The $TE_{11}$ and $TM_{11}$ modes can propagate in this section at 6 GHz but proper design – symmetrical structures – should prevent these modes from being excited. The single 4 GHz input represents an asymmetrical structure to the 6 GHz. It was anticipated the reduced height WR-187 waveguide would minimize this discontinuity to a point where the higher order modes are not excited and a second input for balance feeding is not required. If this fails, a second input is required. The matching section has a twofold purpose. First, it must match the 6 GHz OMT section to the 4 GHz OMT section. Second, it must represent an effective short at the right location to match the 4 GHz arm over the frequency band. At one time during the development, the 6 GHz OMT section consisted of a WR-137 waveguide input transistioned to a 1.372 inch square waveguide. For this case, it was impossible to match the 4 GHz arm over the required bandwidth. This was probably due to a drastic change in the position of the effective short produced by the matching and 6 GHz OMT section. Even with the addition of a transverse post, the bandwidth was not obtained. The 6/4 OMT shown in Figure 27 was matched reasonably well and specific data appears in Table 13. This 6/4 OMT was used to evaluate the radiation patterns of the five horn feed at 6 GHz.

TABLE 13. VSWR DATA ON 6/4 OMT

| 4 GHz Arm | | 6 GHz Arm | |
|---|---|---|---|
| Freq. | VSWR | Freq. | VSWR |
| 3900 | 1.19 | 5800 | 1.07 |
| 4000 | 1.17 | 5900 | 1.13 |
| 4100 | 1.19 | 6000 | 1.15 |
| 4200 | 1.05 | 6100 | 1.22 |
| 4300 | 1.23 | 6200 | 1.24 |

Radiation patterns of the center horn were taken over the frequency band 5800 to 6200 MHz. These patterns appear in the Appendix. The patterns show some asymmetry, probably due to the odd modes ($TE_{11}$ and $TM_{11}$) excited in the 6/4 orthomode transducer (OMT) used. The 6/4 OMT has only a single input for the 4 GHz which results in an asymmetrical structure and could excite the higher order odd modes ($TE_{11}$ and $TM_{11}$). The patterns also reveal that a quadratic phase error is present. This phase error results because the flare angle of the center horn is too large for operation at 6 GHz. Even with these deficiencies, the calculated average spillover efficiencies are 72.3 percent for the hyperboloid without splash ring and 86.8 percent with splash ring at 6 GHz.

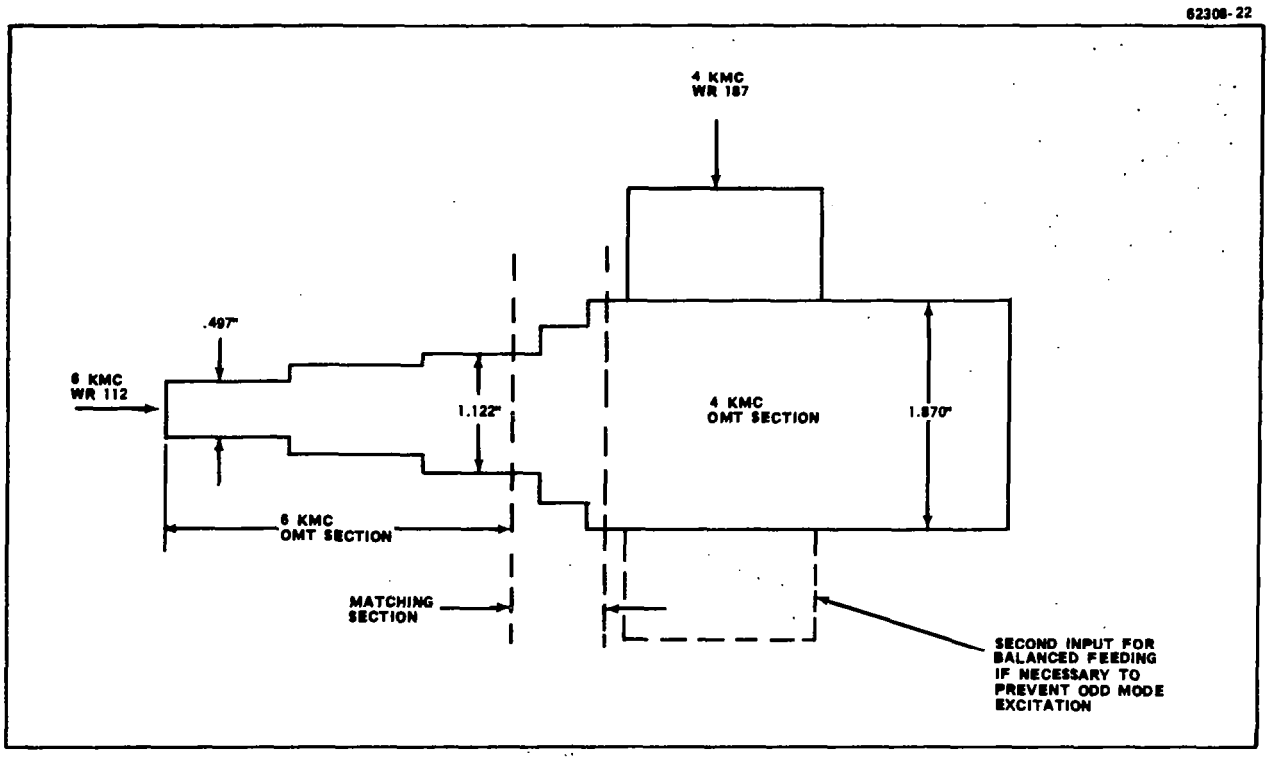


Figure 27. Transmit Capability

Section Three

# 3.0 CASSEGRAIN ANTENNA SYSTEM

## 3.1 CASSEGRAIN DESIGN

The cassegrain design establishes the location and contour of the hyperboloid and the proper position of the feed. Using the parameters:

$D = 180$ inches

$F/D = .40$

$\alpha = 11.9$ degrees

$f = 63$ inches

the cassegrain geometry (see Figure 2) was determined. The constant "$\alpha$" was chosen by radiation pattern measurements on the feed. The angle, $\alpha = 11.9^{o}$, corresponds to approximately a 10 dB taper at the hyperboloid edge which results in optimum gain and still provides enough taper to obtain reasonably low sidelobes. The position of the feed was set by the minimum blockage condition of the feed and hyperboloid combination. From phase center measurements, the best phase center of the feed was found to be within plus or minus one inch of the common aperture of the five horns. This allowed the throats of the outside four horns to be located near the vertex which eased the mounting of the feed to the reflector hub. The required hyperboloid focal length for this configuration was 63 inches. The remaining cassegrain geometry is determined as follows:

(1) $$d = \frac{2f}{\cot \alpha + \cot\theta_o}$$

$$= \frac{(2)\ (63)}{4.745 + .488} = 24 \text{ inches}$$

(2) $$M = \frac{D}{4F} \cot\frac{\alpha}{2}$$

$$\frac{1}{(4)(0.4)} (9.595) = 6.00$$

(3) $$e = \frac{M + 1}{M - 1}$$

$$= \frac{6 + 1}{6 - 1} = 1.400$$

(4) $$a = f/2e$$

$$= \frac{63}{(2)\ (1.40)} = 22.500 \text{ inches}$$

(5) $$b = a\ e^2 - 1$$

$$= (22.500)\ (1.4^2 - 1)^{1/2} = 22.045 \text{ inches}$$

(6) $$P = f/2 - a$$

$$= 31.5 - 22.5 = 9 \text{ inches}$$

This results in a design as shown in Figure 29.

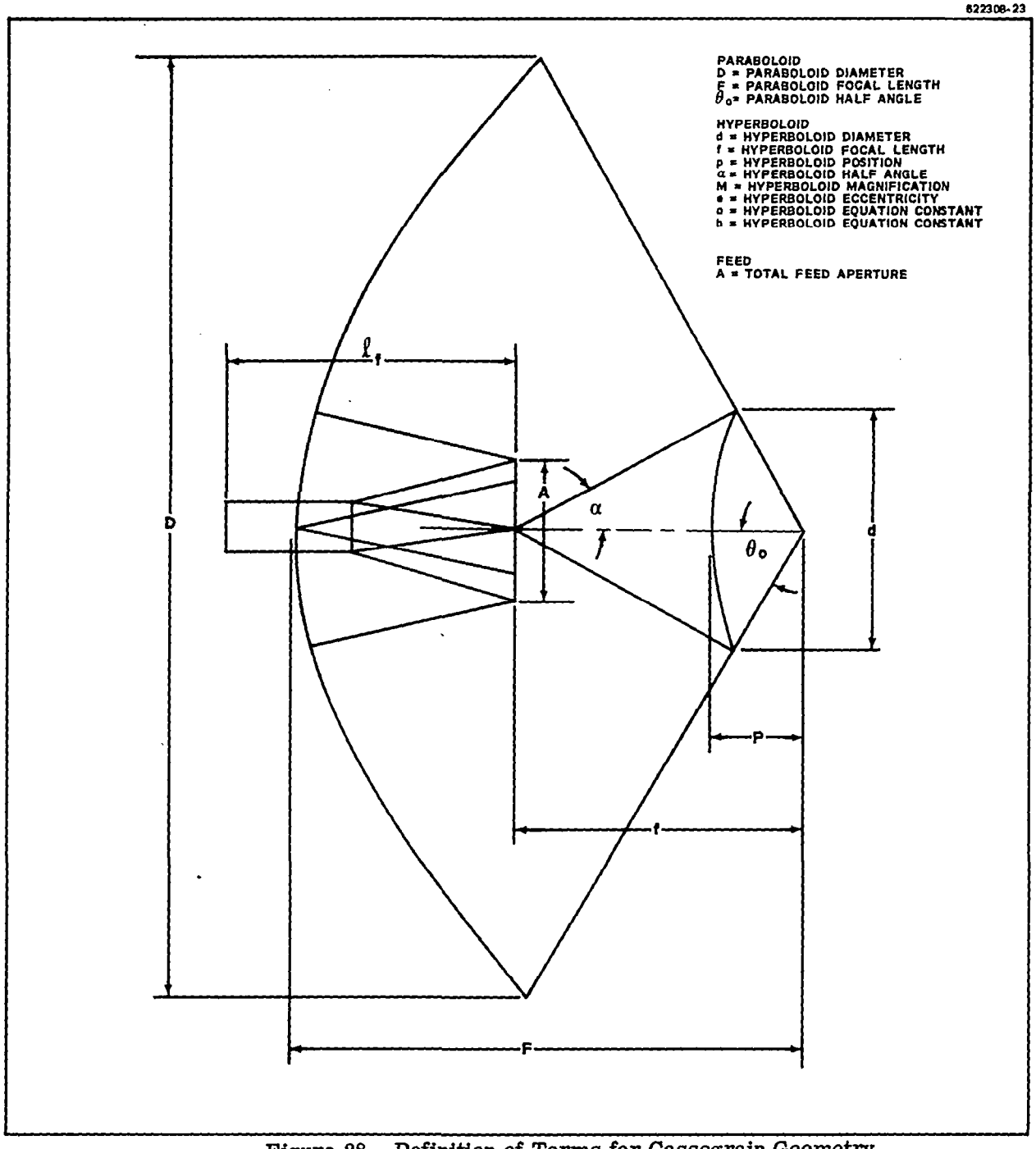


Figure 28. Definition of Terms for Cassegrain Geometry

The hyperboloid is a part of the feed system. All adjustments of the feed were incorporated into the hyperboloid. Provisions were made for focusing, off-axis alignment to the feed electrical axis and hyperboloid tilt to adjust the antenna boresight if required. After the adjustments had been made the hyperboloid structure was pinned to prevent any further accidential movement.

The secondary dish (hyperboloid) is supported by a quadripod. The quadripod was chosen over other arrangements because it has symmetry in all planes which the tripod does not have and has less blockage than an octapod. Each leg of the quadripod consists of two struts (main strut and secondary strut). The main strut was designed to reduce the beam pointing error to less than .01 degrees from an off axis translation when the antenna was moved from a horizontal to a zenith position. The secondary strut was added to prevent tilting of the hyperboloid by an off axis wind loading.

Two hyperboloids were used in the evaluation of secondary antenna characteristics. The difference between the two hyperboloids was a splash plate. The splash plate consists of a ring 1.8 wavelengths wide tilted at an angle of 18.4 degrees added onto the outer edge of the basic hyperboloid.

One problem was encountered during the design of the support structure. The initial subreflector support structure was designed to fit a dish of F/D = 0.42 as specified in the Statement of Work. This support structure did not fit the dish supplied. Measurements on the dish indicated an F/D = 0.4. The re-design of the subreflector support structure was based on an F/D = 0.4. Also the subreflector without the splash plate was designed and built to fit a 0.42 F/D. However, it was possible to utilize this subreflector with the 0.4 dish although the hyperboloid focal point lies about three inches behind the phase center with the present design. This should not appreciably affect performance, however, based on experience in moving the feed during secondary tests during the previous Lo-Noise feed study NAS5-3282. The hyperboloid with a beamshaping flange was fabricated with the correct contour for an F/D of 0.4. Fortunately, this part had not been released for fabrication when the dish error was discovered.

## 3.2 SECONDARY ANTENNA PERFORMANCE

Secondary antenna characteristics were evaluated on the 15-foot Cassegrain antenna system shown in Figure 30 over the frequency band 3900 to 4300 MHz. This included measurements of both circular and linear polarized radiation patterns, VSWR, isolation, and gain. Radiation patterns were taken using the 3800 foot antenna test range located at Carbon Canyon. The transmit and receive sites are at the same elevation and lie on opposite sides of the canyon. With the floor of the canyon approximately 400 feet below the sites, the depression angles are 14 degrees for the transmit site and 21 degrees for the receive site.

Isolation and VSWR measurements were completed only for the hyperboloid without the splash ring. The VSWR of the feed installed in the 15-foot reflector was found to be approximately the same as in free space. On the other hand, isolation between the sum channel and the orthogonal arms of the orthomode transducer (OMT) decreased (from 32 dB to 23 dB) when the feed was installed. This is due to the incident power in the region of the hyperboloid vertex reflecting back into the feed. As this reflected power is oppositely polarized, it appears at the orthogonal arms of the OMT. If it is assumed that all isolated ports are terminated with a 300°K load, the noise temperature contribution would be approximately 5°K. In order to decrease this coupling to the orthogonal ports and the resulting noise contribution, additional vertex matching of the hyperboloid is required.

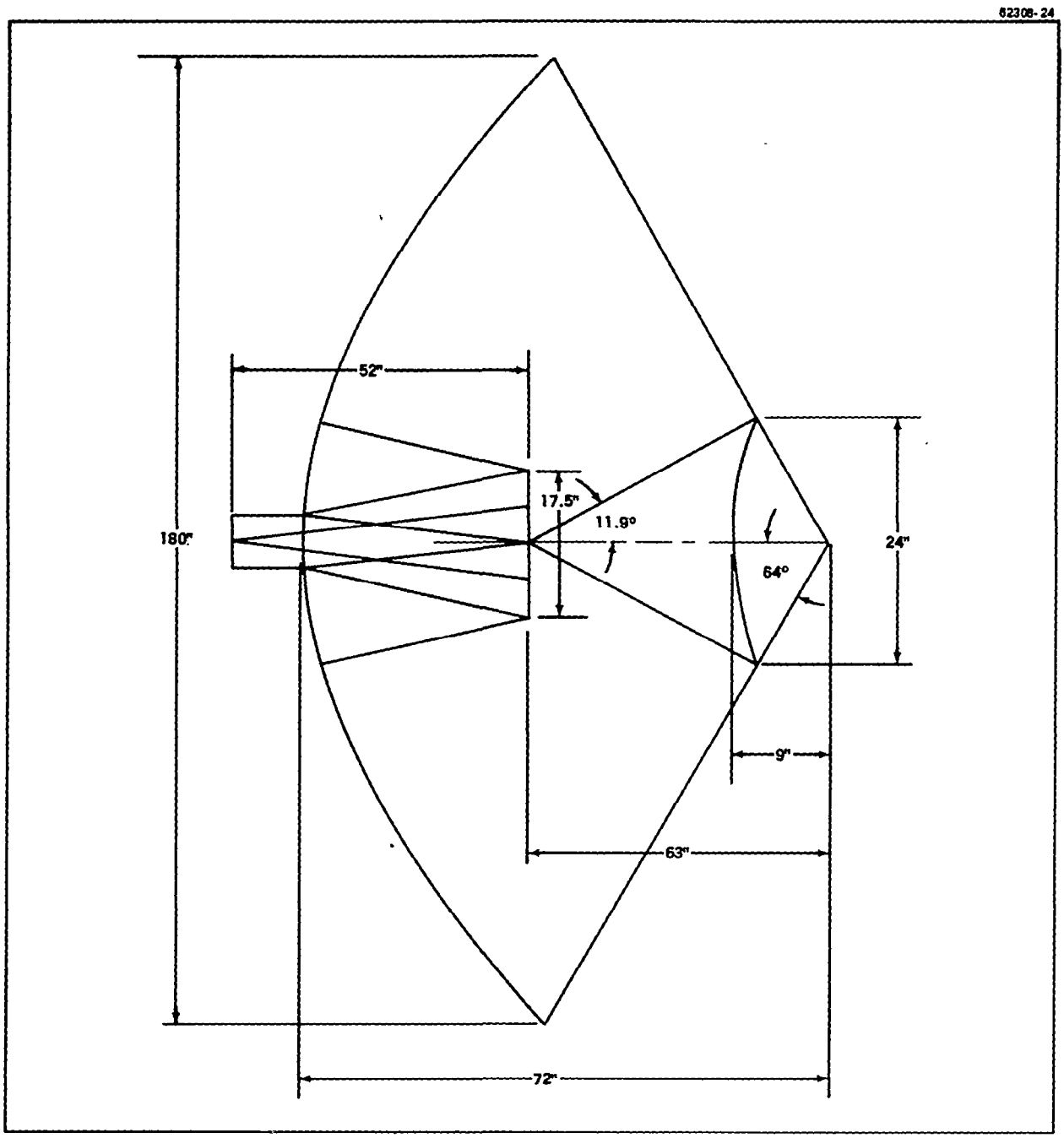


Figure 29. Cassegrain Geometry for 15-Foot Five Horn Feed Antenna System

All other intercouplings remained the same after the feed was installed in the Cassegrain system.

Sum channel radiation patterns were taken in the azimuth (AZ), elevation (EL), and the two diagonal planes for right circular (RCP) and linear polarizations over the frequency band from 3900 to 4300 MHz. Radiation patterns were measured using both hyperboloids. Sidelobe levels for the case without a splash plate varied between 17.0 and 20.5 dB while with the splash plate they were somewhat higher (14.9 to 17.8 dB). Sidelobe level data is given in Table 14.

TABLE 14. SLL FOR RCP PATTERNS OF 15-FOOT CASSEGRAIN ANTENNA SYSTEM

| | Without Splash Ring | | | | With Splash Ring | | | |
|---|---|---|---|---|---|---|---|---|
| Freq. (MHz) | AZ | EL | Diag $45^o$ | Diag $-45^o$ | AZ | EL | Diag $45^o$ | Diag $-45^o$ |
| 3900 | 18.5 | 17.8 | 17.0 | 17.8 | 17.6 | 16.7 | 16.6 | 17.1 |
| 4000 | 19.5 | 18.3 | 18.7 | 18.6 | 17.8 | 16.8 | 16.0 | 16.1 |
| 4100 | 19.5 | 18.2 | 19.5 | 18.3 | 17.5 | 15.9 | 15.5 | 15.8 |
| 4200 | 20.5 | 18.9 | 20.1 | 17.7 | 17.5 | 16.0 | 15.4 | 15.7 |
| 4300 | 20.5 | 18.8 | 18.7 | 19.0 | 17.6 | 15.9 | 14.9 | 15.5 |

The 3 dB beamwidth of the 15-foot Cassegrain antenna system is approximately one degree. The beamwidth using the hyperboloid without the splash plate is slightly larger than with the splash plate. A possible reason for this is that the hyperboloid without the splash ring was designed for a dish with an F/D of 0.42 which would result in illuminating a smaller area of the paraboloid which has an F/D of 0.40. Specific data on beamwidths appears in Table 15.

TABLE 15. 3 DB BW FOR RCP PATTERNS OF 15-FOOT CASSEGRAIN ANTENNA SYSTEM

| | Without Splash Ring | | | | With Splash Ring | | | |
|---|---|---|---|---|---|---|---|---|
| Freq. (MHz) | AZ | EL | Diag $45^o$ | Diag $-45^o$ | AZ | EL | Diag $45^o$ | Diag $-45^o$ |
| 3900 | $1.11^o$ | $1.14^o$ | $1.13^o$ | $1.13^o$ | $1.08^o$ | $1.04^o$ | $1.11^o$ | $1.07^o$ |
| 4000 | $1.11^o$ | $1.12^o$ | $1.11^o$ | $1.11^o$ | $1.02^o$ | $1.01^o$ | $1.07^o$ | $1.03^o$ |
| 4100 | $1.10^o$ | $1.12^o$ | $1.09^o$ | $1.10^o$ | $1.00^o$ | $1.00^o$ | $1.01^o$ | $.99^o$ |
| 4200 | $1.05^o$ | $1.11^o$ | $1.10^o$ | $1.10^o$ | $.96^o$ | $.95^o$ | $1.00^o$ | $.95^o$ |
| 4300 | $1.07^o$ | $1.05^o$ | $1.04^o$ | $1.04^o$ | $.95^o$ | $.96^o$ | $.96^o$ | $.93^o$ |

The only anomaly encountered with the sum channel radiation patterns was an apparent quadratic phase error that was dependent on the plane of the pattern cut (astigmatism). The astigmatism is apparently caused by asymmetry of the 15-foot dish as will be discussed later in more detail. A representative set of patterns appear in the Appendix.

Secondary radiation patterns were also calculated using the primary pattern data. An average illumination was used, and patterns computed for the 15-foot dish with and without considering subreflector blockage. The presence of the splash ring was not taken into account except from a blockage standpoint. The patterns are shown in Figures 31 and 32. As may be seen by comparison with the measured data given in the Appendix, the sidelobe level and position of the predicted sidelobe agrees reasonably well with that actually obtained.

**Figure 30. 15-Foot Cassegrain Antenna System**

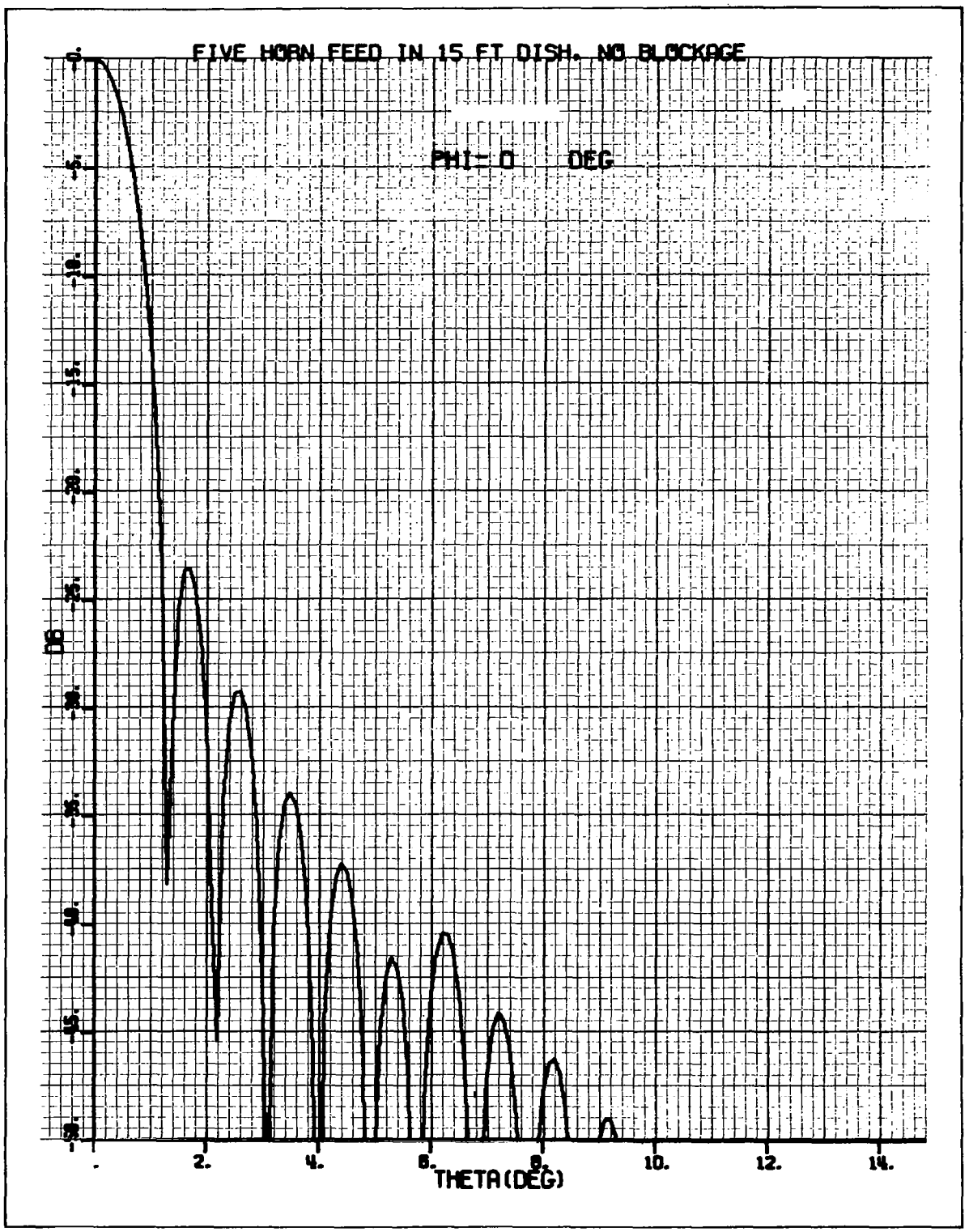


Figure 31. Calculated Radiation Pattern of Five Horn Feed in 15 Foot Dish – No Blockage

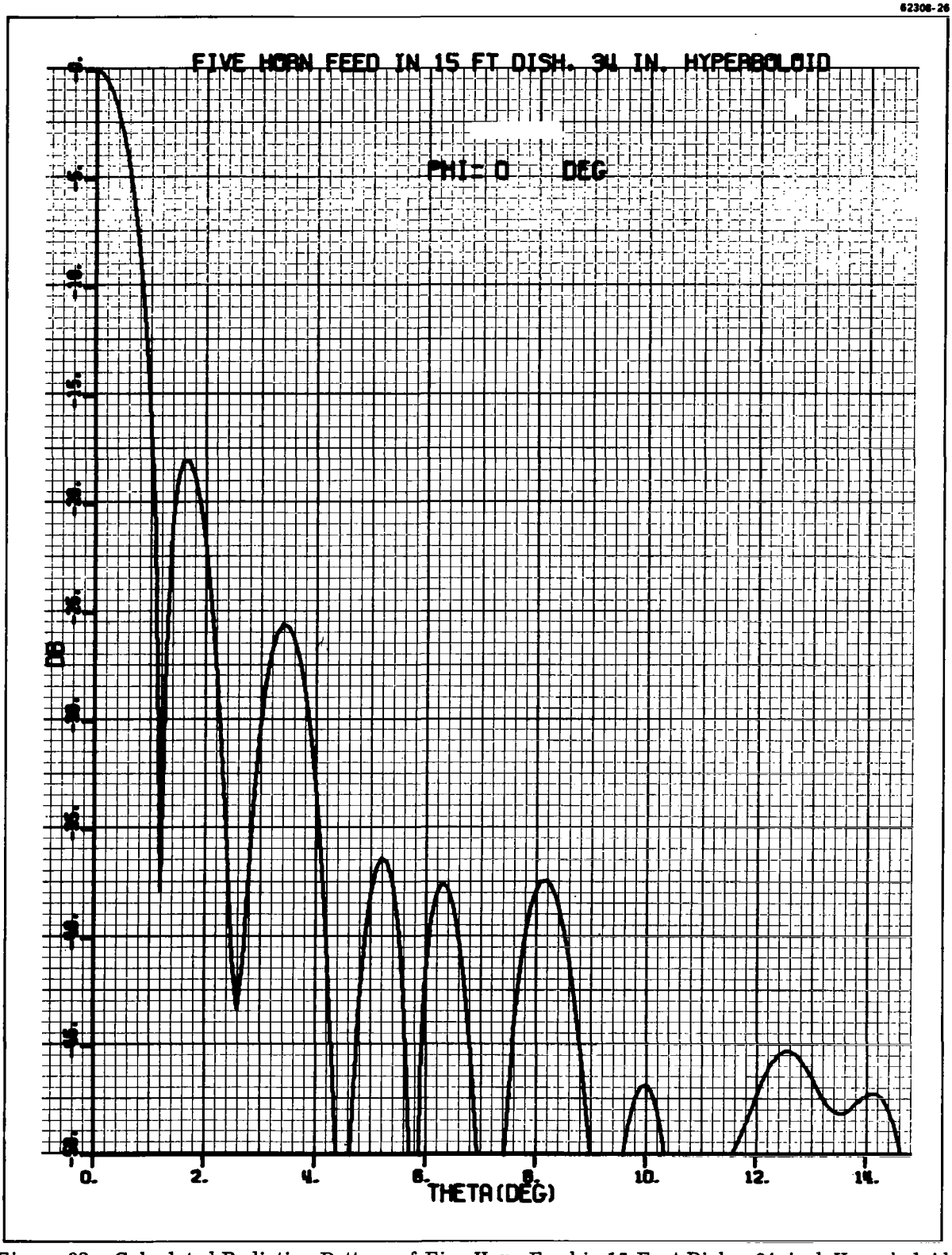


Figure 32, Calculated Radiation Pattern of Five Horn Feed in 15 Foot Dish – 34-inch Hyperboloid and Splash Ring

Azimuth and elevation error channel patterns were taken for both hyperboloids over the frequency band 3900 to 4300 MHz and appear in the Appendix. Measured results of the pertinent characteristics are tabulated in Table 16.

TABLE 16. RCP ERROR CHANNEL CHARACTERISTICS OF 15-FOOT CASSEGRAIN ANTENNA SYSTEM

| | Without Splash Ring | With Splash Ring |
|---|---|---|
| Sidelobe Level from Peak of Sum | (av) 16.6 dB | (av) 15.7 dB |
| Null Depth from Peak of Sum | 36 dB | 36 dB |
| Orthogonality of Null Planes | $90.0^{o} \pm .5^{o}$ | --- |
| Roll Error Vs Incident Linear | $.03^{o}$ | $0.0^{o}$ |
| Boresight Error Vs Frequency | (pessimistic) $.07^{o}$ | $.01^{o}$ |
| Peak of Sum-to-Peak of Error | (av) 5.6 dB | (av) 6.0 dB |
| Error Slope Reference to Peak of Error | --- | 161 mv/mr |

Axial ratio measurements were made at the peaks of the sum and error channel radiation patterns over the frequency band 3900 to 4300 MHz for both hyperboloids. The axial ratio of the Cassegrain antenna system agreed closely with the axial ratio of the feed in free space. Specific data is given in Table 17.

TABLE 17. AXIAL RATIO OF 15-FOOT CASSEGRAIN ANTENNA SYSTEM

| | Without Splash Ring | | | With Splash Ring | | |
|---|---|---|---|---|---|---|
| Freq. (MHz) | Sum | AZ | EL | Sum | AZ | EL |
| 3900 | .5 | .7 | .2 | .3 | 1.1 | .4 |
| 4000 | .5 | .6 | .5 | .7 | 1.2 | .6 |
| 4100 | .6 | .7 | 1.2 | .9 | 1.0 | 1.2 |
| 4200 | .9 | 1.7 | 1.2 | 1.2 | 1.7 | 1.6 |
| 4300 | 1.4 | 1.8 | 1.7 | 1.5 | 1.9 | 1.4 |

Before any antenna measurements were made, the Cassegrain antenna system was focused. Focusing was accomplished by obtaining minimum sidelobes and nulls on both sides of the main beam. In the case of the hyperboloid without a splash ring, the hyperboloid was initially placed at the theoretical focus. This proved to be the correct location to focus the azimuth plane patterns. At this same location the elevation plane patterns revealed the presence of a quadratic phase error. By measuring the sum pattern in multiple planes it was discovered that there is a gradual increase in the phase error going from the azimuth plane (a minimum phase error) to the elevation plane (a maximum phase error). The hyperboloid (no splash ring) was left at the theoretical focal point and secondary characteristics measured. Due to the addition of the splash ring, it was anticipated that the antenna would not be focused by placing the hyperboloid (with splash ring) at the theoretical focal point. In addition to obtaining minimum sidelobe levels and nulls on both sides of the main beam, maximizing the gain was added to the requirements of focusing the antenna. Patterns and data on gain versus axial displacement of the hyperboloid were taken and the results plotted in Figure 33. Referring to Figure 33 there are three (3) points of interest. The first one is the point of theoretical focus where neither the azimuth nor the elevation planes are focused and the gain is not maximized. The second point is where the gain is an absolute maximum and the azimuth plane is focused. This point which is closer to the feed makes optimum use of the energy intercepted by the splash ring and results in a quadratic phase error in the elevation plane (same problem encountered here as with the hyperboloid with no splash ring). The third point – approximately one half wavelength closer to the feed – is where the gain maximized

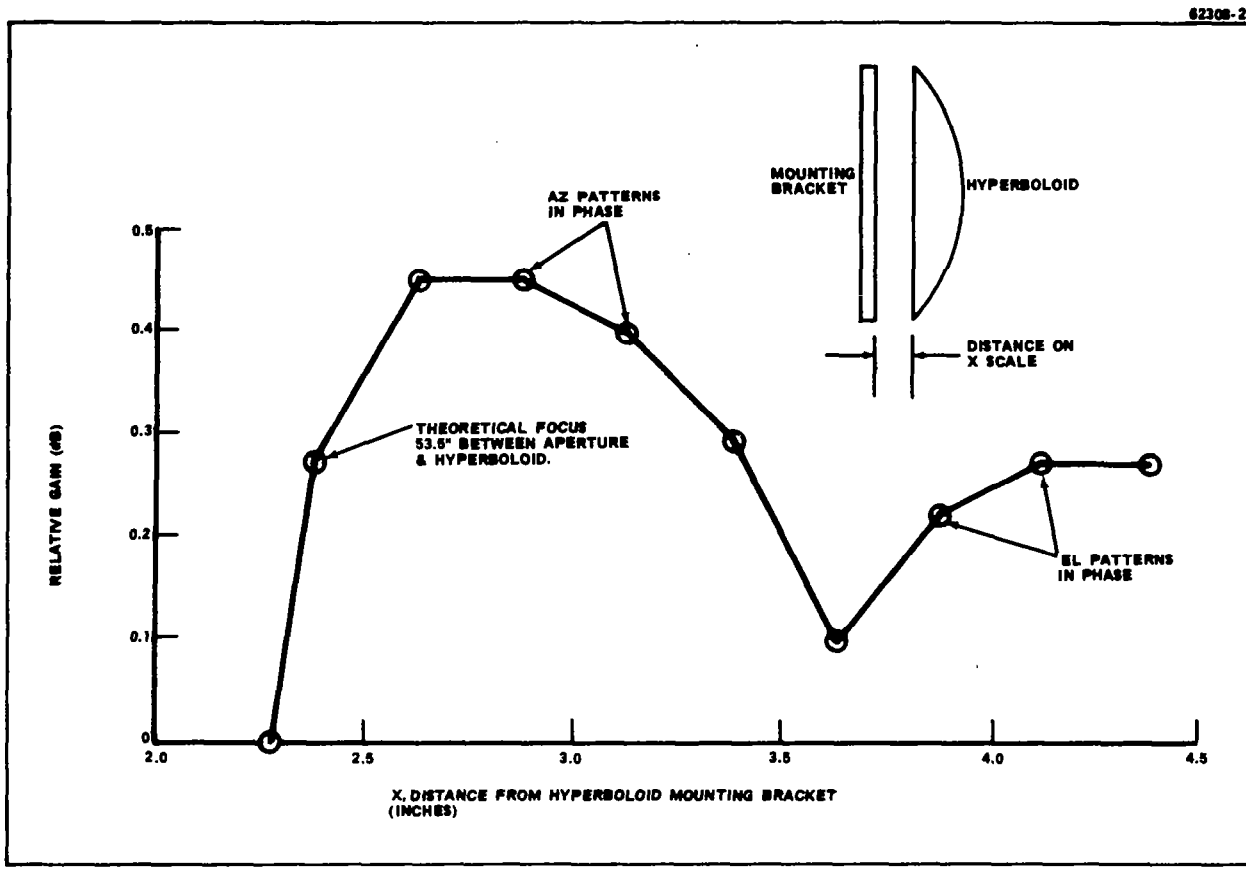


Figure 33. Gain vs. Hyperboloid Location

again (slightly lower than the first maximum) and the elevation plane is focused. This phenomenom of double focus is not completely explainable at this time but does not appear to depend on the hyperboloid. Therefore, it appears that the main dish may have some asymmetry. The hyperboloid (with splash ring) was placed at the point of absolute maximum gain and secondary characteristics measured.

Gain measurements were made on the antenna at 4100 MHz for both hyperboloids. The maximum gain of the antenna using the hyperboloid without splash ring measured 41.91 dB. This corresponds to an efficiency of 40.2%. This gain was measured by the total power method which is outlined in Figure 34.

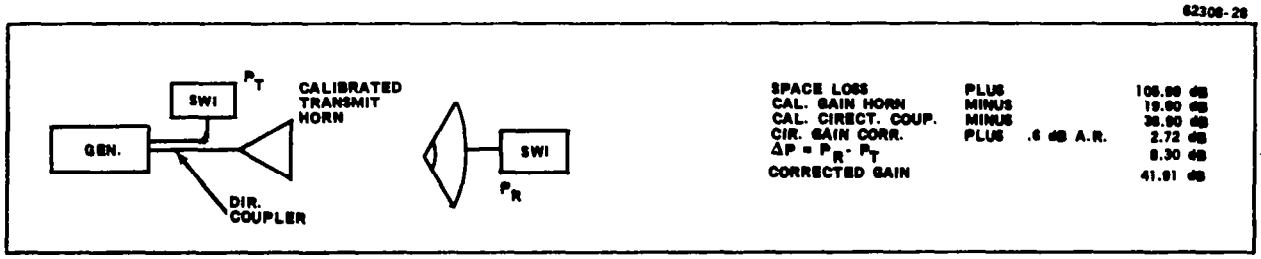


Figure 34. Total Power Method of Gain Measurement

This gain is low for three reasons:

1. The entire 15-foot dish is not illuminated because the hyperboloid was designed to work with a F/D of 0.42 dish. The effective dish diameter is thus about 14.3 feet.

2. The additional phase error introduced by not having the feed phase center at the hyperboloid focal point which is also due to the hyperboloid being designed for a 0.42 F/D dish.

3. During the gain measurements, there was trouble with the transmit prime power generating equipment. This problem was cleared up when making measurements with the hyperboloid with splash dish.

The maximum gain measured using the hyperboloid with the splash ring was 43.36 dB which corresponds to an efficiency of 56.2 percent. Two methods of gain measurement were used: (1) total power, and (2) gain comparison. These two methods agreed within 0.1 dB. This measured gain agrees well with the theoretical gain as shown below:

EXPECTED GAIN – FIVE HORN FEED CASSEGRAIN ANTENNA
15-FOOT DISH, FREQUENCY = 4100 MHz

| | | | |
|---|---|---|---|
| 1. | Spillover efficiency (from April report) | 85% | -0.7 dB |
| 2. | Illumination Efficiency (Silver) | 82% | -0.86 dB |
| 3. | Hyperboloid Blockage Loss $\eta_B = \left[1 - 2\left(\frac{d}{D}\right)^2\right]^2$ (d = 34 in subreflector) | = 86.3% | -0.64 dB |
| 4. | Strut blockage Loss $\eta_S = \left(1 - 1.55\frac{W}{D}\right)^2$ (Four struts of width W = 1.5 inches) | = 91% | -0.41 dB |
| 5. | Total Gain Loss | | -2.61 dB |
| 6. | Maximum Gain (15-foot Dish, Efficiency, 100%) | | 45.87 dB |
| 7. | Expected Measured Gain | | 43.26 dB |
| 8. | Actual Measured Gain | | 43.36 dB |

# 4.0 LOW NOISE PARAMETRIC AMPLIFIER

## 4.1 PARAMETRIC AMPLIFIER DESCRIPTION

The parametric amplifier (paramp) is a non-degenerate type and is pumped at a frequency of approximately 30.5 GHz. As shown in the photo, Figure 35, the lid is removed from the enclosure to show the parametric amplifier assembly. A block diagram of the parametric amplifier is given in Figure 36. The pump tube is a Sperry tunable reflex-klystron type SRV-4403 (see Appendix) and is conduction cooled by hard mounting it to the enclosure. The pump circuit consists of a $K_a$-band directional coupler-detector for pump power monitoring, a $K_a$-band attenuator for adjusting the pump power output to the paramp cavity to vary the paramp gain, and a $K_a$-band isolator. The pump circuit is attached to the paramp cavity consisting of a signal tuner, a varactor diode mount, and a coaxial signal input port. The paramp signal input port is coupled to the four-port circulator (circulator-isolator combination) with a low VSWR GR-900 coaxial connector. The varactor diode is biased from the terminal provided at the circulator. The signal input and output ports of WR-229 waveguide (CPR-229F flange) to GR-900 coaxial transitions are coupled to the four-port circulator at both ends.

## 4.2 OPERATION OF THE PARAMETRIC AMPLIFIER

To simplify instrumentation and operation of the parametric amplifier, the paramp is self-biased with a 1.1 megohm resistor and therefore an external varactor diode bias supply is not required.

With the klystron power supply in power-off condition, connect one end of the 25 ft cable to the klystron power supply output terminal and the other end of the cable to the parametric amplifier enclosure (Klystron power supply terminal). This is all that is required to operate the paramp.

The pump power output, may be monitored by connecting the pump output monitor terminal located at the enclosure to the cable and adapt a microammeter (not furnished) on the other end of the cable. The varactor diode may be externally biased by removing the 1.1 megohm resistor and connecting the interconnecting cable to the provided terminal at the enclosure and connect the bias power supply at the other end of the cable.

Over the 4000 to 4200 MHz frequency range, the paramp can be tuned with the paramp totally enclosed in its enclosure. The tuning and gain adjustment is accomplished by removing the GAIN and SIGNAL TUNER cover plates and by inserting a screwdriver through its opening and turning the screwdriver slot control knobs. Rotating the signal tuner knob will vary the frequency response of the paramp and rotating the gain adjusting knob will vary the gain of the paramp frequency response. If extended frequency tuning range (greater than 4000 to 4200

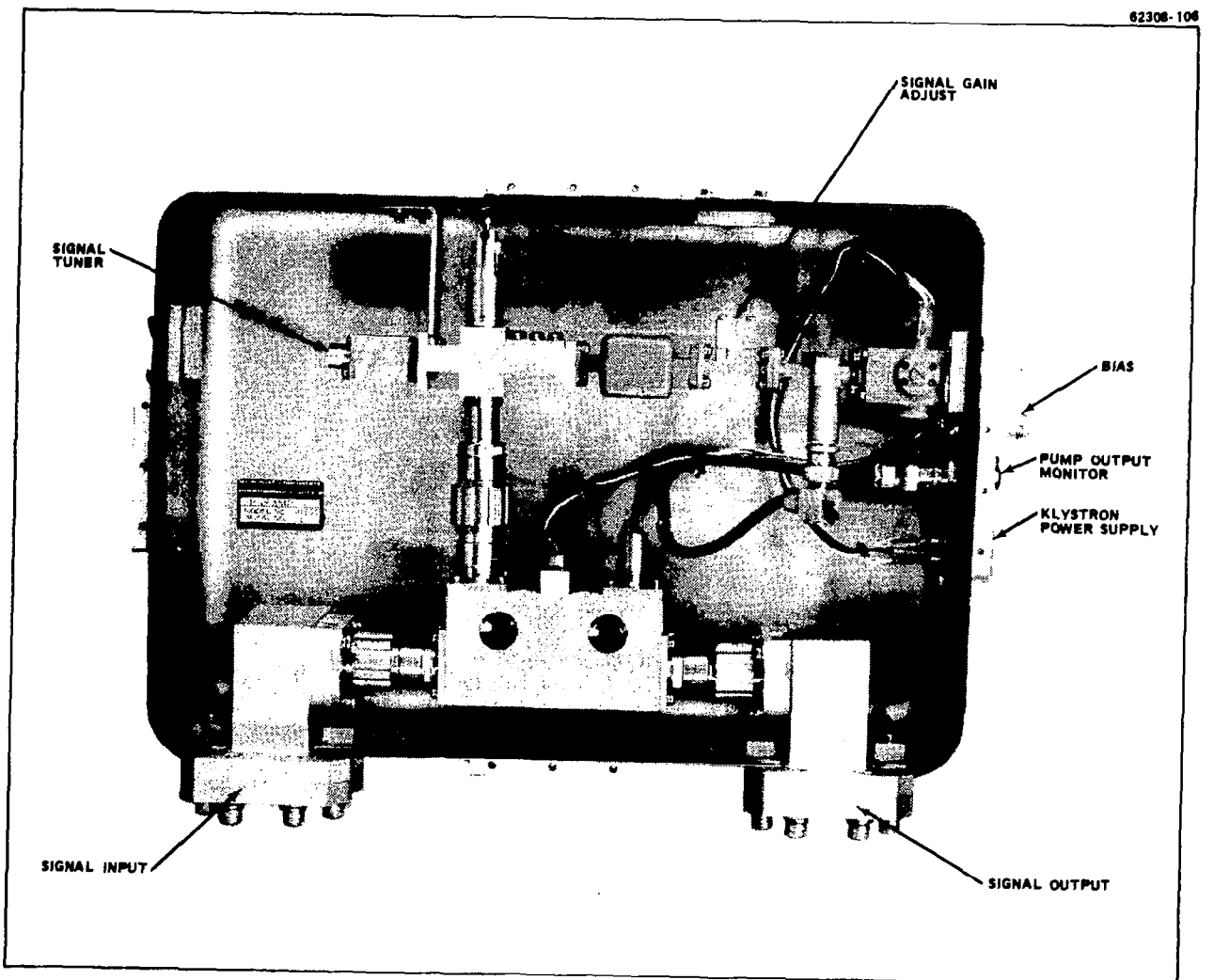


Figure 35. Parametric Amplifier

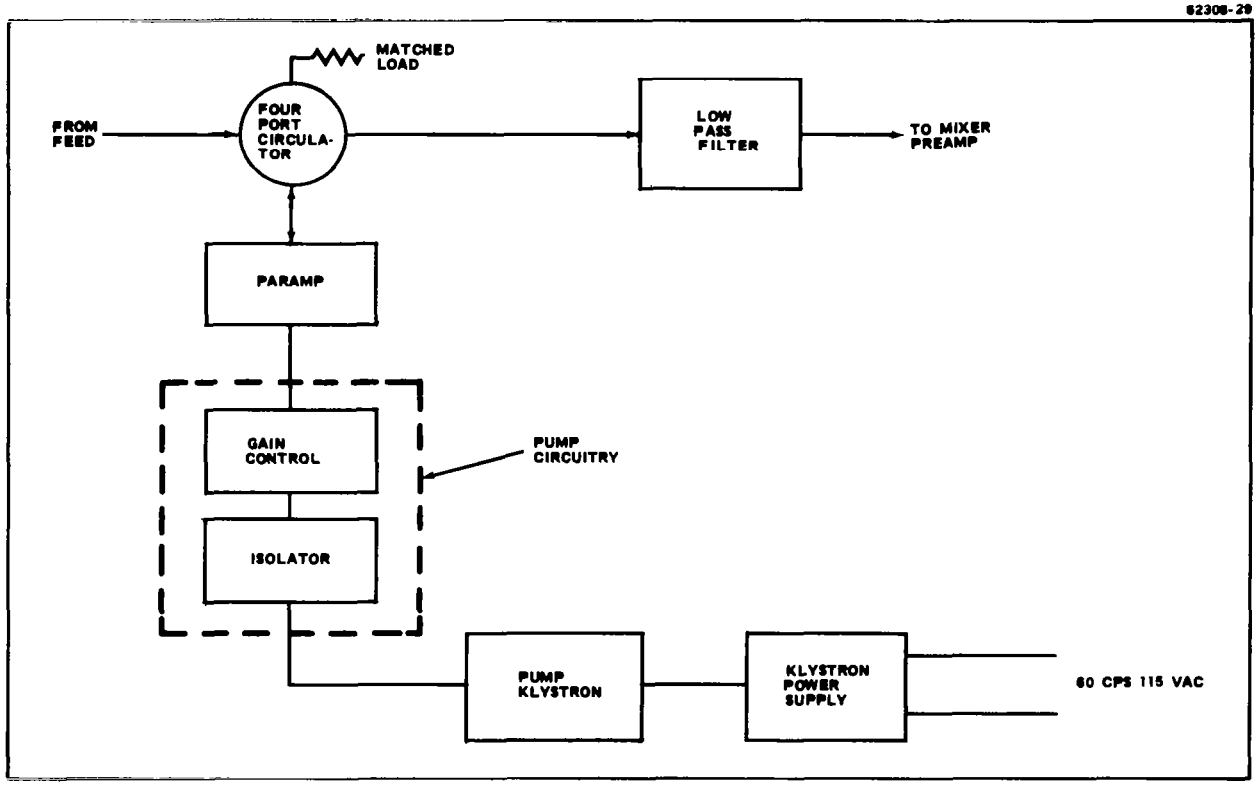


Figure 36. Block Diagram of Parametric Amplifier

MHz) is required, the top lid of the enclosure may have to be removed and the frequency tuning may have to be accomplished by adjusting both the signal tuner and the knurled nut located at the diode holder.

## 4.3 PERFORMANCE OF PARAMETRIC AMPLIFIER

Nominally, this parametric amplifier will provide a maximum of 1.6 dB noise figure operating at 20 dB gain and with a minimum 3 dB bandwidth of 30 mc. (specific data is shown in Table 18).

TABLE 18. NASA-GODDARD 4 GHz PARAMETRIC AMPLIFIER

| Freq. MHZ | Noise Figure (db) | 3 db Bandwidth (MHz) | Gain (db) |
|---|---|---|---|
| 4000 | 1.6 | 58 | 20 |
| 4050 | 1.6 | 46 | 20 |
| 4100 | 1.5 | 60 | 20 |
| 4150 | 1.5 | 37 | 20 |
| 4200 | 1.5 | 34 | 20 |

NOTE:

1. Self Bias with 1.1 meg. resistor
2. Above noise figure data includes 9.5 db second stage noise figure (bandpass filter and mixer).

Date: April 1, 1966

# 5.0 NOISE TEMPERATURE MEASUREMENTS

## 5.1 NOISE TEMPERATURE MEASURING EQUIPMENT

An accurate noise temperature measuring setup at the antenna test range located at Carbon Canyon was assembled. The block diagram of the equipment setup is shown in Figure 37. Figure 38 shows a preliminary run in elevation. The variations in the ambient and nitrogen cooled loads indicated that the system did not have long time stability.

The system was checked out completely to determine the accuracy, stability, and linearity of the setup. A number of problems were encountered during this phase. Linearity was affected by the following: (1) Saturation of the post amp and preamp if the gains were set too high, (2) the video detector in the post amp was not square-law over the signal level range initially being used, (3) the fast rise time of the square-wave modulation resulted in extremely large spikes in the 30 mc IF that saturated the amplifiers. Stability was obtained with the following techniques: (1) Voltage regulators were used in all items of equipment in the setup, (2) All equipment that was not required to be mounted near the antenna was placed on a stationary part of the antenna mount, (3) Paramp, mixer, and waveguide runs were securely tied down to prevent any mechanical strain resulting from the movement of the antenna mount which would cause the signal level to vary. After these problems were eliminated and the system was operating properly, noise temperature measurements were made. Continuous monitoring of the system stability, linearity, etc. were made throughout the tests. The complete equipment complement and its location is shown in Figure 39, 40, and 41.

## 5.2 CONTINUOUS PLOTS AND CALIBRATION OF ANTENNA NOISE TEMPERATURE

Repeated measurements of the noise temperature of the antenna versus elevation angle for various azimuth positions were made for several frequencies in the 4 GHz band. These measurements appear as continuous plots. The plots include the total noise of the system, but since the antenna temperature is the only variable, calibration points were added to indicate the antenna temperature.

Repeated measurements of the noise temperature of the antenna versus azimuth angle for various elevation positions were also made for several frequencies in the 4 GHz band. These measurements appear as continuous plots. These plots are the most interesting since they correlate closely with the horizon contour and known interference sources.

Measurements were made using the cold load reference (nitrogen cooled load) to establish accurate calibration of the temperature plots. During the calibration of

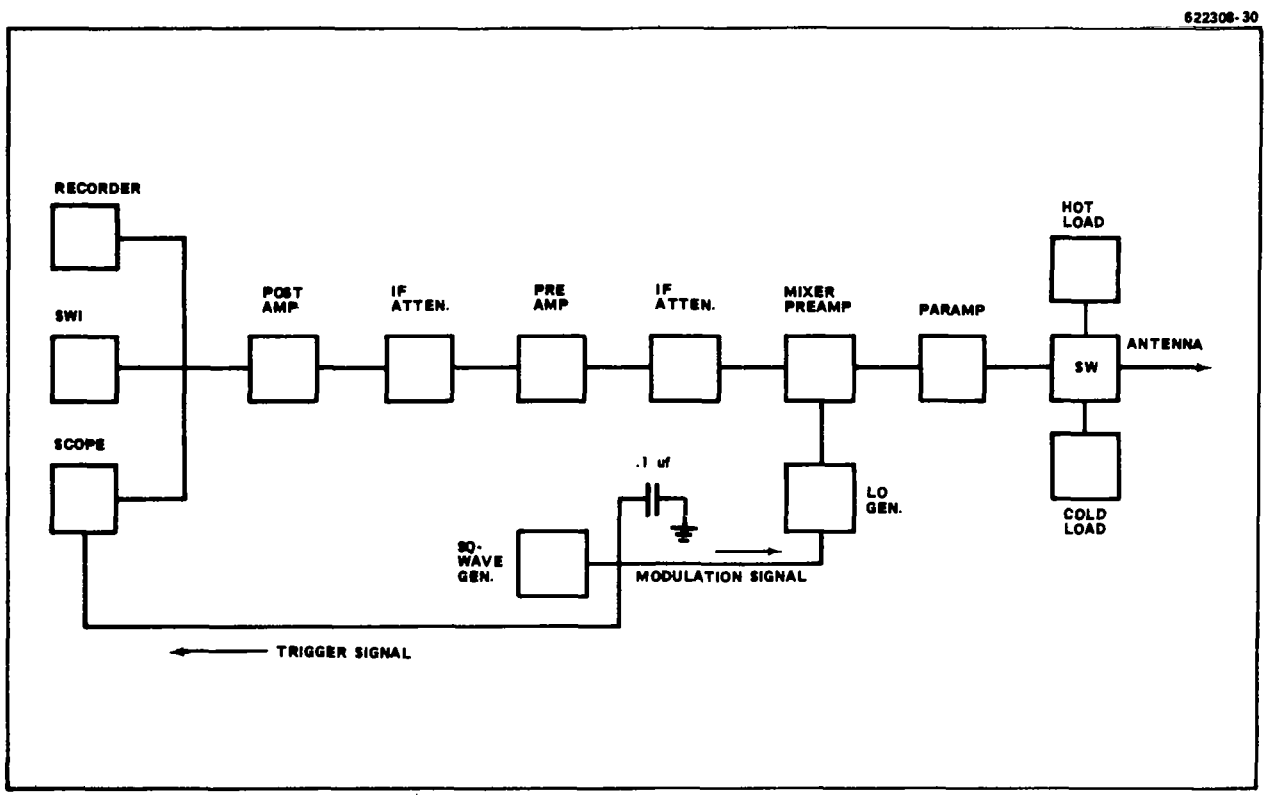


Figure 37. Block Diagram of Equipment Setup for Noise Temperature of NASA Five Horn Cassegrain System

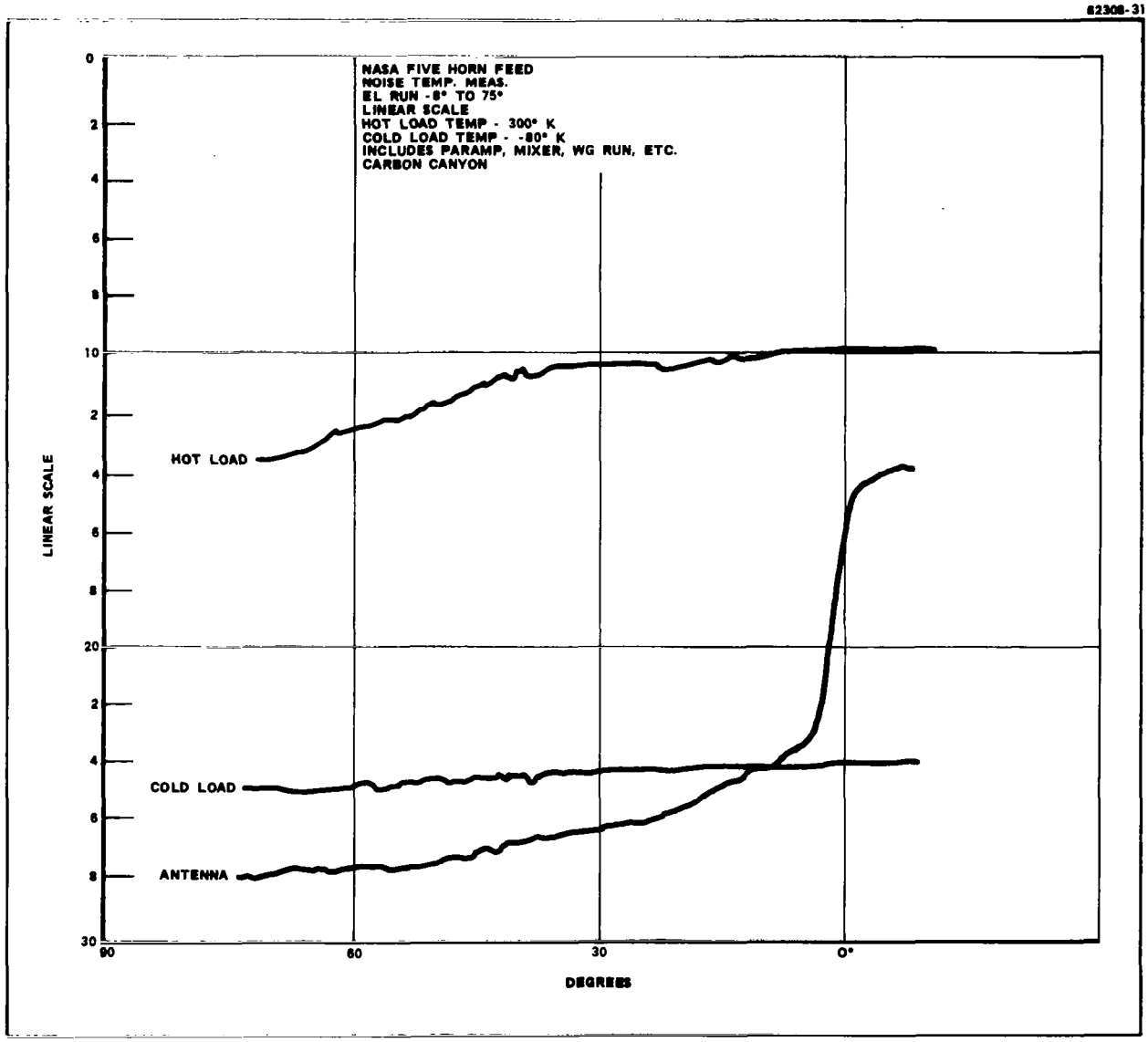


Figure 38. Preliminary Antenna Noise Temperature vs. Elevation Angle Continuous Plot

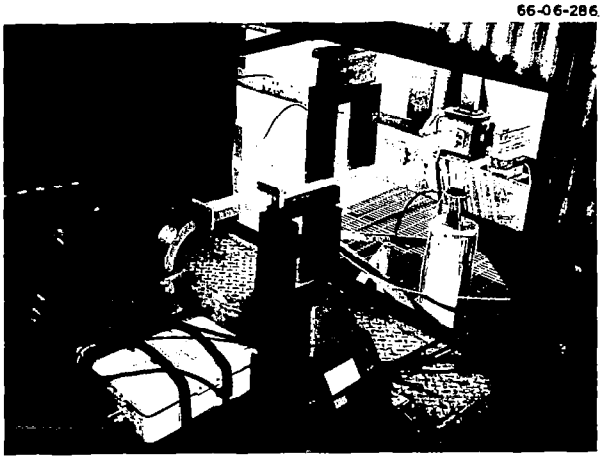


Figure 39. Noise Temperature Measuring Equipment Located on Moving Portion of Antenna Mount

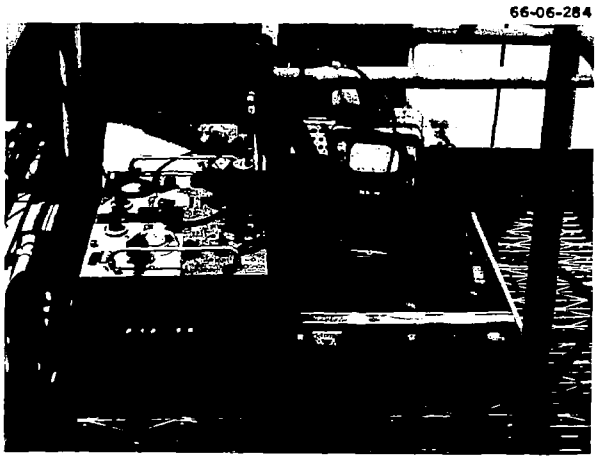


Figure 40. Noise Temperature Measuring Equipment Located on Stationary Portion of Antenna Mount

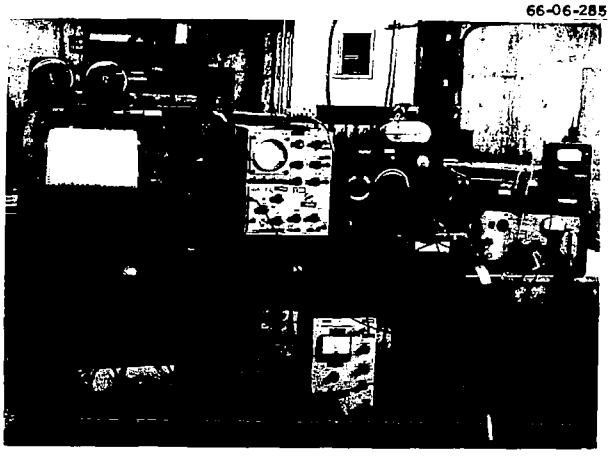


Figure 41. Noise Temperature Measuring Equipment Located in Silo

the continuous plots of antenna noise temperature two of problems were encountered:

(1) Initially, it was decided to calibrate the plots one at a time which required measurements at both high and low elevation angles. When tilting the antenna from a low to a high elevation angle, the liquid notrogen was dumped causing the temperature of the nitrogen cooled load to change so rapidly that accurate measurements could not be made. This problem was solved by making all low elevation measurements first and then inserting a 90 degree bend between the nitrogen cooled load and the waveguide switch when measuring the noise temperature at the high elevation angles.

(2) Water vapor condensed on the outside of the radome. This effectively lowers the isolation between the sum and the orthogonal arms of the OMT's resulting in a higher noise temperature of the antenna.

Before proceeding with the calibrations, the paramp was removed from the setup. The paramp was retuned and checked for the proper gain and noise temperature. Since the klystron has several modes of operation and the gain, stability, and noise temperature depends on the mode of operation, careful attention was given to the proper setting of the beam and reflector voltages of the klystron power supply.

Calibration of the continuous plots of antenna noise temperature versus elevation angle for various azimuth positions was accomplished. The calibration points were chosen at a -8 degrees and 75 degrees in elevation. These plots appear in the Appendix. At 75 degrees elevation, the average measured antenna noise temperature is 26.7°K which includes a 112-inch waveguide run.

Calibration of the continuous plots of antenna noise temperature versus azimuth angle for various elevation positions was accomplished. The calibration points were chosen where the noise temperature remained constant over a large rotation in azimuth. These plots appear in the Appendix.

## 5.3 NOISE TEMPERATURE OF THE SUN

The noise temperature of the sun was measured and the radiation pattern of the antenna using the sun as a source was taken. These radiation patterns appear in Figures 42 and 43 – one on a log scale and the other on a linear scale. The average effective noise temperature of the sun measured at the output of the sum channel is 3270°K. This gives a sun temperature of 53,500°K. The noise temperature of the moon was not made because visual contact (required to align antenna) could not be made due to cloud cover.

## 5.4 CORRELATION BETWEEN HORIZON AND CONTINUOUS PLOTS

Photographs of the horizon using regular film were taken on the clearest day that occurred during the month of June. The near horizon showed up clear, but the far horizon was lost in the haze. Infra-red film was ordered and additional photographs were taken to cover both the near and far horizon. These photographs appear in the Appendix. In Figure 44, the location of the photographs have been added to the azimuth run plot at an elevation of two degrees. The plot has a number of areas that are easily recognized in the photographs. A few of these areas are pointed out in both the photographs and the continuous plot.

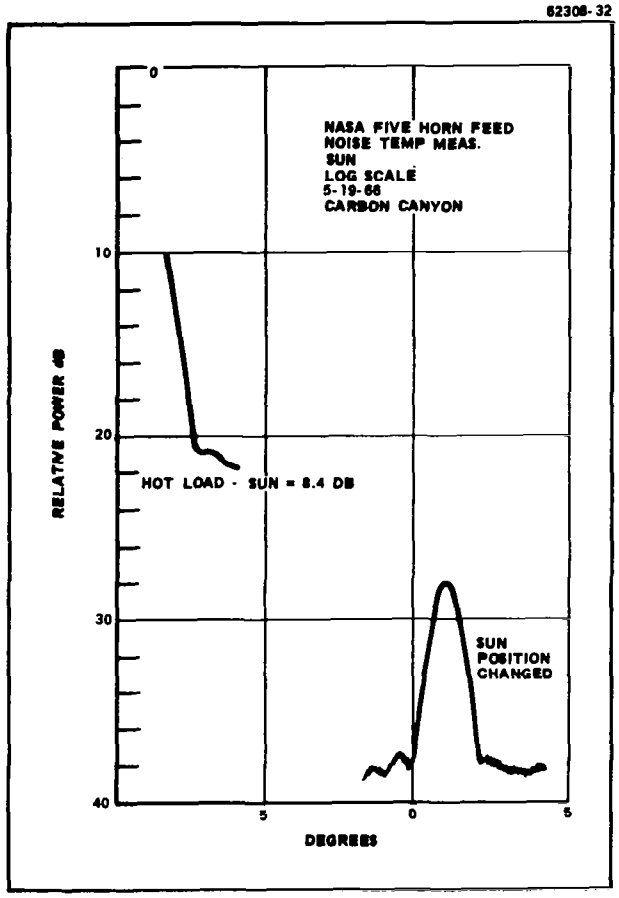


Figure 42. Radiation Pattern Using the Sun as the Source, Log Scale

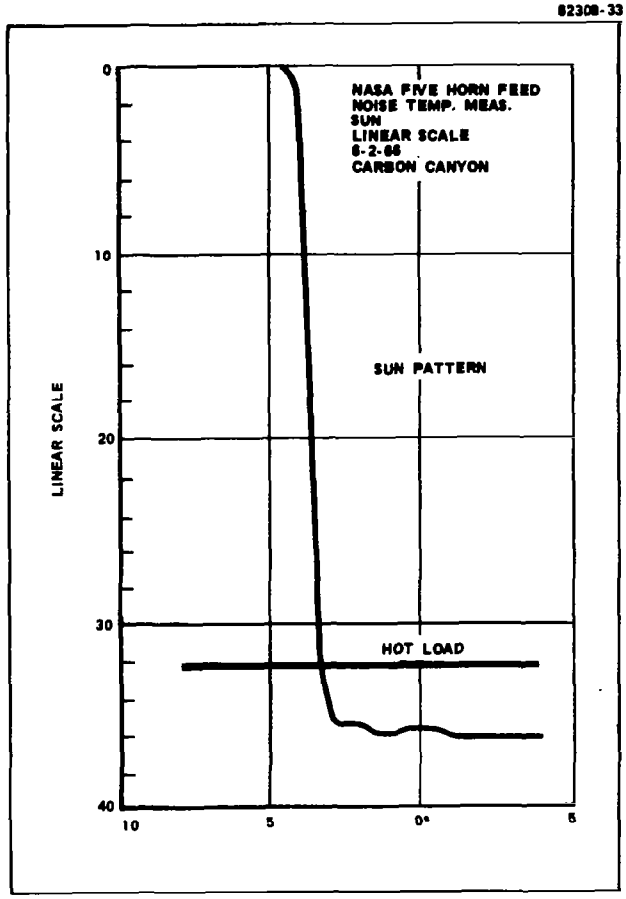


Figure 43. Radiation Pattern Using the Sun as the Source, Linear Scale

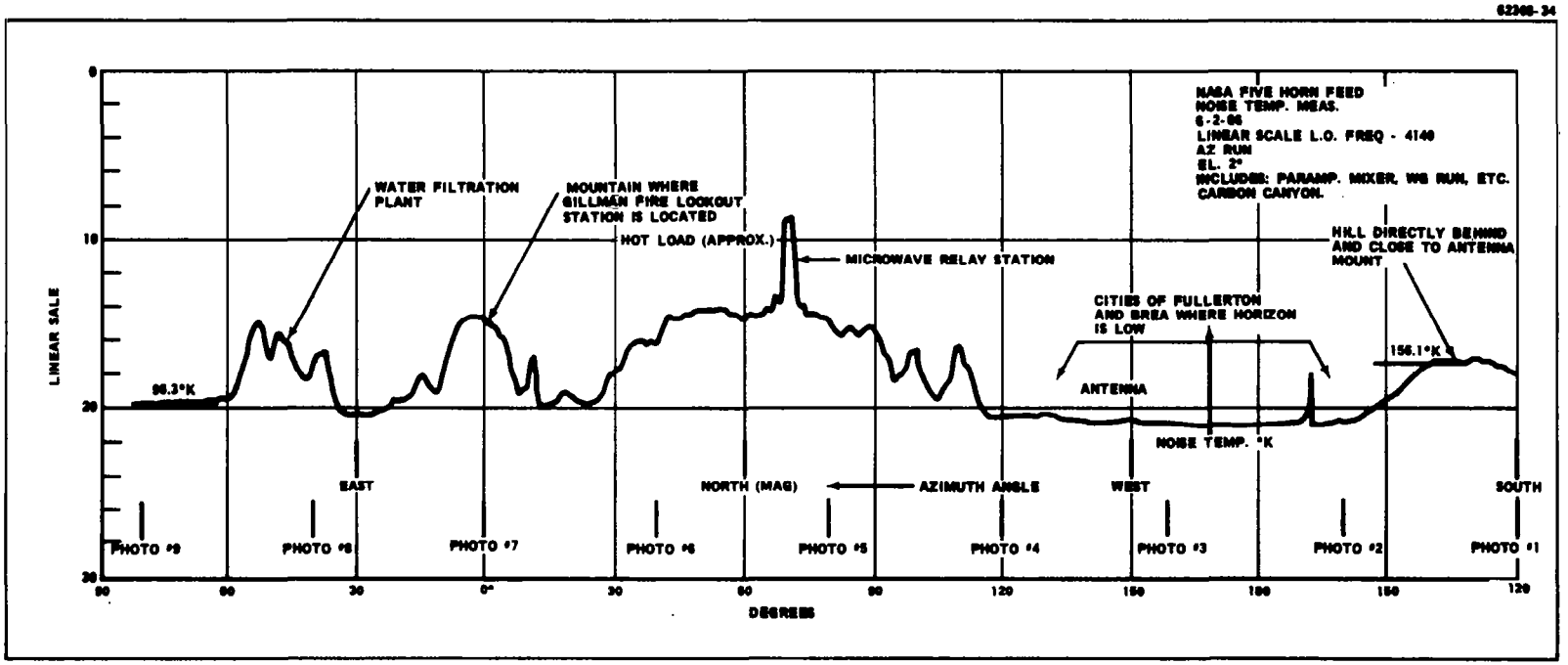


Figure 44. Antenna Noise Temperature vs. Azimuth Angle at an Elevation of Two Degrees

## 5.5 VERTEX MATCHING TO IMPROVE NOISE TEMPERATURE

The imperfect isolation between the sum channel and the orthogonal arm of the OMT, due to reflection from the subreflector back into the feed, contributes 4.6°K to the antenna noise temperature. Since this is a relatively large contributor, additional matching at the vertex of the hyperboloid would improve the antenna noise temperature. An improved match was obtained with the use of a flat plate, approximately 5.5 inches in diameter placed directly in front of the vertex as shown in Figure 45.

Using this matching plate, the noise contributed by this factor is reduced to less than 1°K. Since the matching was accomplished after the antenna was removed from the antenna test mount, radiation patterns using the new vertex plate were not evaluated. Both vertex plates were shipped with the antenna. The conical vertex plate will be installed in the hyperboloid, and the flat one may be used if a lower noise temperature is desired.

## 5.6 ANTENNA NOISE TEMPERATURE AND CONTRIBUTING FACTORS

The antenna was removed from the mount and placed in a zenith position on the ground. The measured antenna noise temperature at the zenith position at the sum channel output of the feed is 19.0°K. The subreflector was removed and the feed noise temperature was measured repeatedly. The average value is 9.3°K. Assuming a sky temperature of 3.5°K at 4 GHz and a calculated value of 0.6°K from the loaded orthogonal arms of the OMT's (based on the measured isolation of the feed) the noise temperature contribution from the resistive loss of the feed is 5.2°K or .076 dB loss. From the above information, the noise contributed from the spillover past the perimeter of the dish hitting the ground is calculated to be 5.8°K or a spillover of 2.3 percent. The waveguide run used in the calibration of the continuous plots has a noise temperature of 7.4°K. The measured values and calculated values based on measurements for the various components contributing to the noise temperature fall within the limits of the theoretically predicted values. Tabulation of the results are given in Table 19.

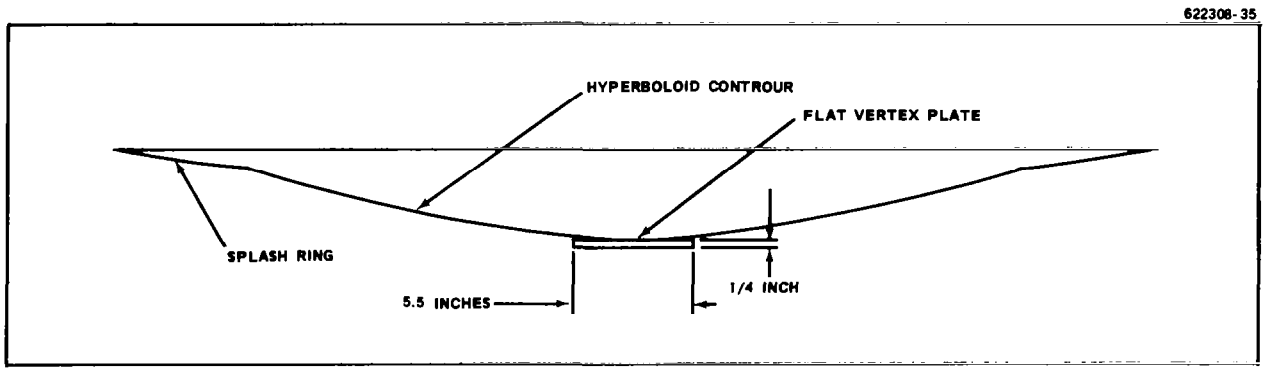


Figure 45. Improved Matching Vertex Plate

## TABLE 19 MEASURED AND EXPECTED ANTENNA NOISE TEMPERATURE AND CONTRIBUTING FACTORS

| Contributing factors to the antenna noise temperature | Meas. | Theor |
|---|---|---|
| (1) Sky – 97.9% of input noise coming from sky | | |
| 3.75°K sky at 75° elevation | 3.7°K | same as meas. |
| 3.5°K sky at zenith | 3.4°K | same as meas. |
| (2) Paraboloid spillover | | |
| 2.3% of input noise coming from 250°K ground | 5.8°K | same as meas. |
| (3) 112 – inch waveguide – loss of .03 – .06 dB/meter at 300°K | 7.4°K | 5.7° -11.7°K |
| (4) Feed loss – 68 inches of waveguide at .03 – .06 dB/meter at 300°K | 5.2°K | 3.6° -7.2°K |
| (5) Isolation | | |
| (a) feed in free space | same as theor. | .6°K |
| (b) feed installed in reflector using conical vertex plate (based on measured – isolation between sum and orth-arms of OMT's) | same as theor. | 4.6°K |
| (c) feed installed in reflector using flat vertex plate (based on measured isolation between sum and orth-arms of OMT's) | same as theor. | 1°K |
| **Antenna Noise Temperature** | | |
| (1) antenna noise temperature at output of 112-inch waveguide run at 75° elevation with conical vertex plate | 26.7°K | 23.4-33.0°K |
| (2) antenna noise temperature at the feed sum channel output with conical vertex plate at zenith | 19.0°K | 17.4°-21.0°K |
| (3) improved antenna noise temperate at the feed dun channel output with flat vertex plate at zenith | 15.4°K | 13.8°-17.4°K |

## 6.0 POLARIZATION CONTROL

### 6.1 TECHNIQUE

The signal loss caused by a polarization mismatch can be eliminated by controlling the polarization ellipse of the ground antenna on both transit and receive. Referring to Figure 46, the polarization ellipse may be expressed as

$$\frac{E_x^2}{E_1 \sin^2 \theta} - \frac{2 E_x E_y \cos \theta}{E_1 E_2 \sin^2 \theta} + \frac{E_y^2}{E_2^2 \sin^2 \theta} = 1$$

where $E_1$ and $E_2$ are two space orthogonal field and theta, $\theta$, is the time phase between the field. From this it can be shown that any sense of polarization – linear, elliptical and circular – can be obtained by the proper choice of time phase, $\theta$, and the relative amplitude of the two fields.

Linear polarization is obtained by setting the time phase equal to zero giving

$$\frac{E_x}{E_1} = \frac{E_y}{E_2}$$

where the angle of tilt is given by

$$\tan \theta = \frac{E_1}{E_2}$$

Circular polarization is obtained by setting the time phase equal to $90^o$ and maintaining equal amplitude. The equation of the ellipse reduced to

$$\frac{E_x^2}{E_1^2} + \frac{E_y^2}{E_2^2} = 1$$

Elliptical polarization is obtained by varying the time phase and the relative amplitude of the two fields.

### 6.2 PERFORMANCE

This technique was implemented with the use of a power divider, phase shifter and an OMT. The block diagram of the setup is shown in Figure 47. Data was taken for various setting of the phase shifter and power divider. The axial ratio of the circular polarized wave produced by this setup was better than 0.1 dB. The linear

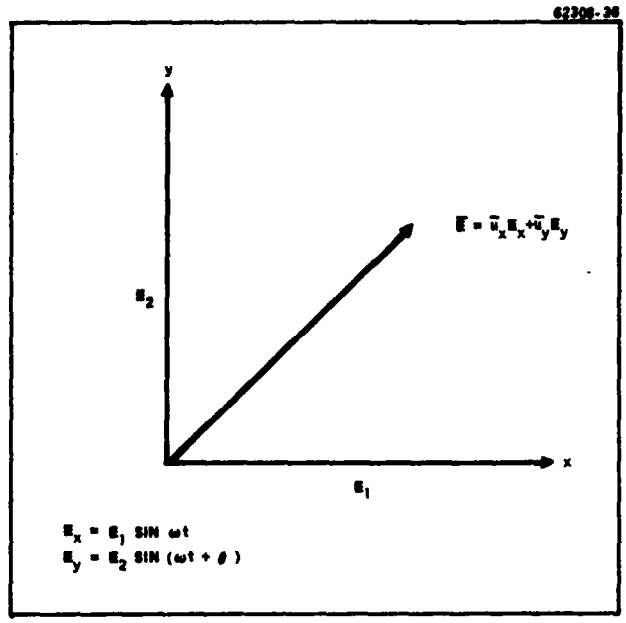


Figure 46. Components of Elliptically Polarized Wave

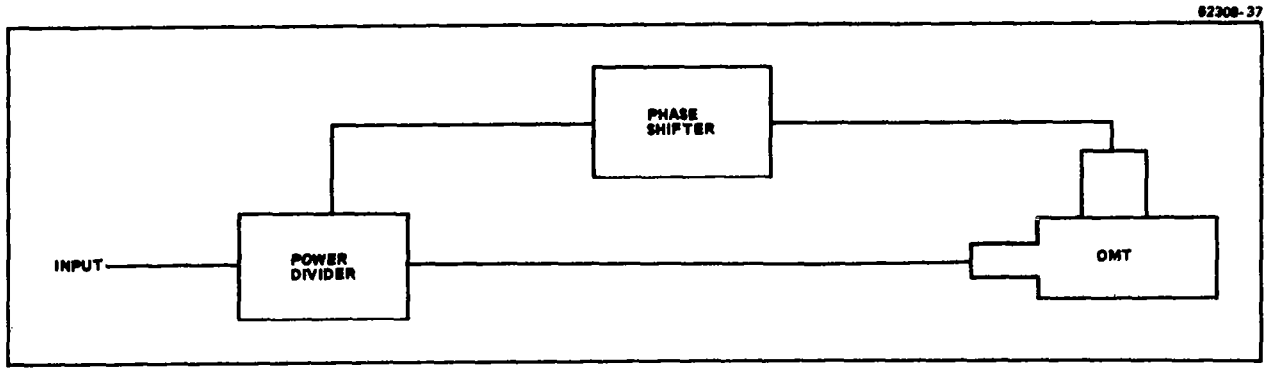


Figure 47. Block Diagram of Setup to Obtain Any Sense of Polarization

polarization had better than a 30 dB axial ratio. Table 20 shows the data taken to produce rotable linear polarization. The phase shifter was set to give a zero time phase between the two orthogonal fields and the power divider changed to vary the relative amplitude of the two fields.

TABLE 20. ROTATABLE LINEAR POLARIZATION AT 7750 MHz

| Short Position of Pwr Div. (Wavelength) | Percent PWR to Normal Arm of OMT | Measured Direction of Pol. | Theoretical Direction of Pol. | Axial Ratio (dB) |
|---|---|---|---|---|
| 0 | 100 % | 0 | 0 | $30^+$ |
| 1/16 | 14.7% | $20^o$ | $22.5^o$ | $30^+$ |
| 1/8 | 50 % | $45^o$ | $45^o$ | $30^+$ |
| 3/16 | 85.4% | $70^o$ | $67.5^o$ | $30^+$ |
| 1/4 | 0 % | $90^o$ | $90^o$ | $30^+$ |

One method of generating elliptical polarization was verified. This involves equalizing the amplitudes and varying the time phase between the two fields. The major axis of the ellipse should be at a $\pm 45^o$. The axial ratio is then given by

$$A.R. = 20 \log \left[ \frac{1 + \cos \theta}{1 - \cos \theta} \right]^{1/2}$$

Data taken for this method is presented in Table 21.

TABLE 21. ELLIPTICAL POLARIZATION BY VARYING THE TIME PHASE AT 7750 MHz

| Short Position of Pwr Div. (Wavelength) | Percent PWR to Normal Arm of OMT | Phase Shift | Major Axis Dir. | Meas. Axial Ratio (dB) | Theor. Axial Ratio (dB) |
|---|---|---|---|---|---|
| 1/8 | 50% | $45^o$ | $45^o$ | 7.5 | 7.7 |
| 1/8 | 50% | $70^o$ | $45^o$ | 3.5 | 3.1 |
| 1/8 | 50% | $90^o$ | $45^o$ | .07 | 0 |
| 1/8 | 50% | $110^o$ | $-45^o$ | 2.6 | 3.1 |
| 1/8 | 50% | $135^o$ | $-45^o$ | 6.4 | 7.7 |

Another method of generating elliptical polarization can be accomplished by maintaining a $90^o$ time phase and varying the relative amplitude of the two fields. The major axis will then lie on the $0^o$ line and the axial will be given by

$$A.R. = 20 \log \frac{E_1}{E_2}$$

The tilt of the major axis can be controlled by unbalancing the amplitudes of the fields and varying the time phase or by setting the time phase to a value other than $90^o$ and varying the relative amplitudes of the two fields.

# 7.0 CONCLUSIONS AND RECOMMENDATIONS

## 7.1 CONCLUSIONS

Development of the five horn feed has resulted in a new technique for achieving high efficiency performance of a 6 GHz transmitting and 4 GHz tracking feed. Although the present feed is limited to operation at 4 GHz, it is possible to extend the operation to 6 GHz with the further development of a 6/4 orthomode transducer. Primary patterns taken experimentally indicate that overall antenna efficiency at both frequencies of better than 50 percent should be attainable, and this was indeed demonstrated to be true at 4 GHz where an overall antenna efficiency of 56 percent was measured in the 15 foot dish.

Excellent noise temperature performance was also demonstrated at 4 GHz. The overall zenith antenna noise temperature measured was about 19°K, which compares well with other state of the art tracking antennas. In view of the results obtained, it may be stated that a very useful and high performance feed design has been achieved as a result of this investigation.

## 7.2 RECOMMENDATIONS

As several months of the contract period were spent developing the approach used for design of the five horn feed, there was not sufficient time for a thorough theoretical analysis of the feed system. Hence, the present feed may not be the most optimum geometrical configuration. Further investigation should be made to determine the optimum parameters such as size of outer and center horns, spacing between horns, and illumination of the horns and broadband multimoding in a common aperture. This analysis requires a rather detailed computer analysis, and should be the first step toward further development.

Also, a broadband 6/4 GHz orthomode transducer should be developed to extend the performance of the feed to 6 GHz. A program to develop the required components and a new feed optimum for 6/4 GHz performance would be desirable. Such a feed should be considered for a dish at least 30 feet in diameter or larger to alleviate the restricted packaging volume imposed by the 15 ft reflector used in the present program.

## NEW TECHNOLOGY

This report has covered in detail a description of the theory and operation of a five horn Cassegrain monopulse feed capable of operation in two frequency bands. This feed is considered a substantial improvement in the state of the art of dual frequency feeds. As this item has been sufficiently described in the report, no further comments will be made here. Formal reporting as required under the contract "New Technology Clause" will be made from the Hughes General Patent Office.

## APPENDICES

1. Primary Sum Channel Radiation Patterns
2. Primary Cross Polarized Radiation Patterns
3. Primary Azimuth Error Radiation Patterns
4. Primary Elevation Error Radiation Patterns
5. Center Horn at 6 KMC Radiation Patterns
6. Isolation – Feed in Free Space
7. Secondary Sum Channel RCP Radiation Patterns (with Splash Plate)
8. Secondary Cross Polarized Radiation Patterns (with Splash Plate)
9. Secondary Azimuth Error RCP Radiation Patterns (with Splash Plate)
10. Secondary Elevation Error RCP Radiation Patterns (with Splash Plate)
11. Secondary Linear Polarized Radiation Patterns (with Splash Plate)
12. Data Sheet for Sperry Reflex-Klystron
13. Continuous Plots of Antenna Noise Temperature Verus Azimuth Angle
14. Continous Plots of Antenna Noise Temperature Verus Elevation Angle
15. Photographs of Horizon at Carbon Canyon Test Range

# 1. PRIMARY SUM CHANNEL RADIATION PATTERNS

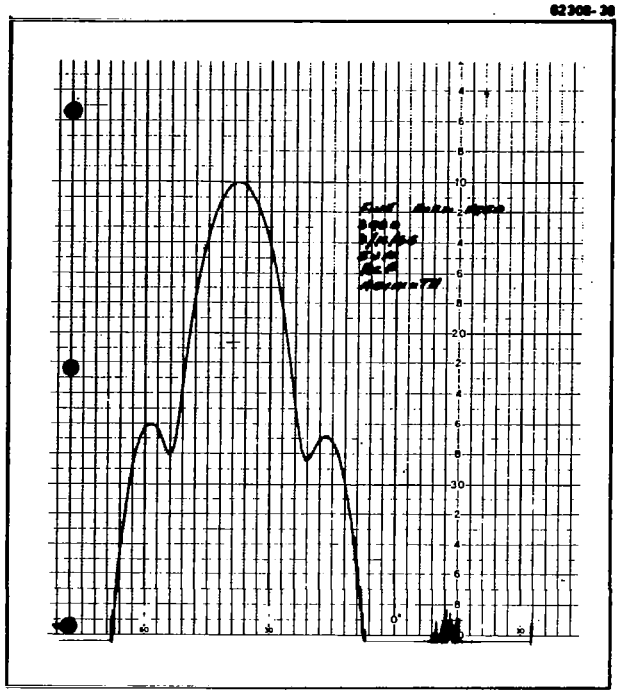

Five Horn Feed-3900-RCP-Azimuth

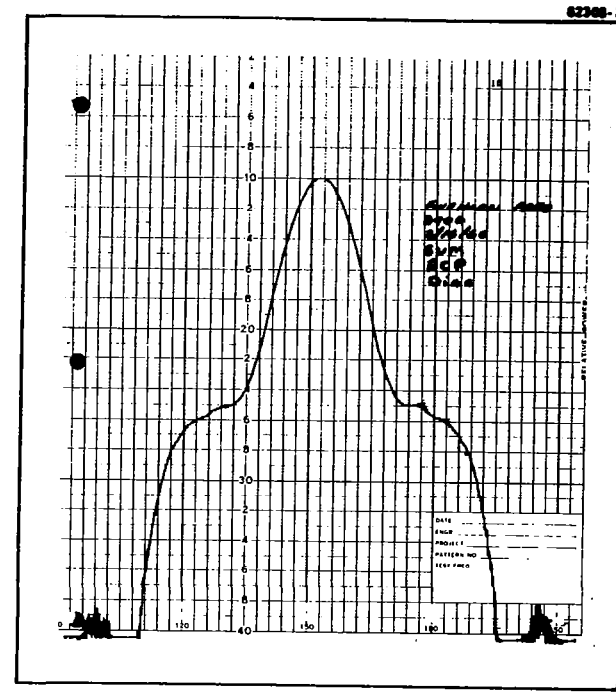

Five Horn Feed-3900-RCP-Diagonal

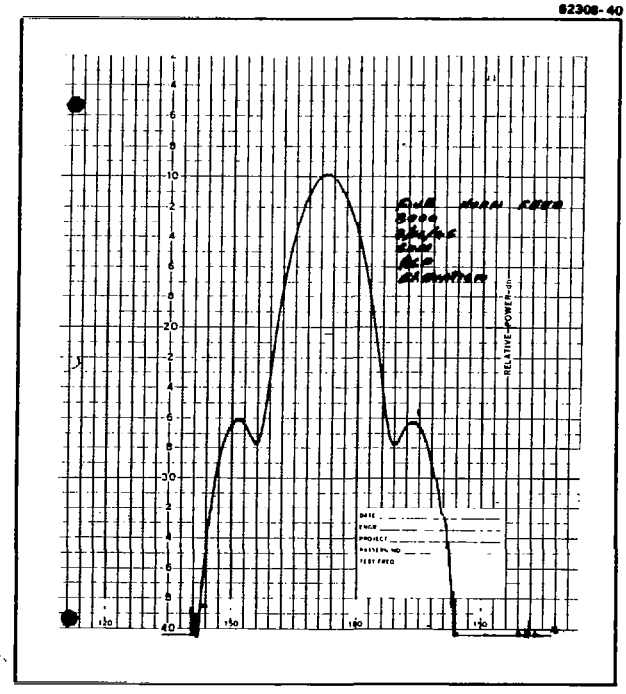

Five Horn Feed-3900-RCP-Elevation

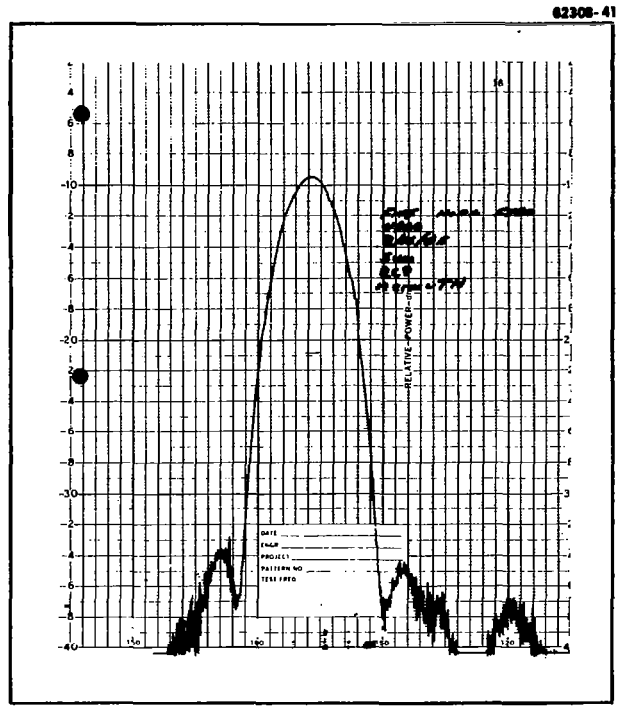


Five Horn Feed-4100-RCP-Azimuth

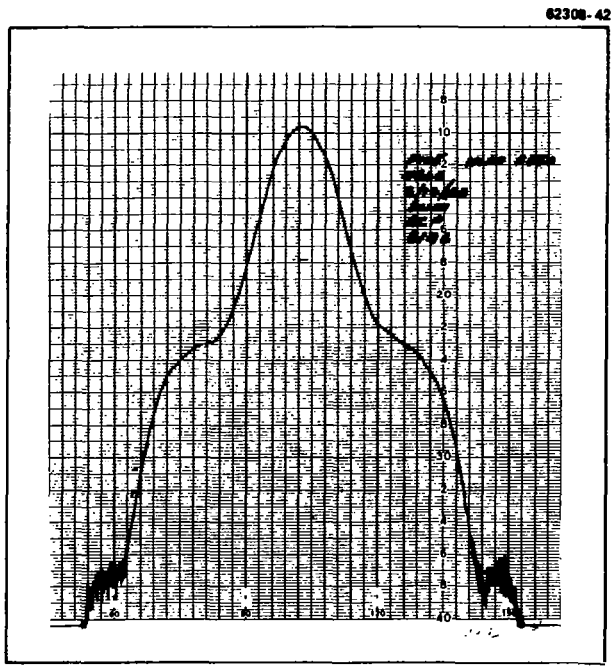


Five Horn Feed-4100-RCP-Diagonal

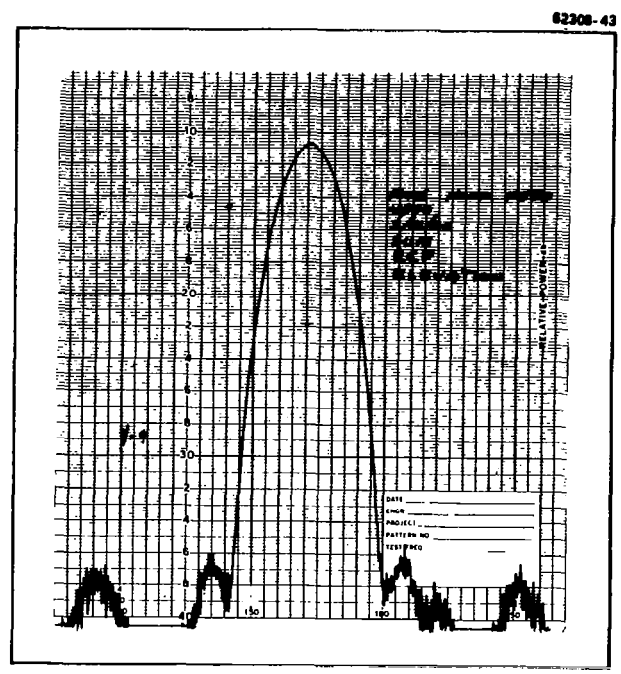


Five Horn Feed-4100-RCP-Elevation

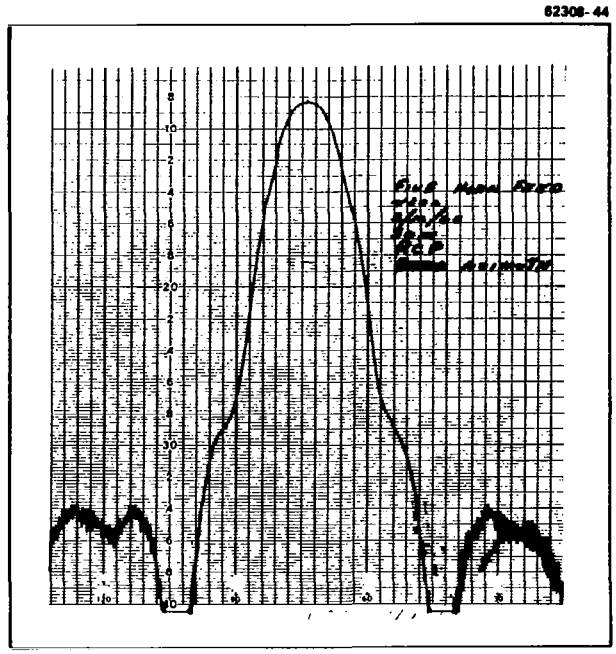


Five Horn Feed-4300-RCP-Azimuth

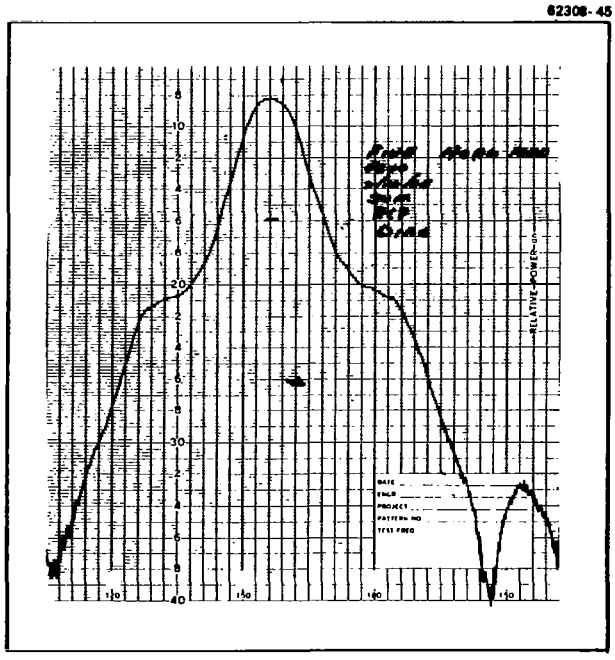


Five Horn Feed-4300-RCP-Diagonal

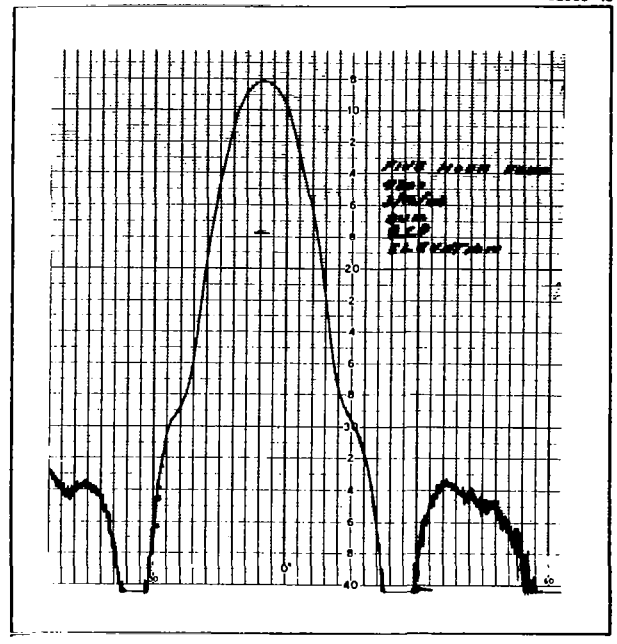


Five Horn Feed-4300-RCP-Elevation

## 2. PRIMARY CROSS POLARIZED RADIATION PATTERNS

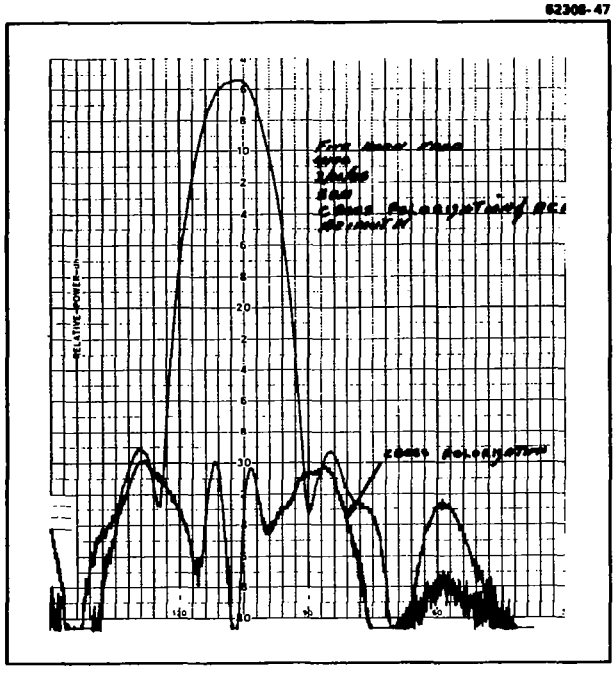


Five Horn Feed-4100-Cross
Polarization & RCP – Azimuth

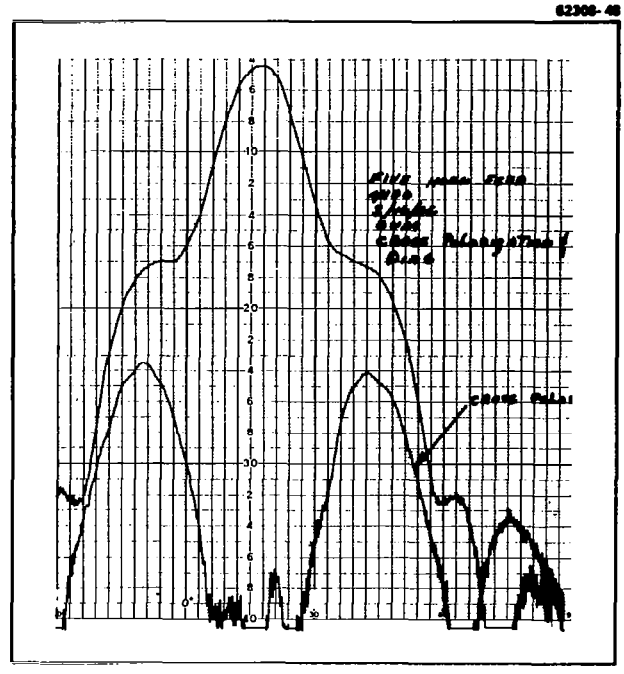


Five Horn Feed-4100-Cross
Polarization & RCP – Diagonal

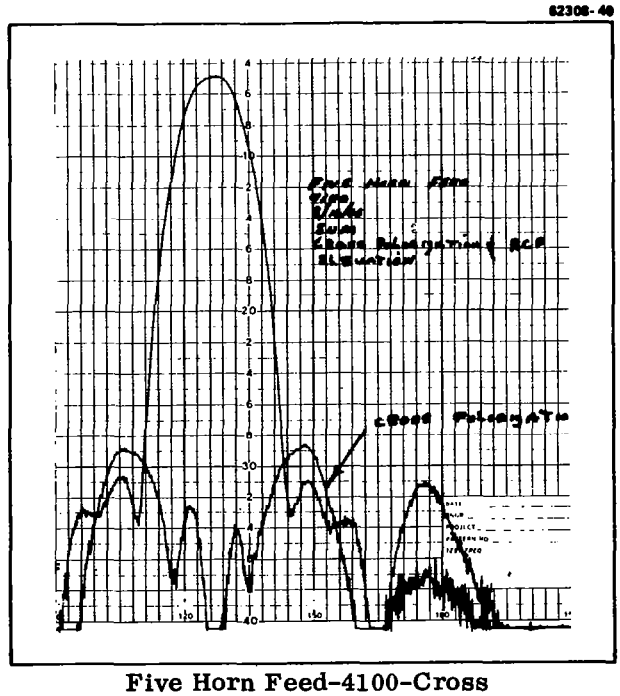


Five Horn Feed-4100-Cross
Polarization & RCP – Elevation

# 3. PRIMARY AZIMUTH ERROR RADIATION PATTERNS

62308-50

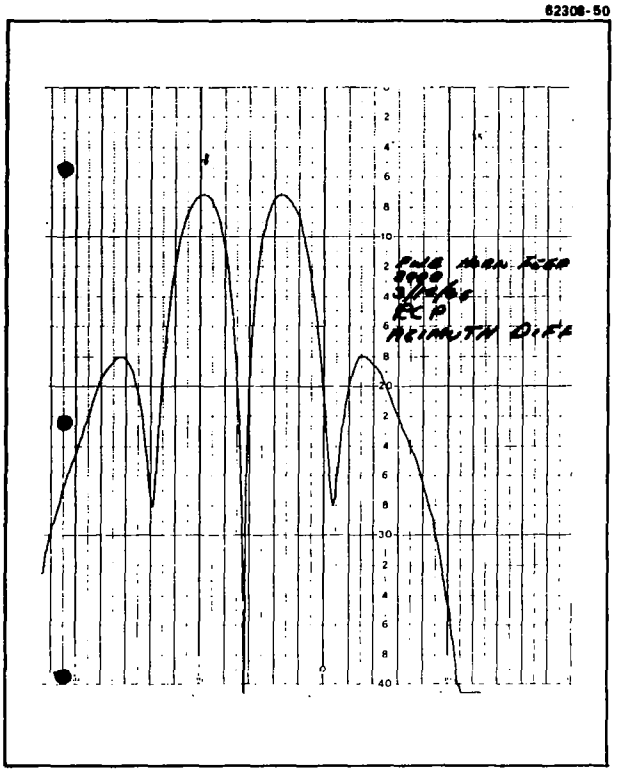

Five Horn Feed-3900-RCP-Azimuth Difference

62308-51

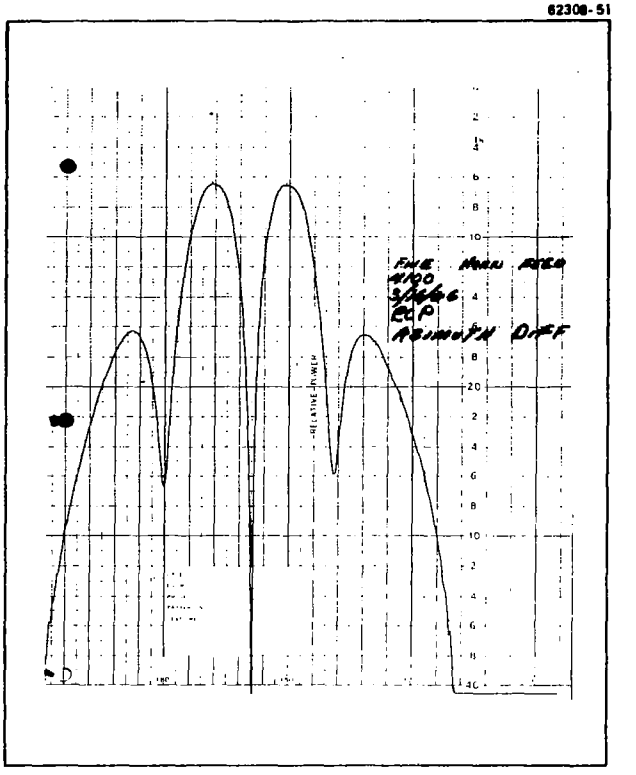

Five Horn Feed-4100-RCP-Azimuth Difference

62308-52

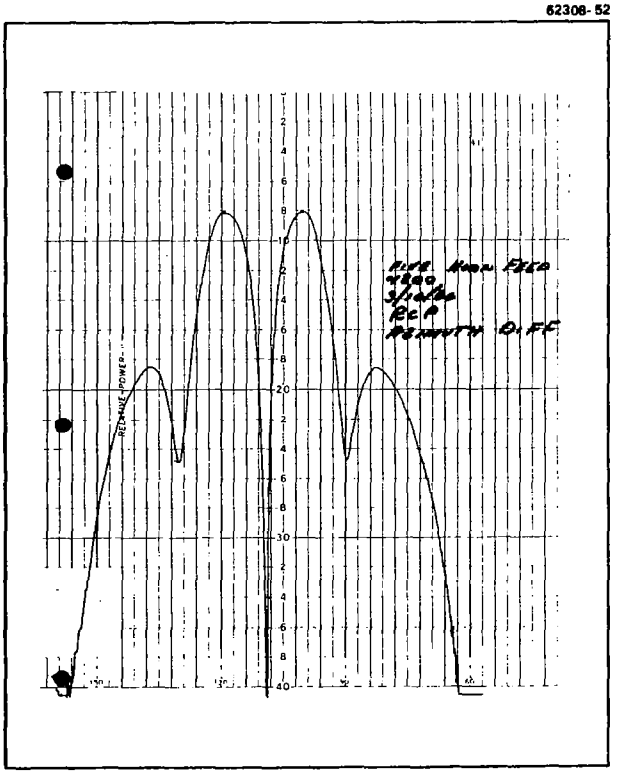

Five Horn Feed-4300-RCP-Azimuth Difference

# 4. PRIMARY ELEVATION ERROR RADIATION PATTERNS

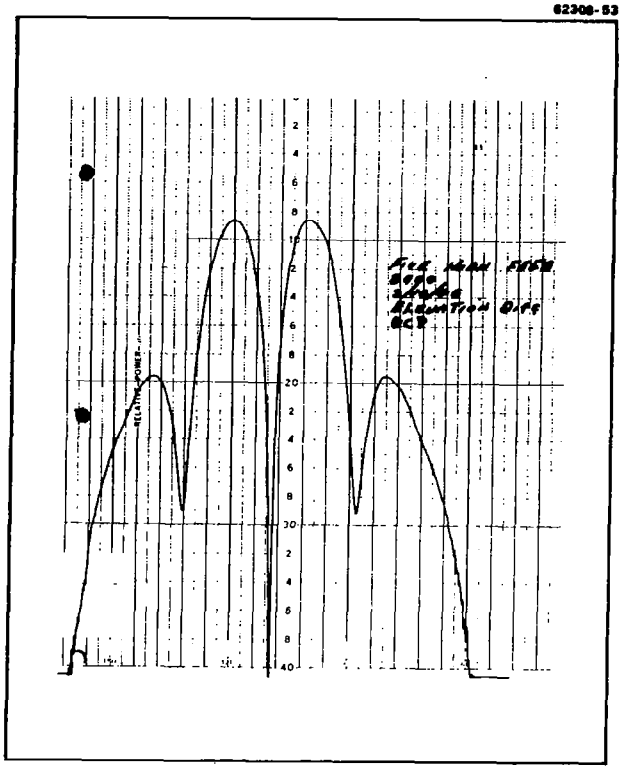


Five Horn Feed-3900-RCP-Elevation Difference

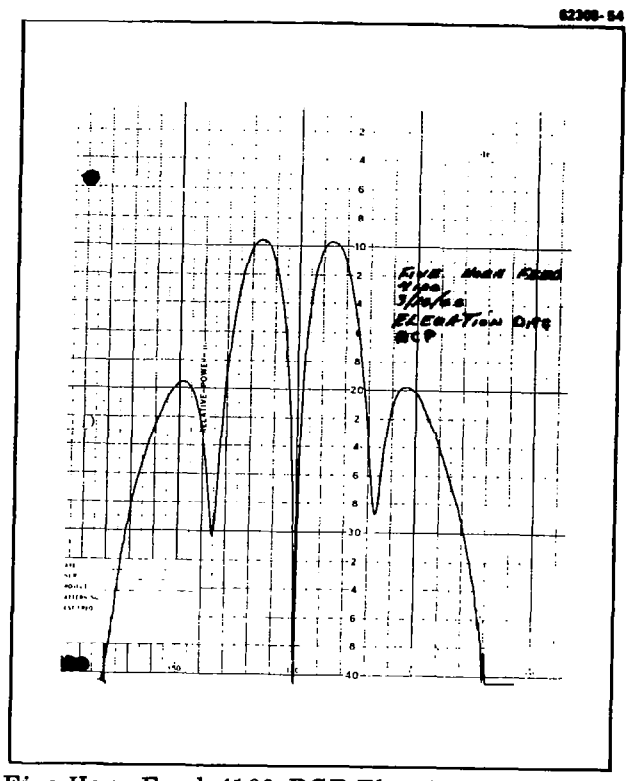


Five Horn Feed-4100-RCP-Elevation Difference

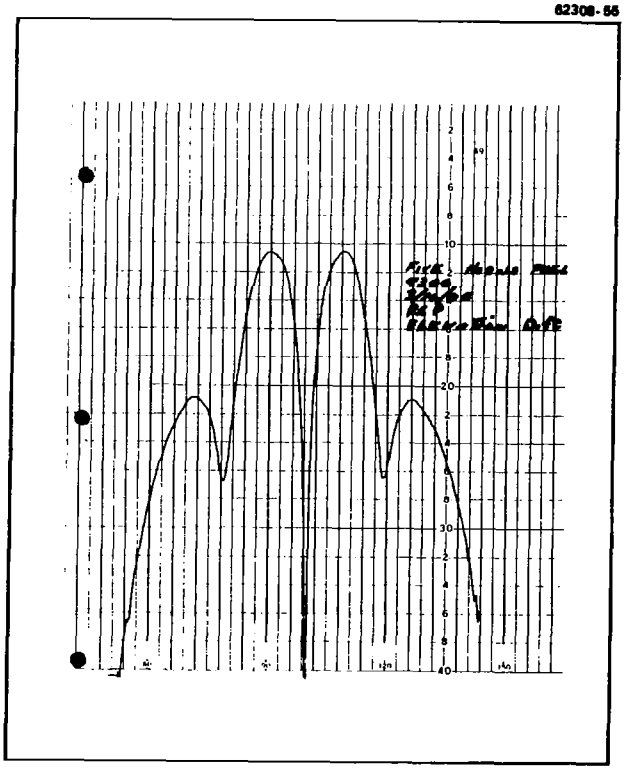


Five Horn Feed-4300-RCP-Elevation Difference

# 5. CENTER HORN AT 6 KMC RADIATION PATTERNS

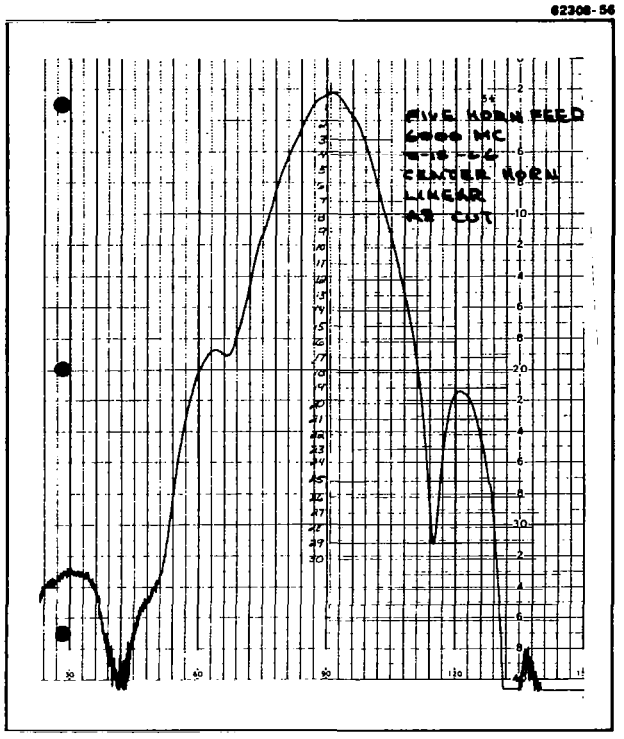


Five Horn Feed 6000 MC Center Horn – Linear – Azimuth

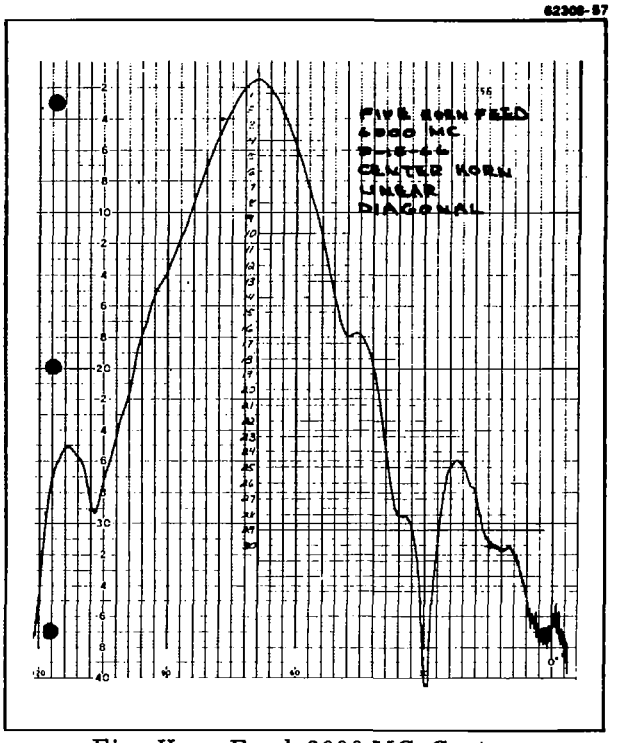


Five Horn Feed-6000 MC-Center Horn – Linear – Diagonal

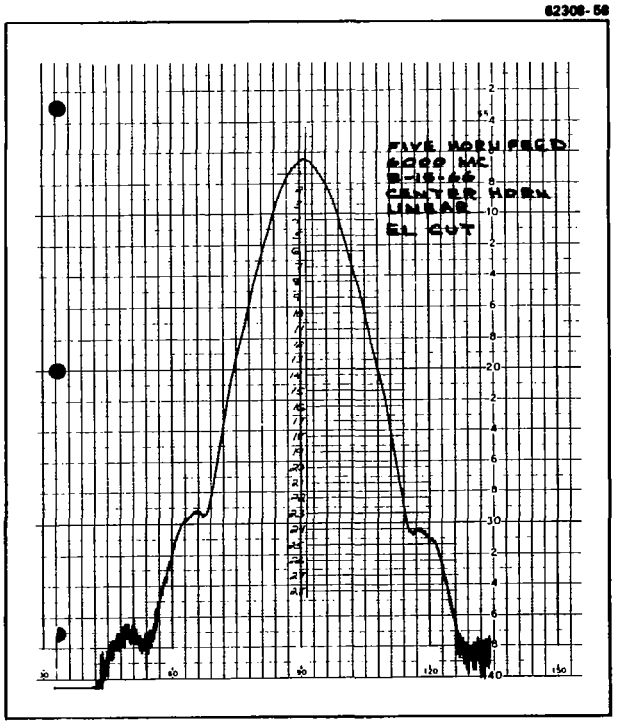


Five Horn Feed-6000 MC-Center Horn – Linear – Elevation

# 6. ISOLATION – FEED IN FREE SPACE

EXPERIMENTAL DATA SHEET

Project NASA - FIVE HORN Date 3/17/66

Item FEED - ISOLATION Page 1 of 3

G. Burnett

Sketch and Notes: Primary

| | Sum | | AZ | | EL | | X DIFF | |
|---|---|---|---|---|---|---|---|---|
| Sum | | | | | | | | |
| 3900 | | | | 50+ | | 47.8 | | 38.3 |
| 4000 | | | | 50+ | | 41.8 | | 32.5 |
| 4100 | | | | 50+ | | 39.3 | | 33.5 |
| 4200 | | | | 49.0 | | 50+ | | 35.2 |
| 4300 | | | | 50+ | | 43.9 | | 34.0 |
| AZ | | | | | | | | |
| 3900 | | | | | | 32.8 | | 50+ |
| 4000 | | | | | | 34.5 | | 38.9 |
| 4100 | | | | | | 34.7 | | 41.4 |
| 4200 | | | | | | 34.4 | | 34.9 |
| 4300 | | | | | | 34.0 | | 34.8 |
| EL | | | | | | | | |
| 3900 | | | | | | | | 47.2 |
| 4000 | | | | | | | | 48.7 |
| 4100 | | | | | | | | 50+ |
| 4200 | | | | | | | | 50+ |
| 4300 | | | | | | | | 50+ |

EXPERIMENTAL DATA SHEET

Project NASA - FIVE HORN Date 3/8/66

Item FEED - ISOLATION Page 3 of 3

G. Burnett

Sketch and Notes: Primary

| | Sum | | AZ | | EL | | | |
|---|---|---|---|---|---|---|---|---|
| OMT 4 | | | | | | | | |
| 3900 | | 39.7 | | 41.5 | | 38.2 | | |
| 4000 | | 41.1 | | 40.3 | | 46.6 | | |
| 4100 | | 41.3 | | 43.1 | | 48.8 | | |
| 4200 | | 44.6 | | 45.4 | | 47.3 | | |
| 4300 | | 43.6 | | 50+ | | 50+ | | |
| CENT OMT | | | | | | | | |
| 3900 | | 40.3 | | 50+ | | 50+ | | |
| 4000 | | 30.5 | | 50+ | | 50+ | | |
| 4100 | | 30.3 | | 50+ | | 50+ | | |
| 4200 | | 34.2 | | 50+ | | 50+ | | |
| 4300 | | 35.6 | | 50+ | | 50+ | | |
| | | | | | | | | |
| | | | | | | | | |
| | | | | | | | | |
| | | | | | | | | |

# 7. SECONDARY SUM CHANNEL RCP RADIATION PATTERNS (WITH SPLASH PLATE)

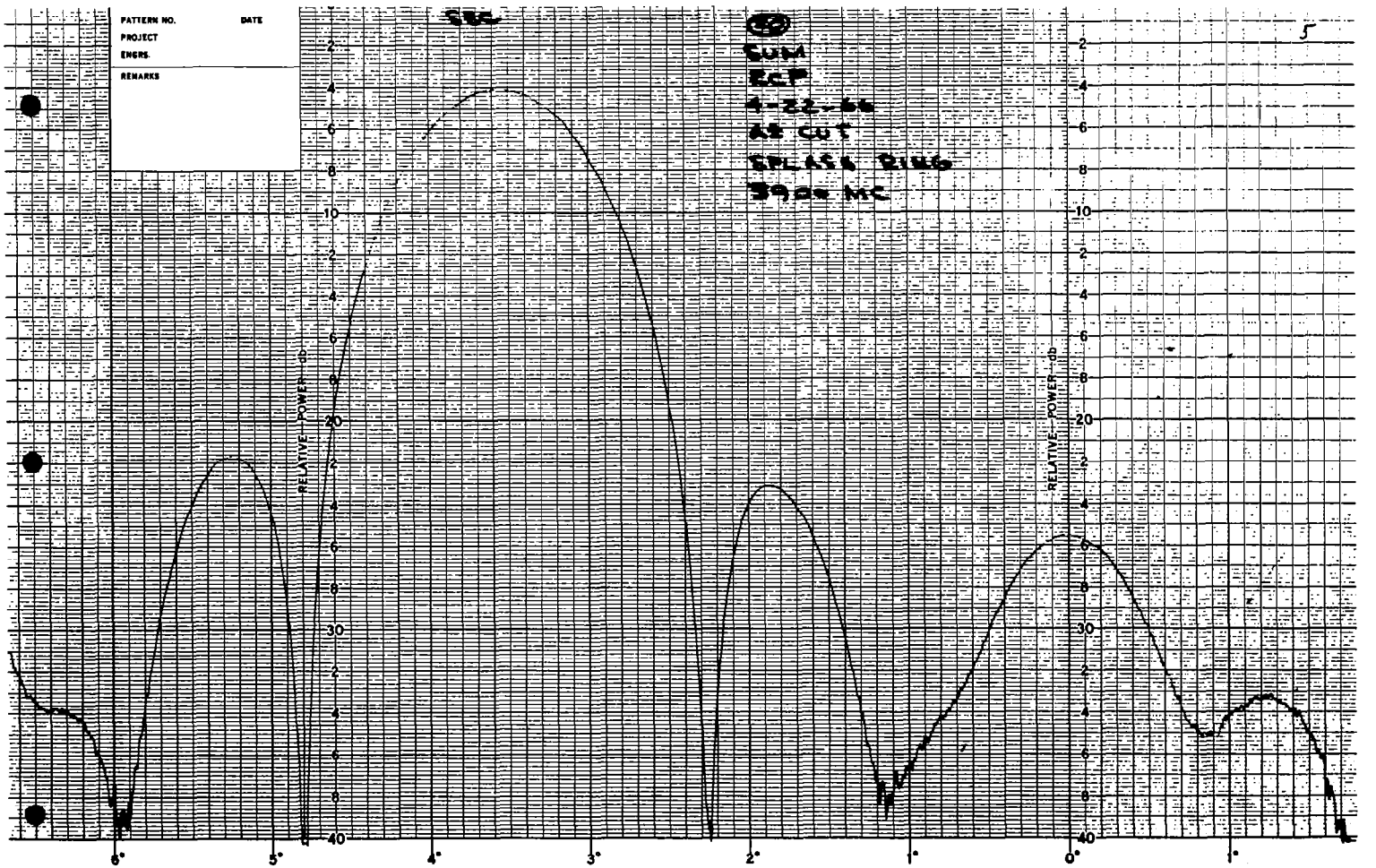


Azimuth Cut – 3900 MC

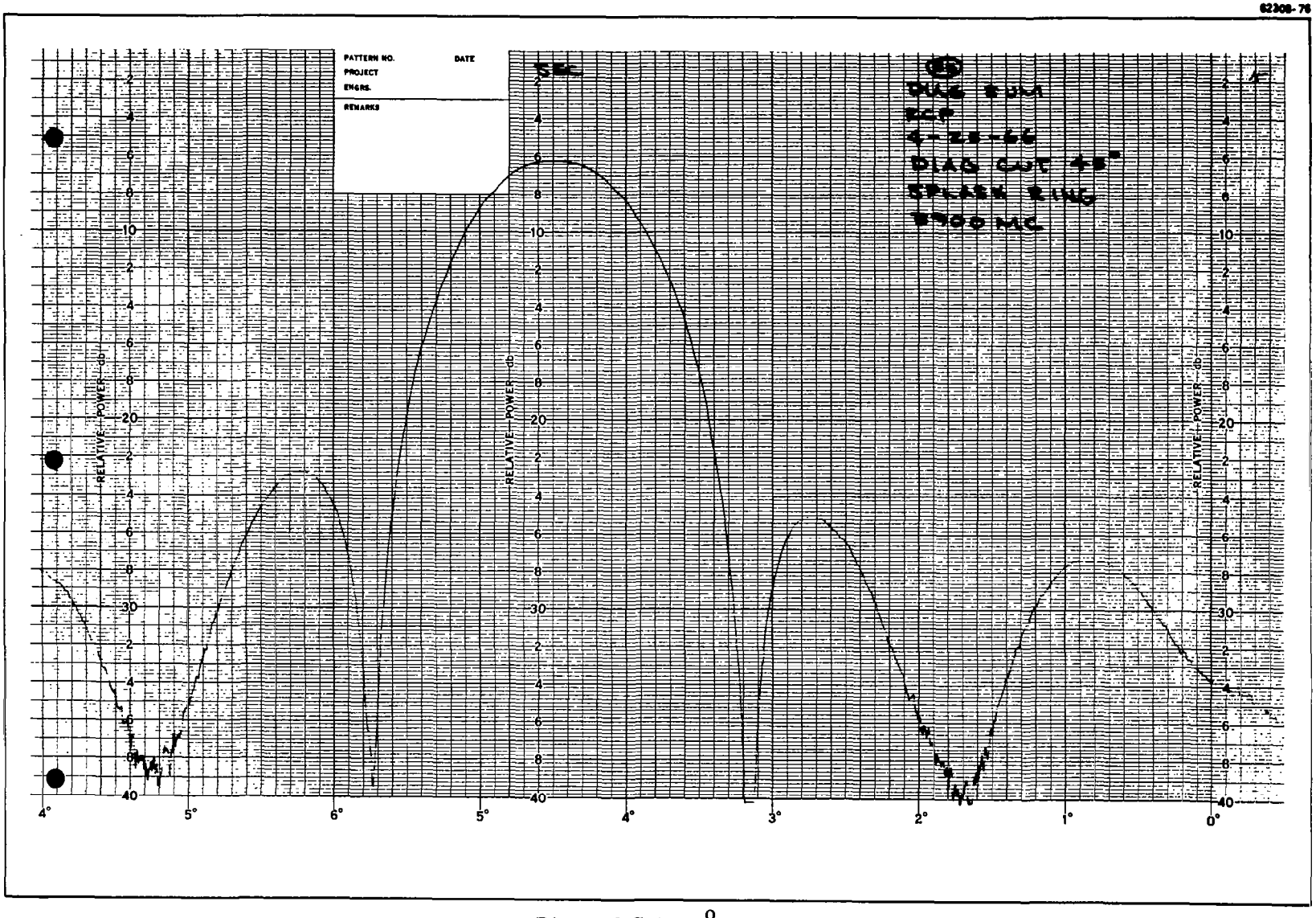


Diagonal Cut $-45^{o}$ – 3900 MC

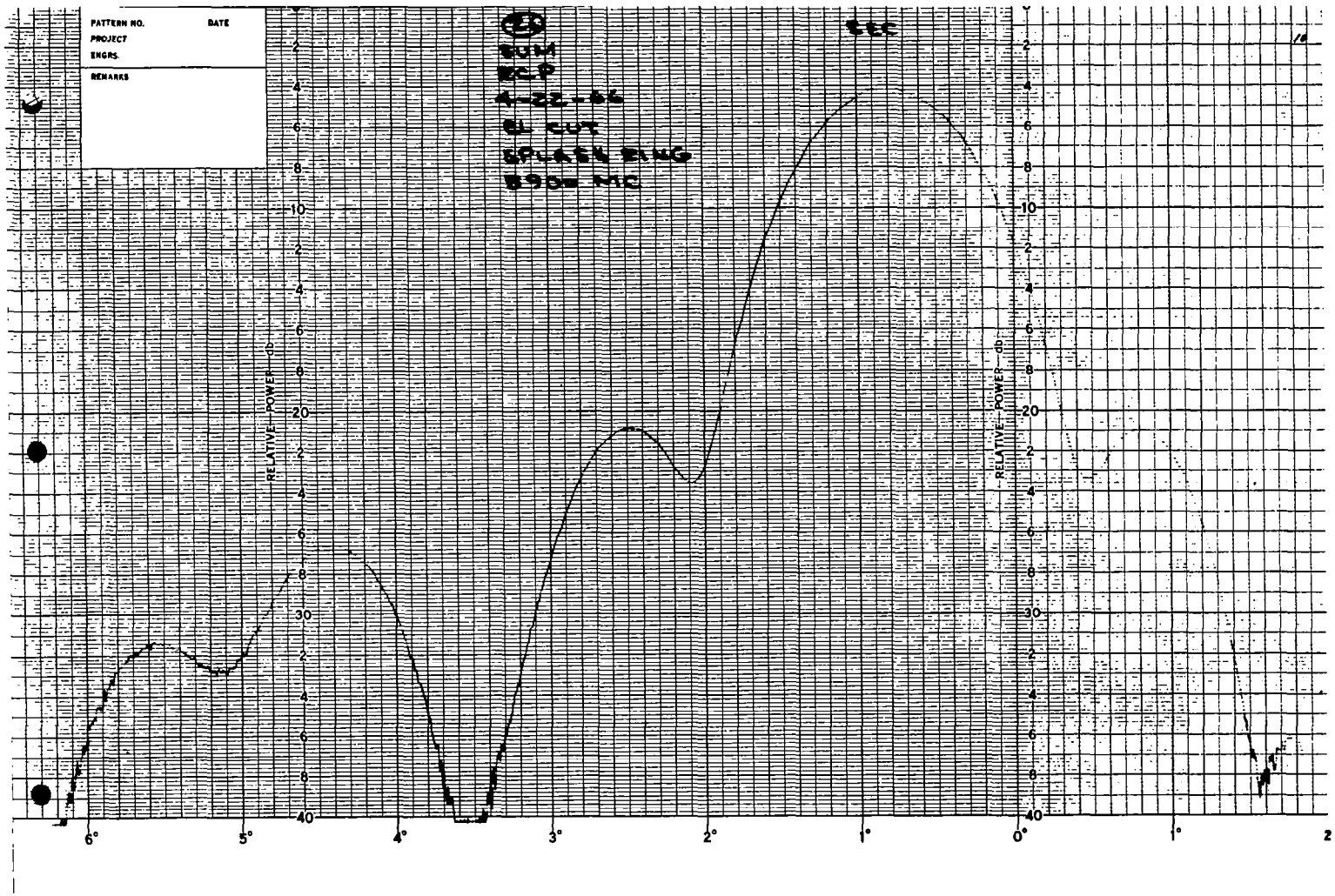


Elevation Cut – 3900 MC

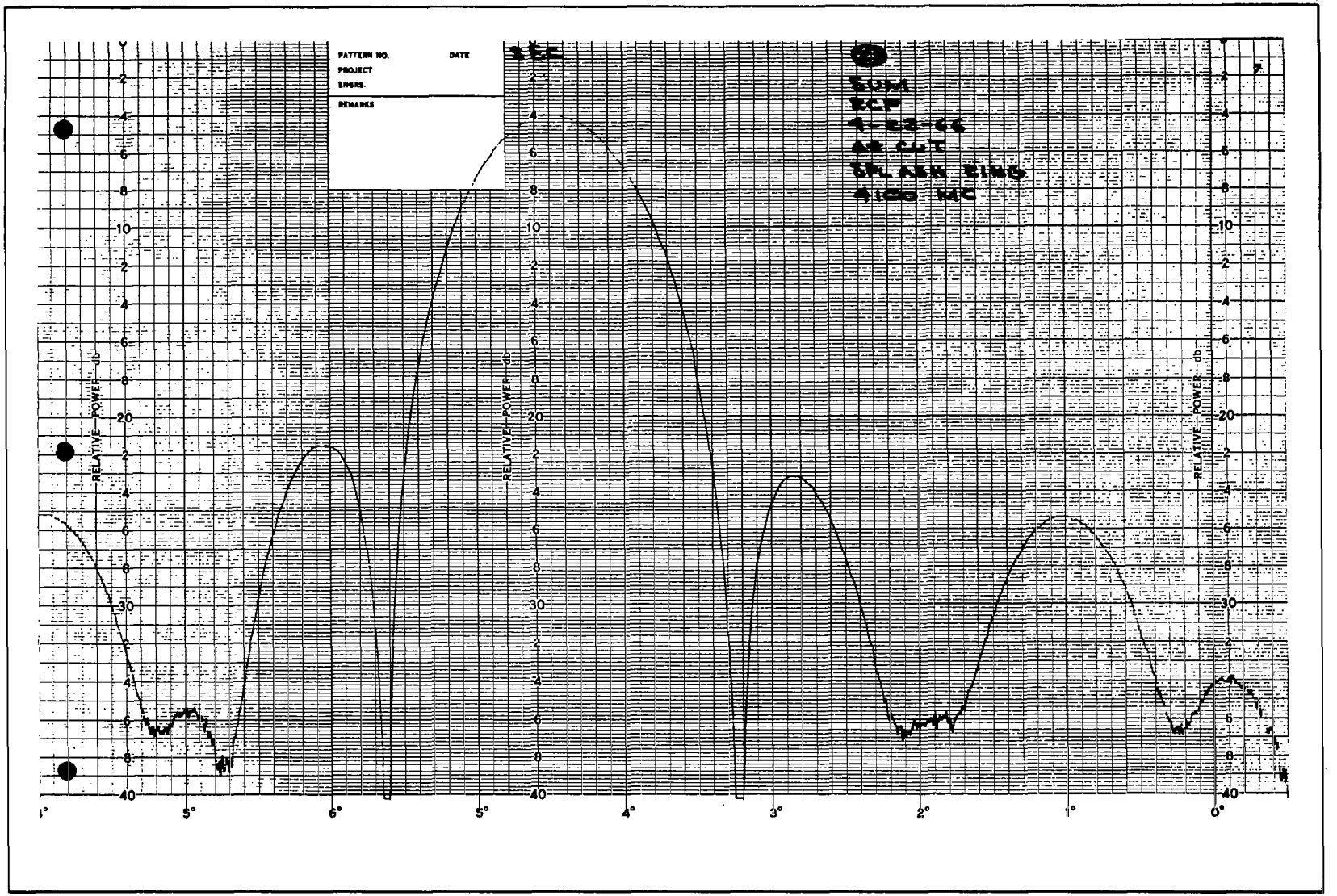


Azimuth Cut – 4100 MC

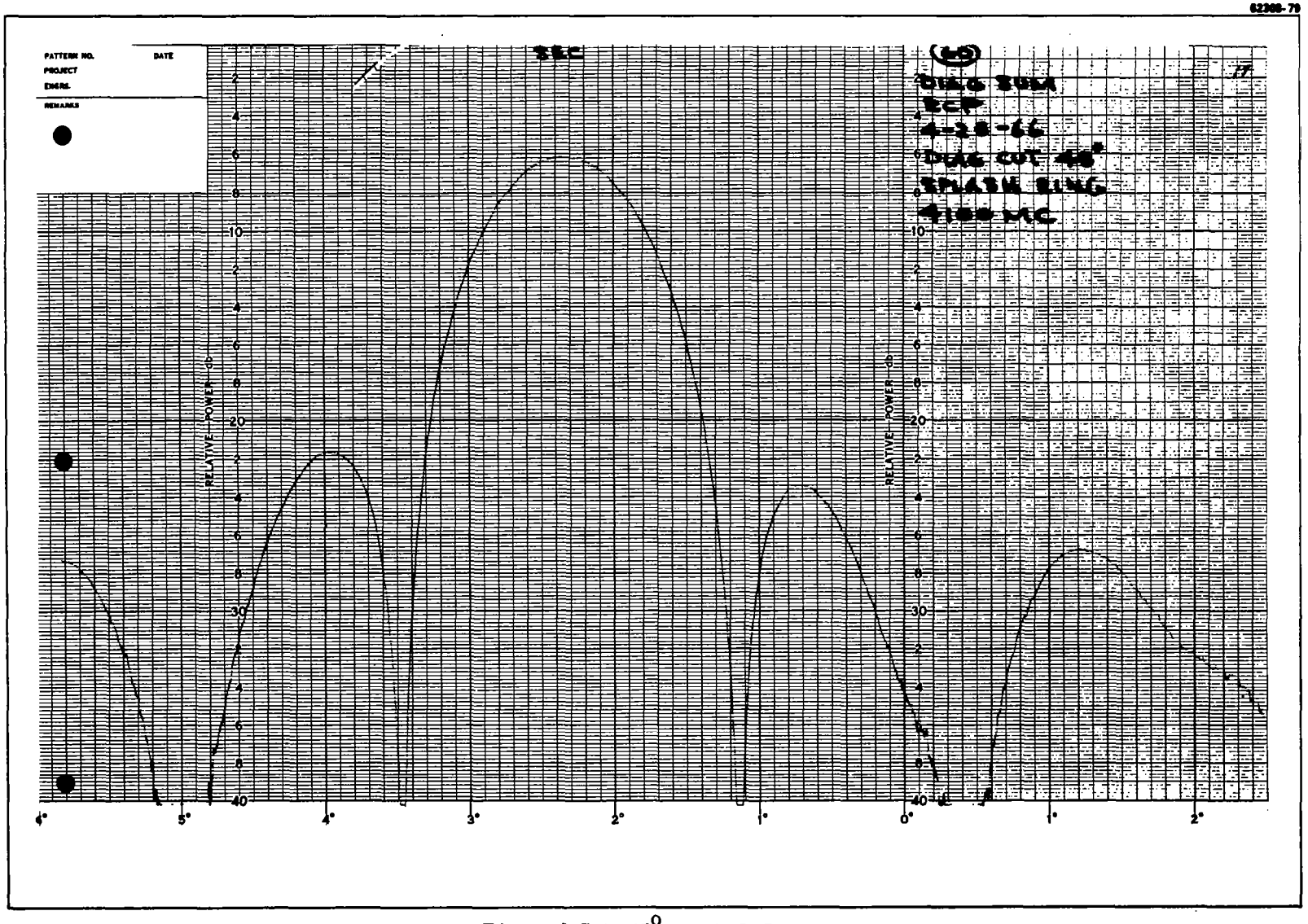


Diagonal Cut -45° – 4100 MC

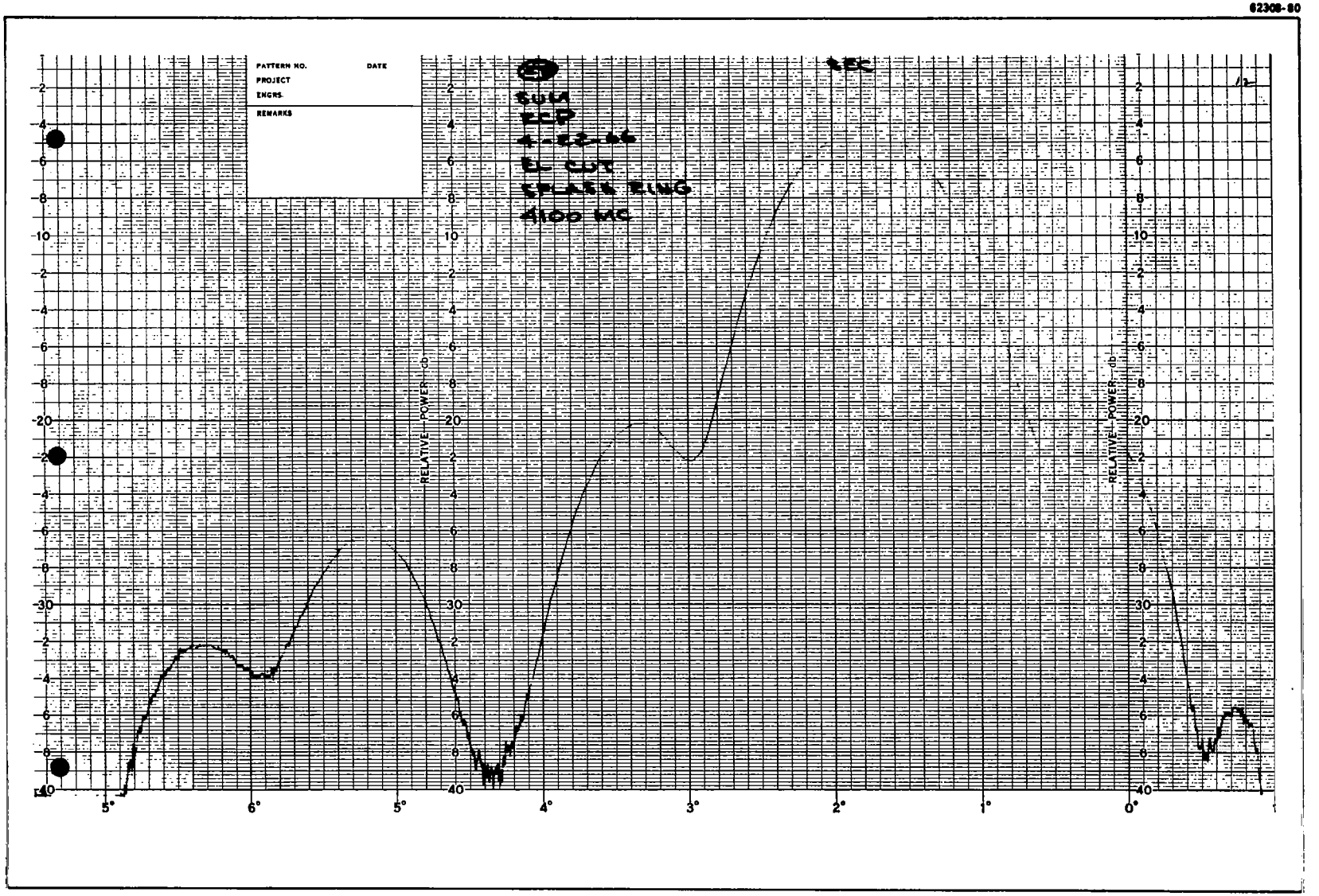


Elevation Cut – 4100 MC

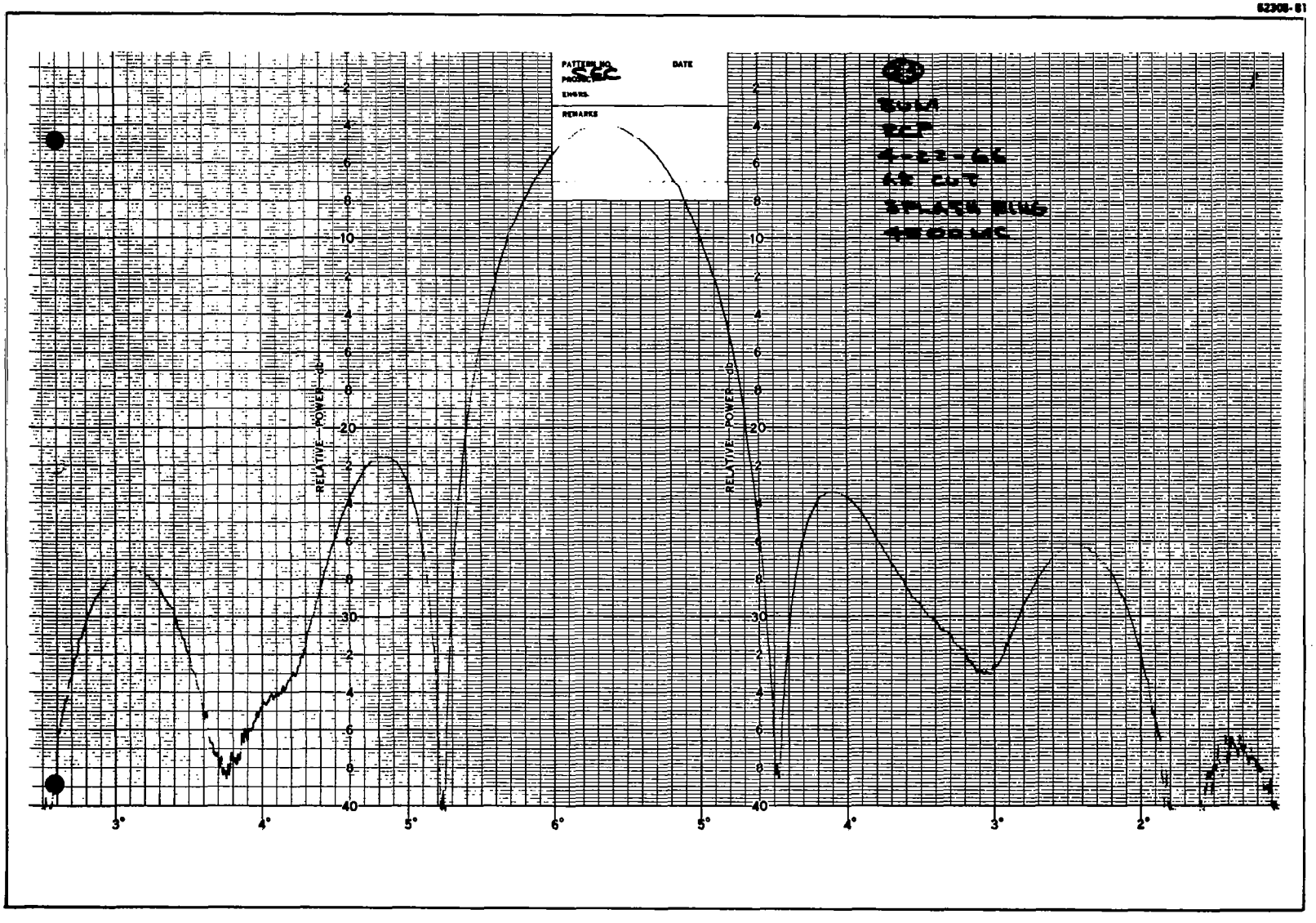


Azimuth Cut – 4300 MC

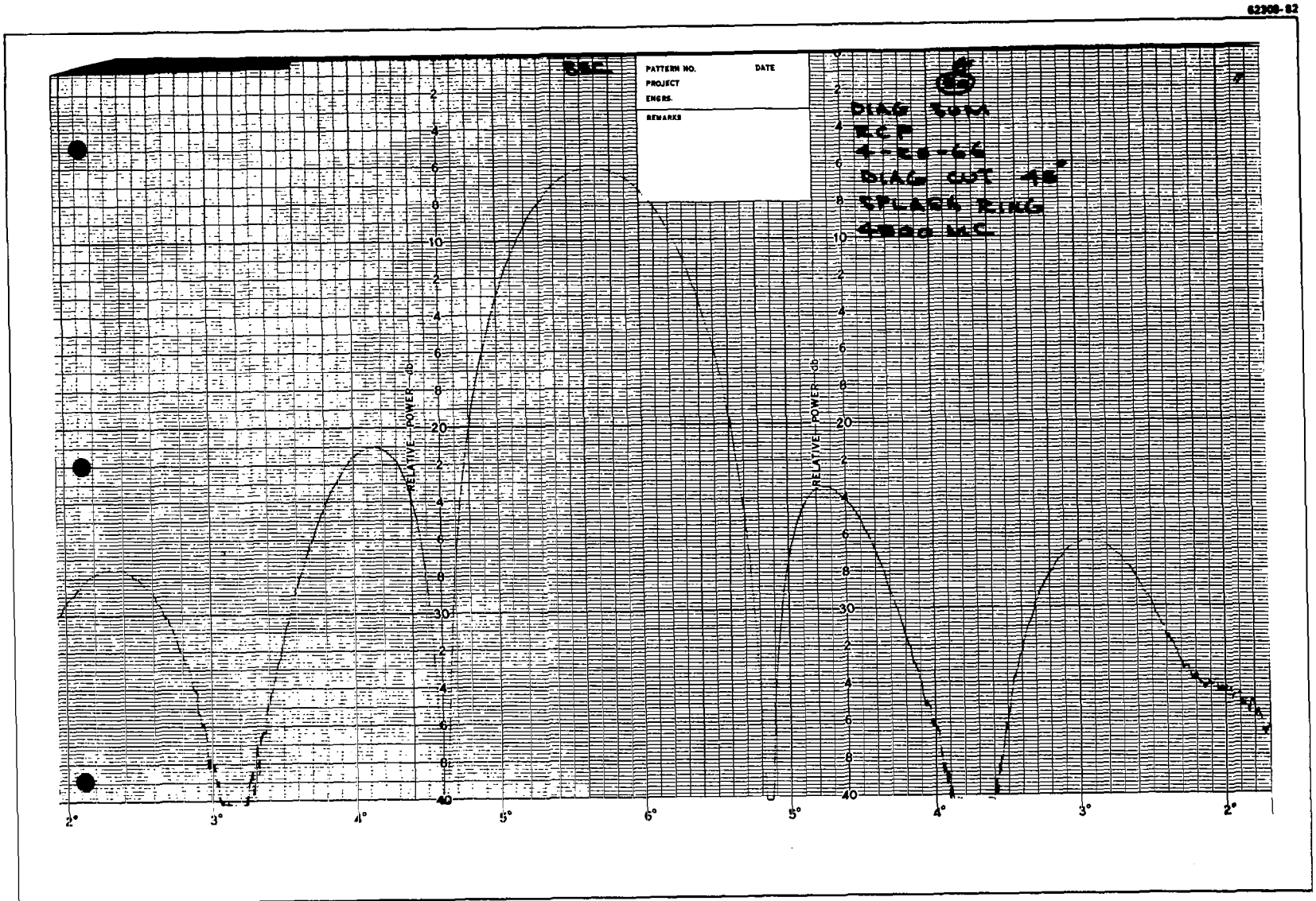


Diagonal Cut $-45^{O}$ – 4300 MC

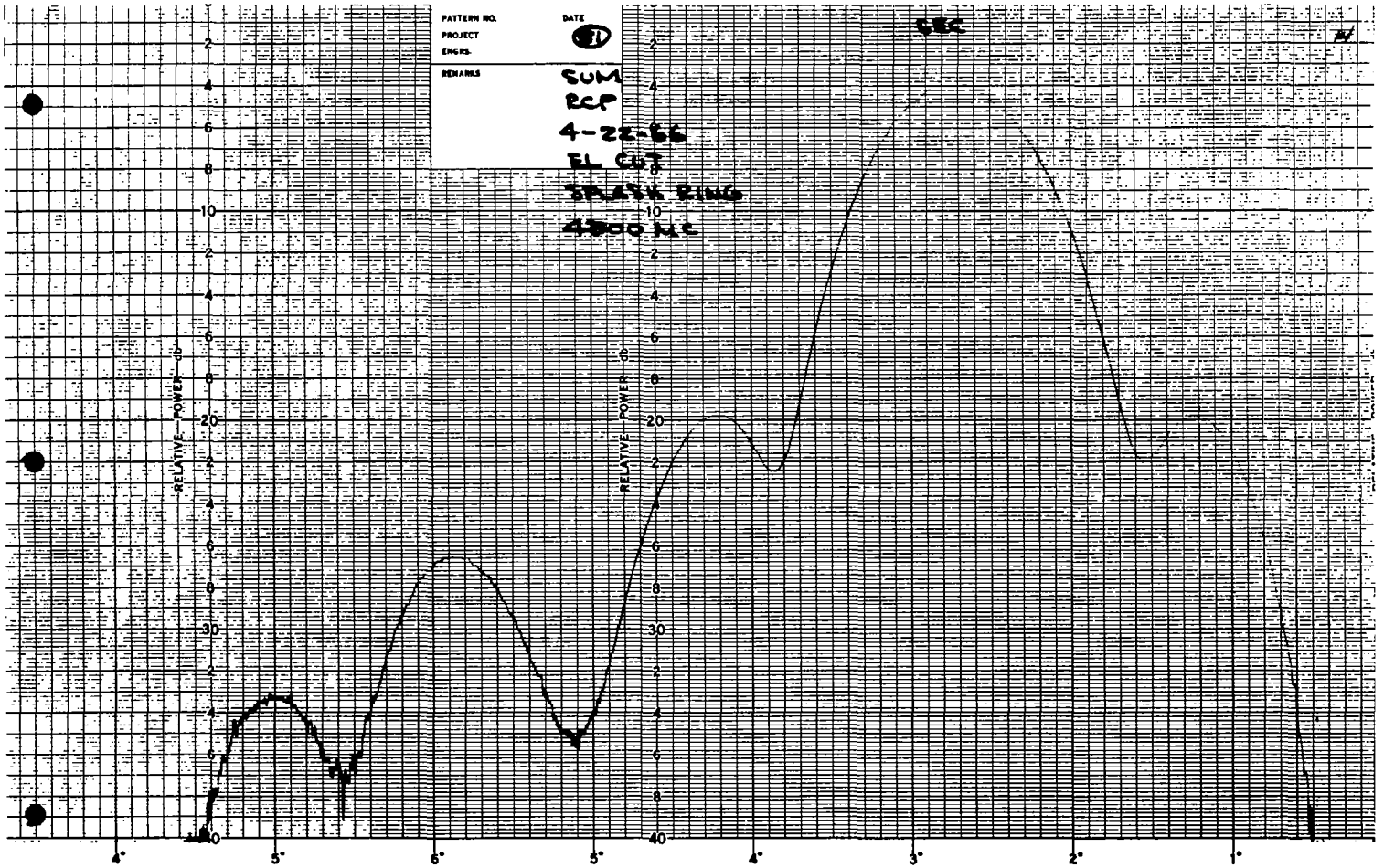


Elevation Cut – 4300 MC

## 8. SECONDARY CROSS POLARIZED RADIATION PATTERNS (WITH SPLASH PLATE)

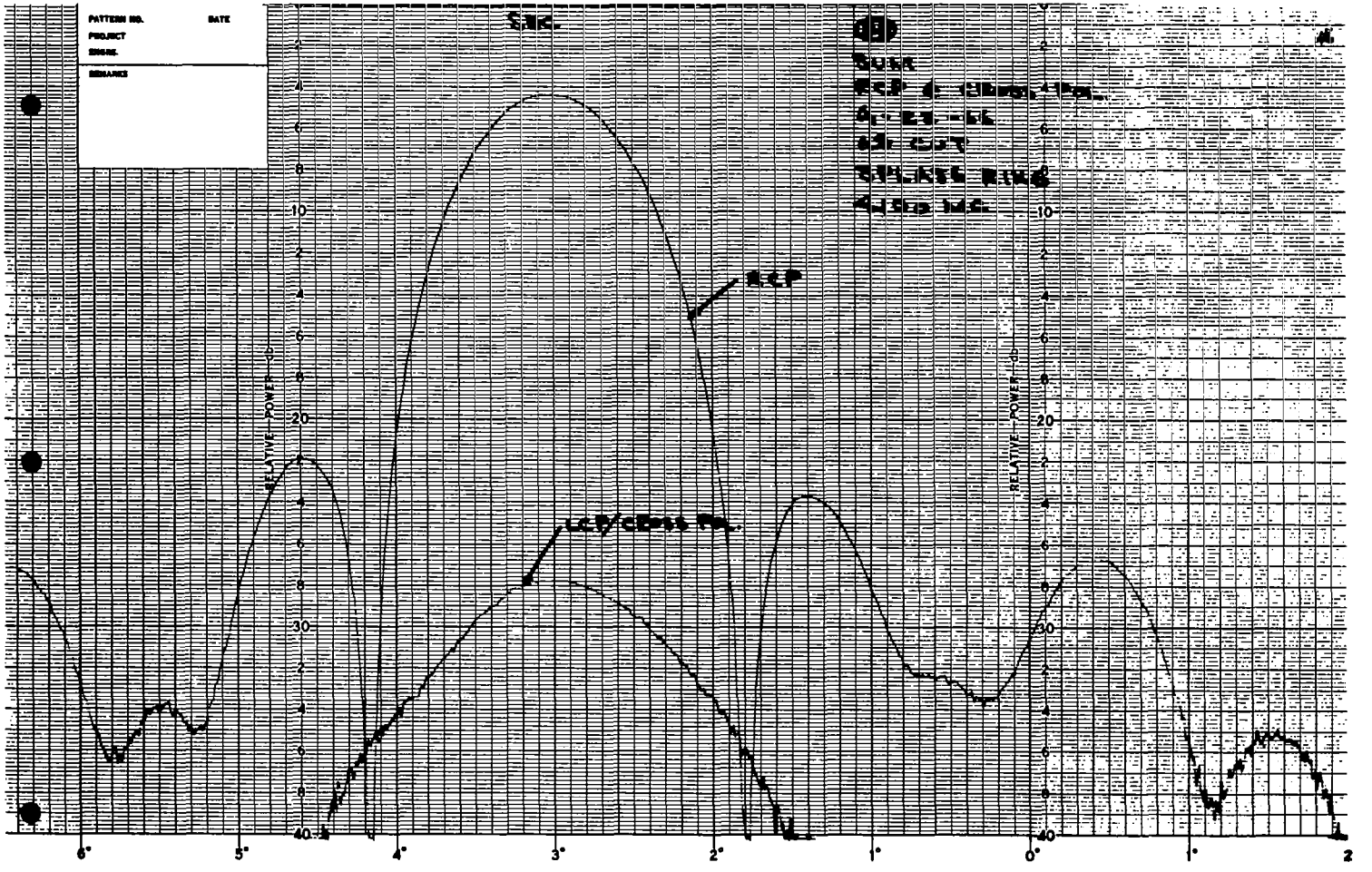


Sum – RCP & Cross Polarization – Azimuth Cut – 4100 MC

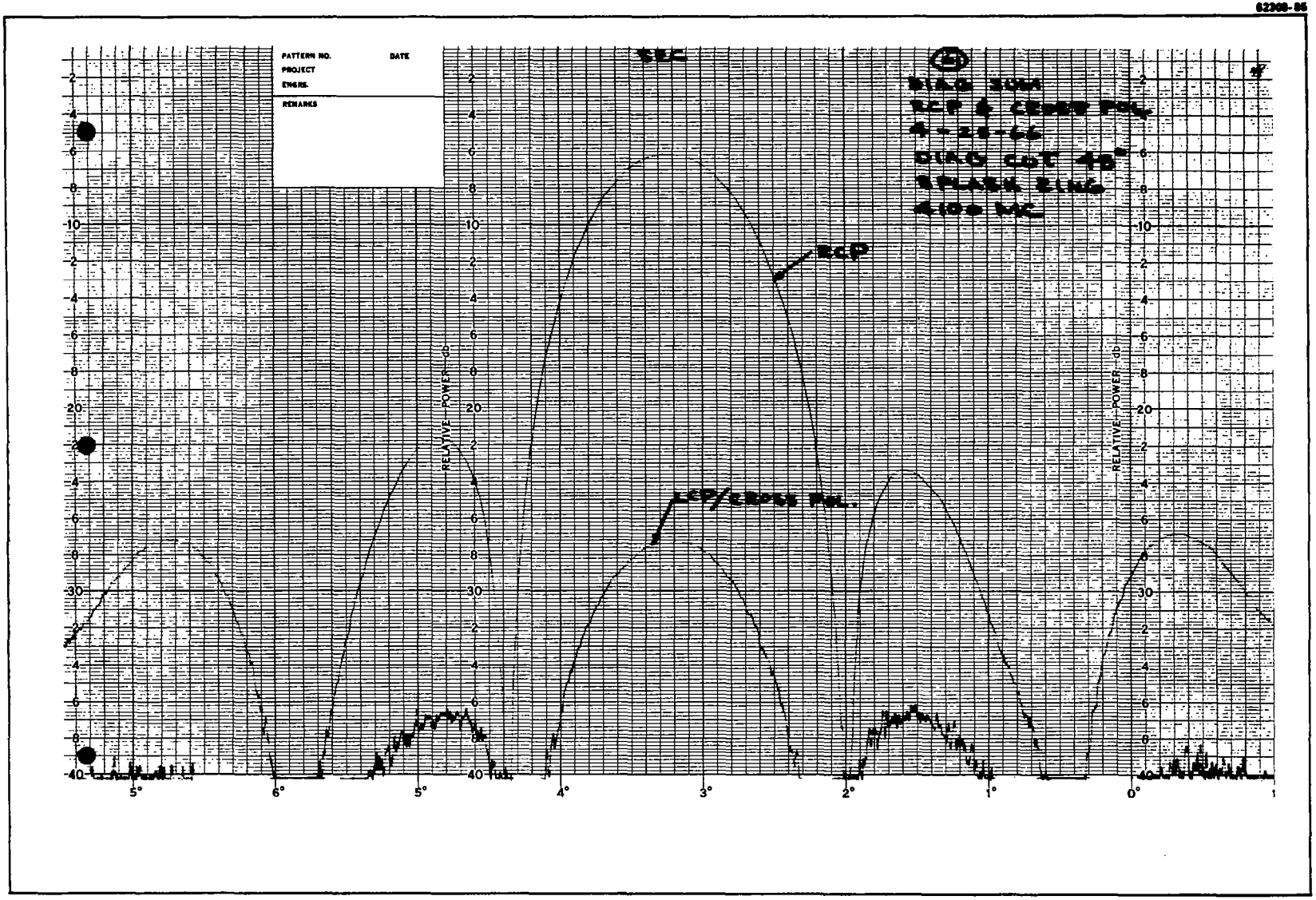


Sum – RCP & Cross Polarization – Diagonal Cut +45° – 4100 MC

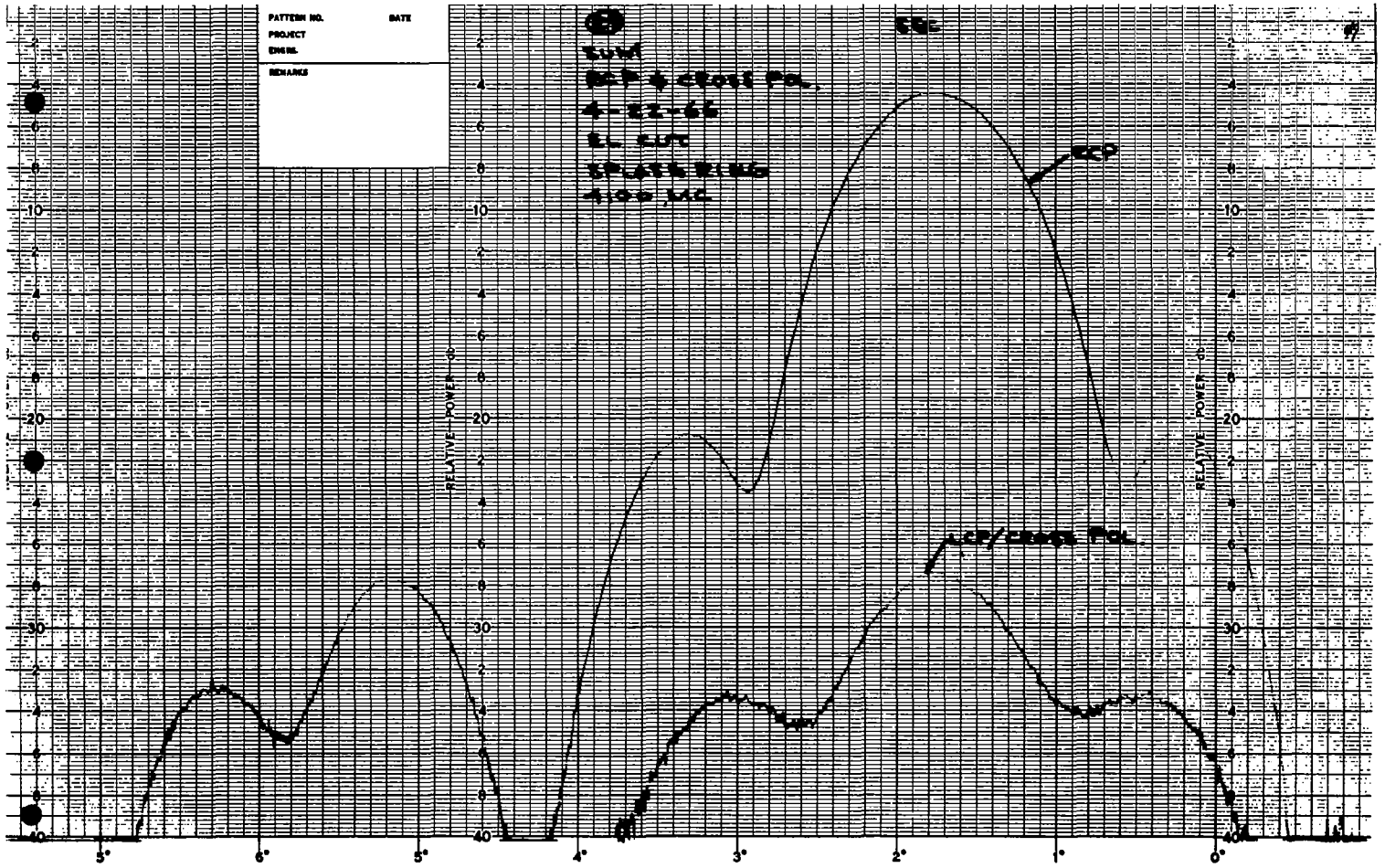


Sum – RCP & Cross Polarization – Elevation Cut – 4100 MC

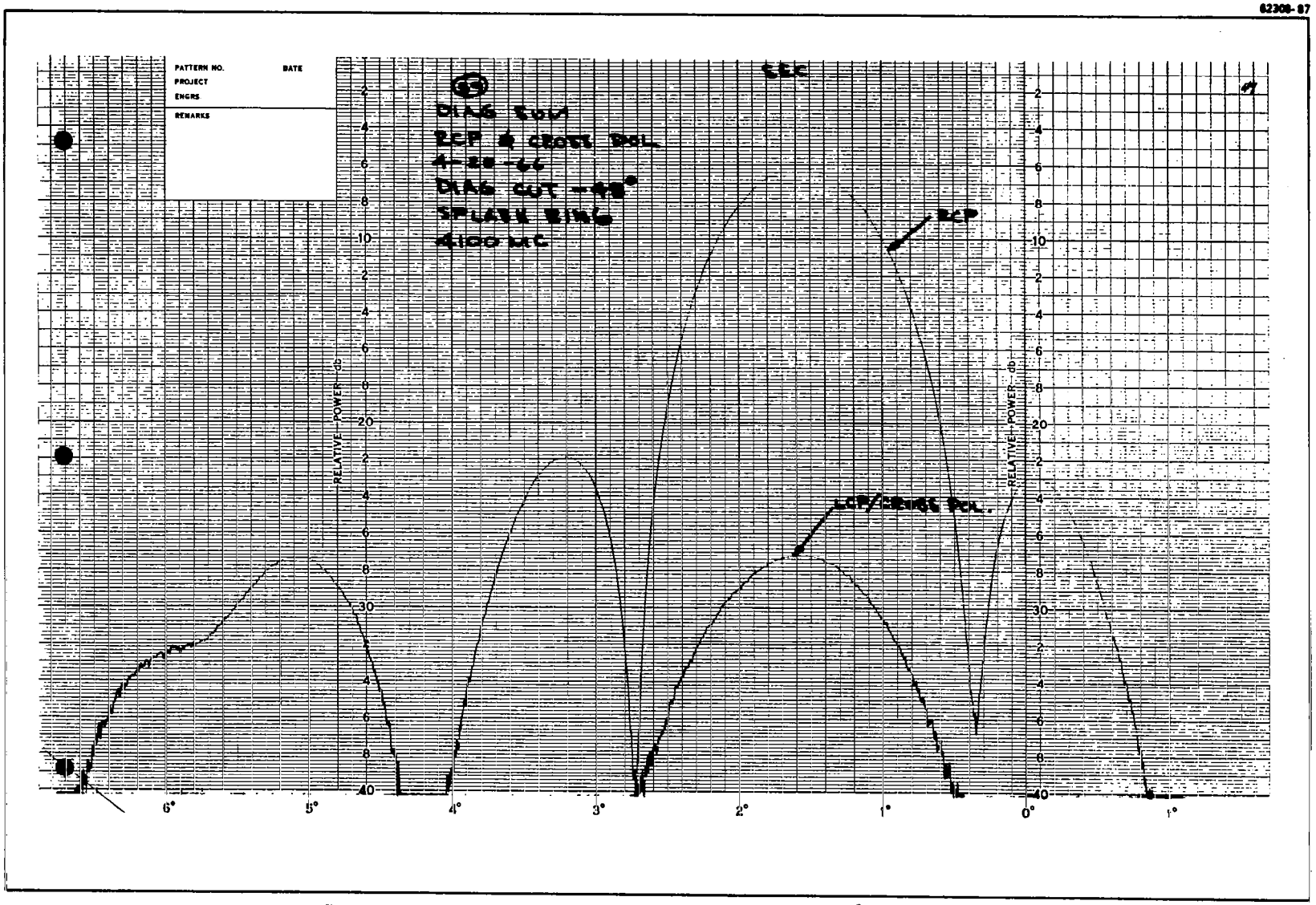


Sum – RCP & Cross Polarization – Diagonal Cut -45° – 4100 MC

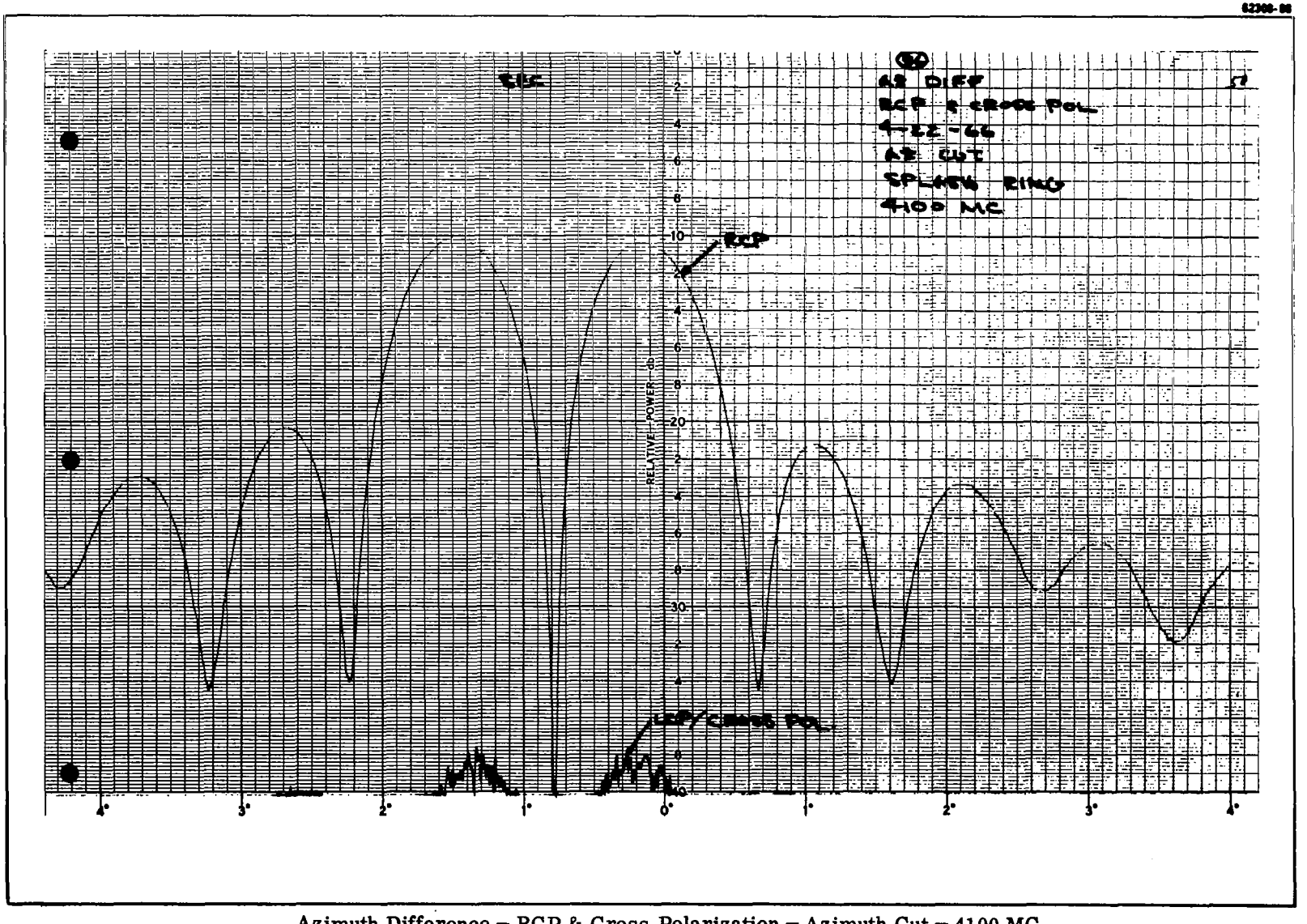


Azimuth Difference – RCP & Cross Polarization – Azimuth Cut – 4100 MC

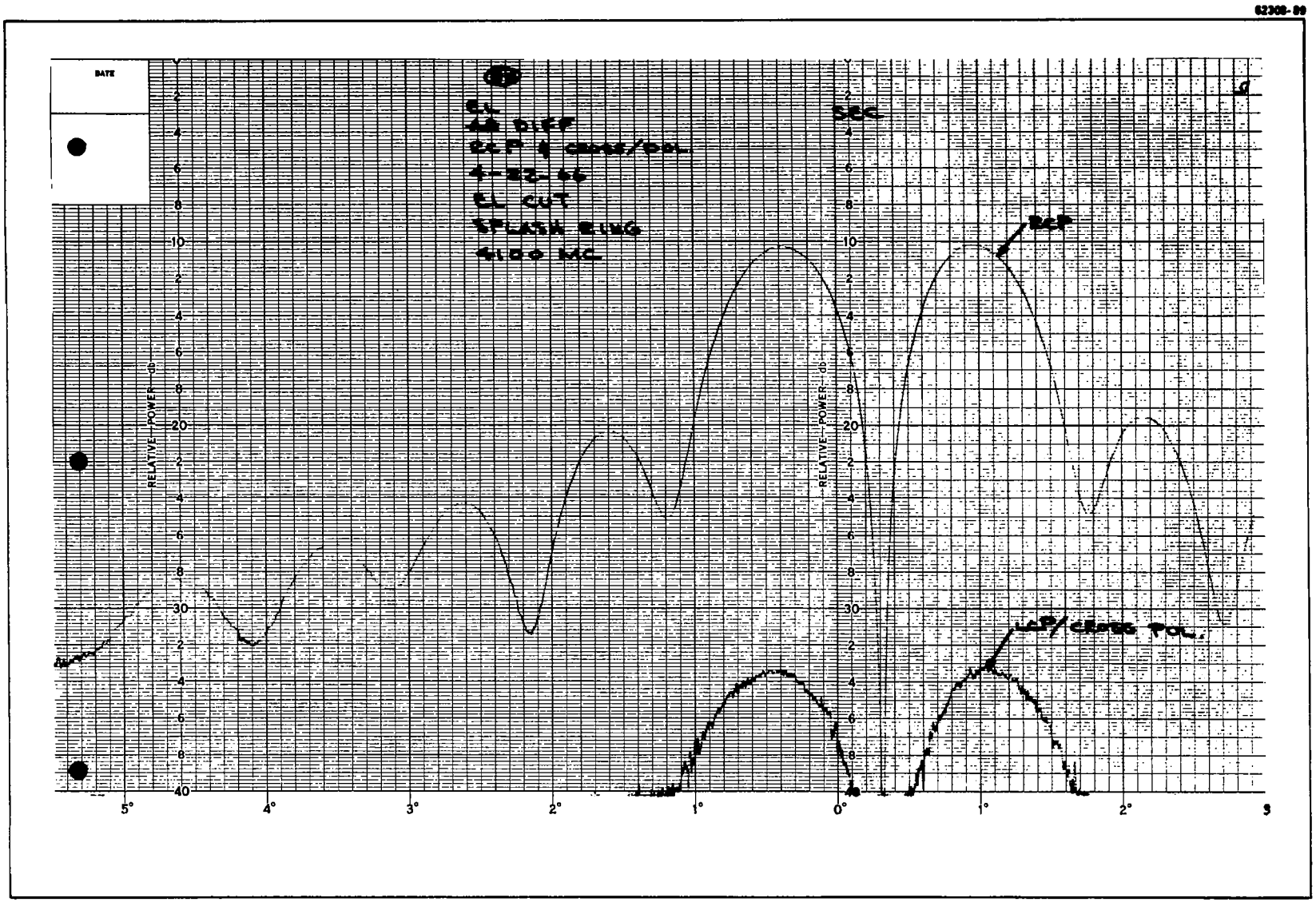


Elevation Difference – RCP & Cross Polarization – Elevation Cut – 4100 MC

# 9. SECONDARY AZIMUTH ERROR RCP RADIATION PATTERNS (WITH SPLASH PLATE)

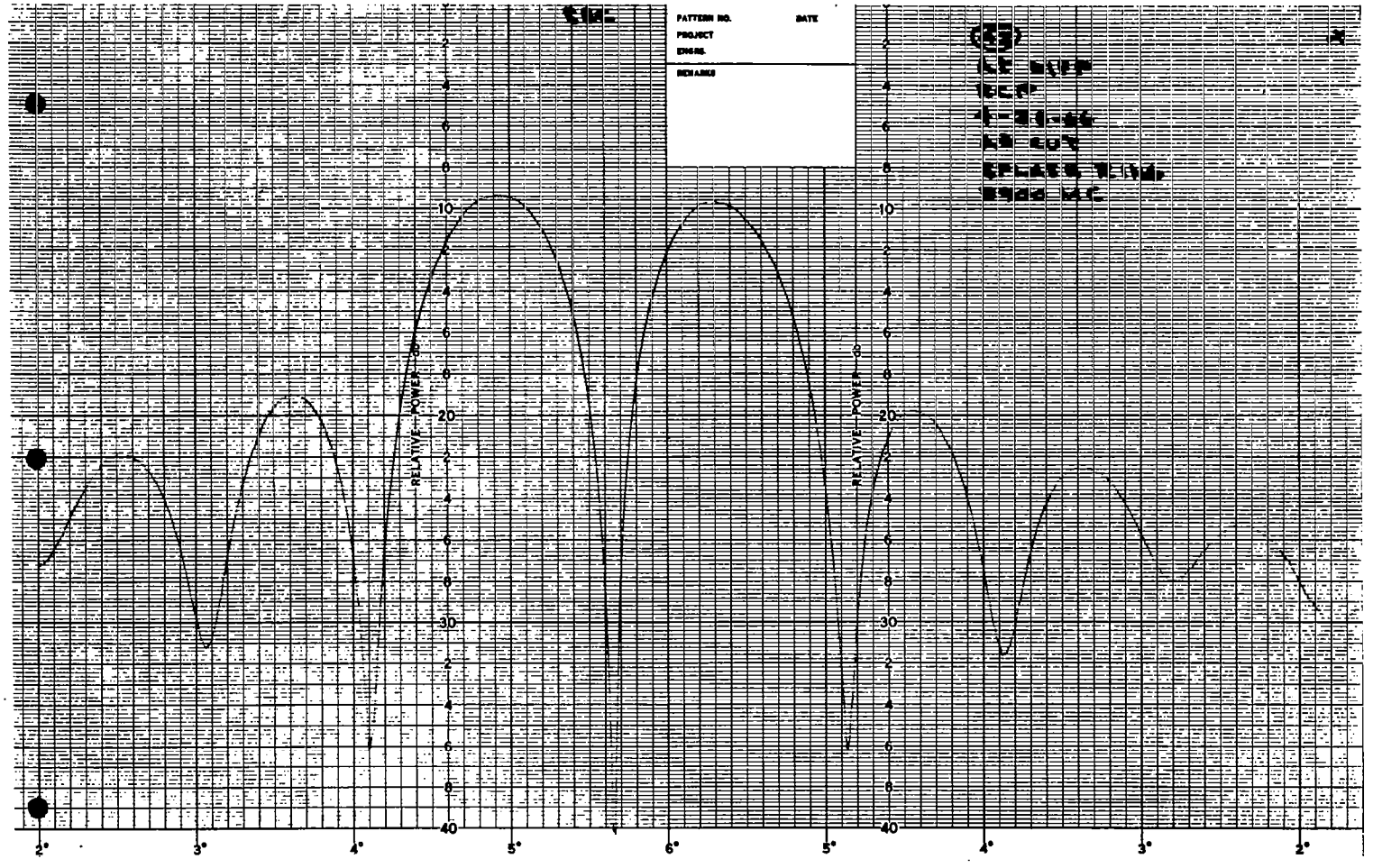


Azimuth Difference – Azimuth Cut – 3900 MC

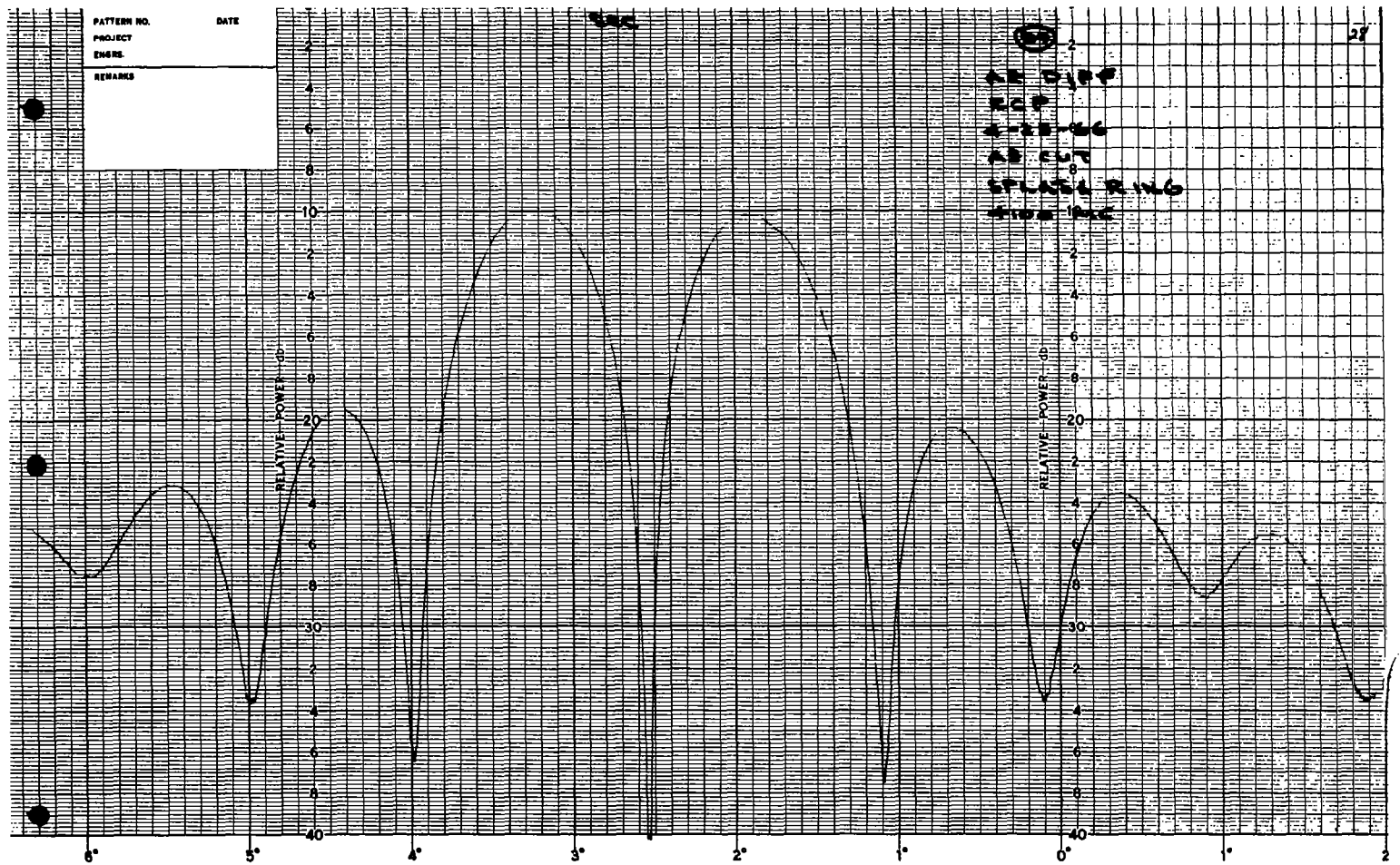


Azimuth Difference – Azimuth Cut – 4100 MC

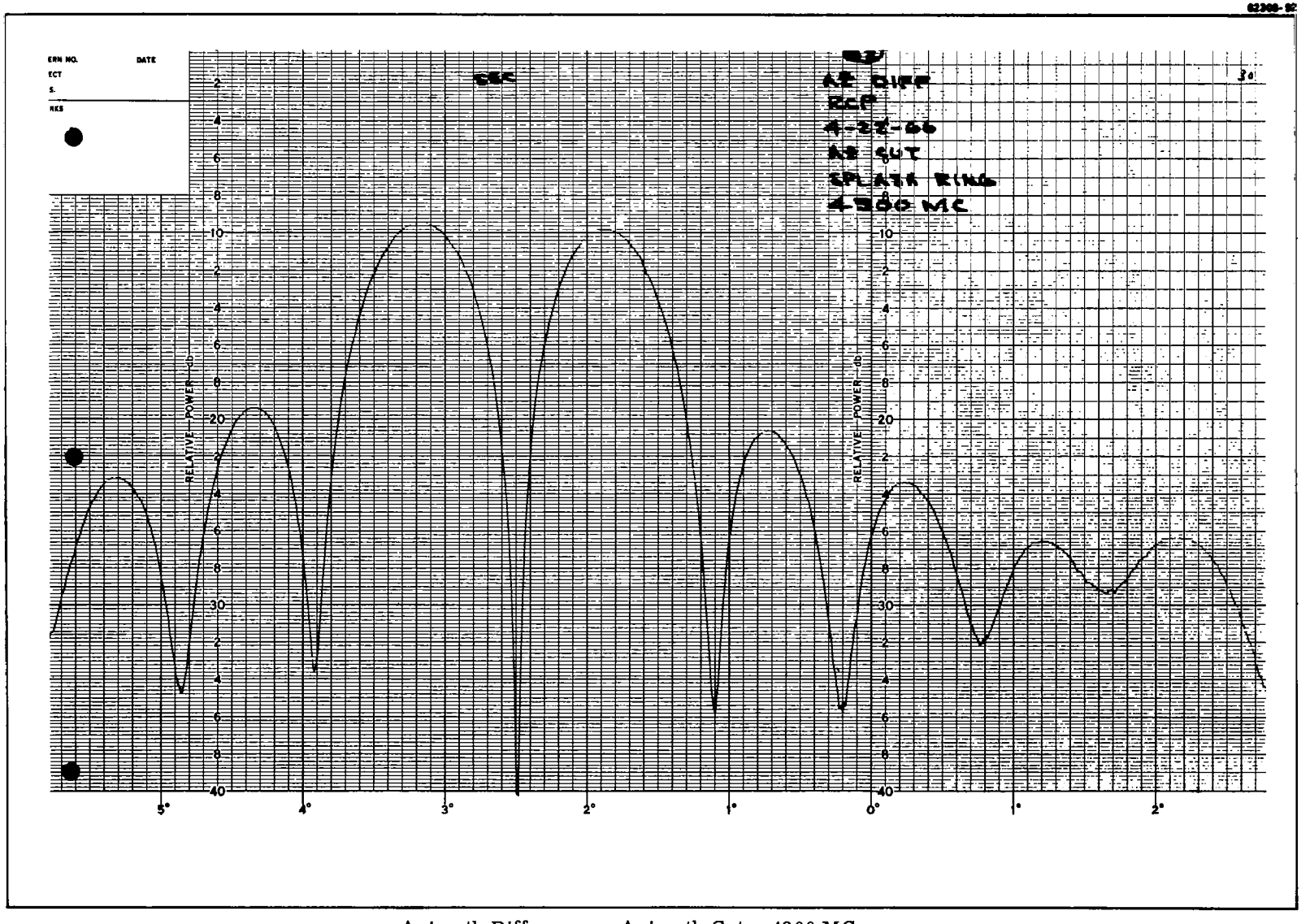


Azimuth Difference – Azimuth Cut – 4300 MC

# 10. SECONDARY ELEVATION ERROR RCP RADIATION PATTERNS (WITH SPLASH PLATE)

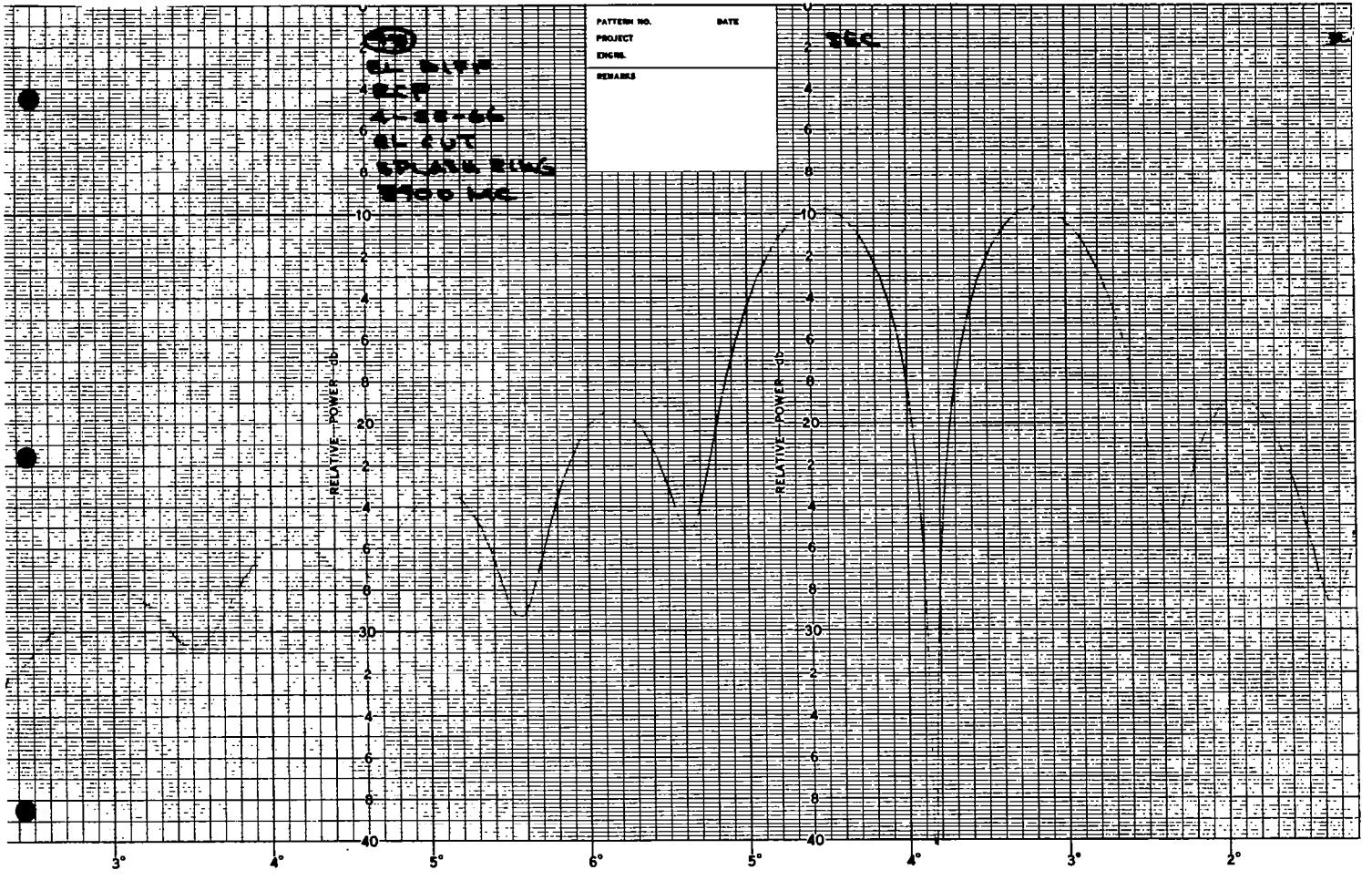


Elevation Difference – Elevation Cut –3900 MC

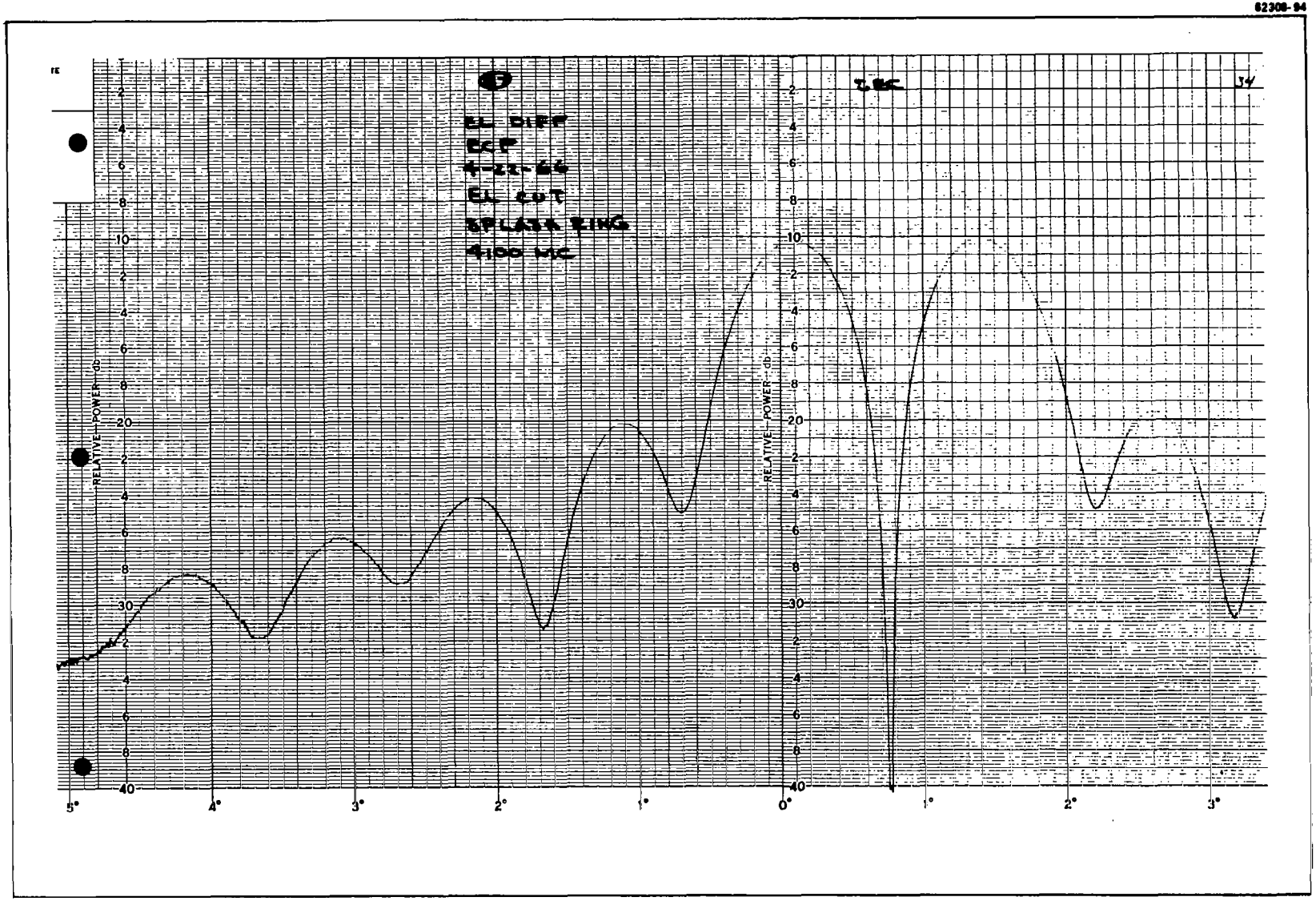


Elevation Difference – Elevation Cut – 4100 MC

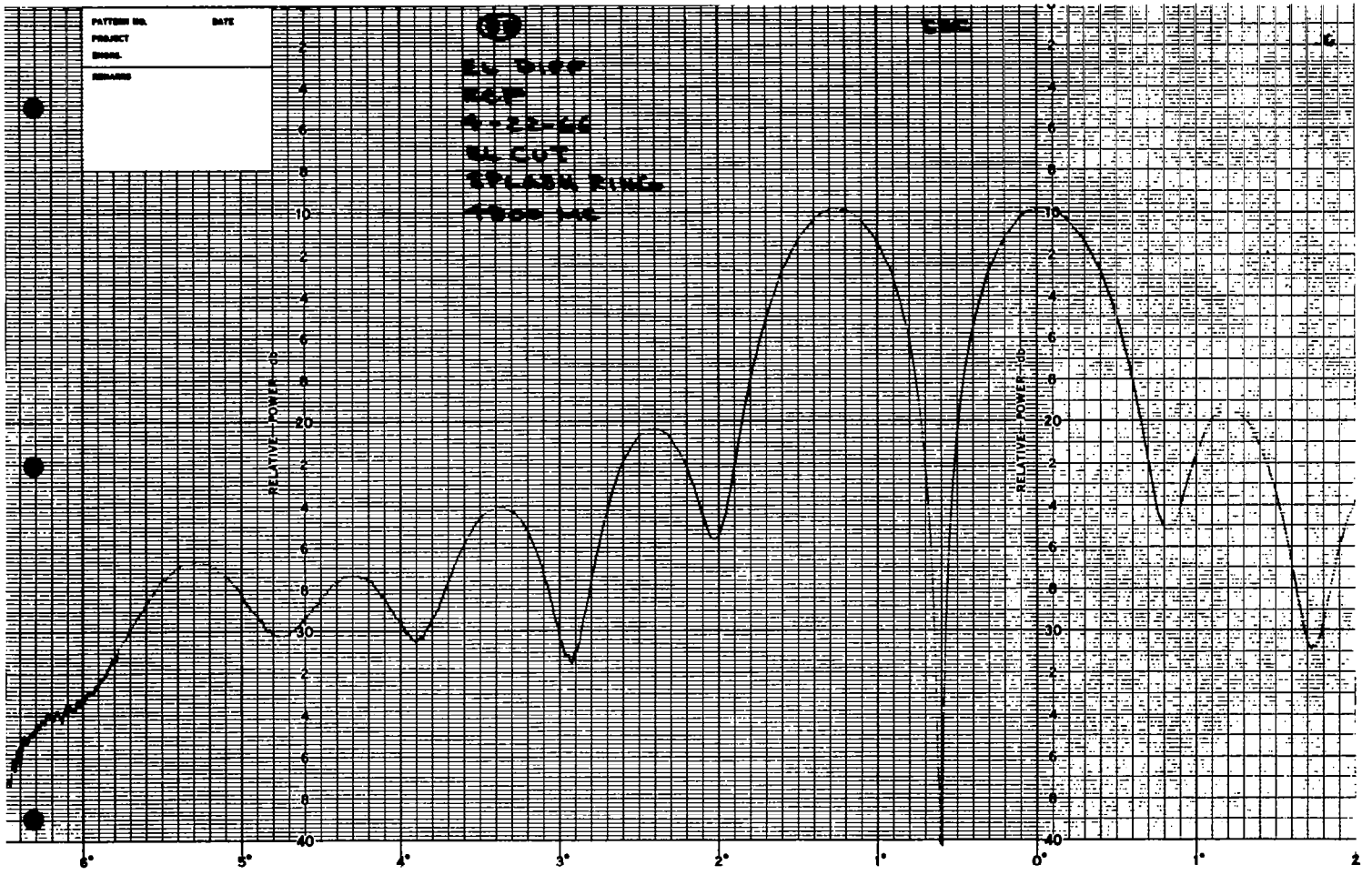


Elevation Difference – Elevation Cut – 4300 MC

# 11. SECONDARY LINEAR POLARIZED RADIATION PATTERNS (WITH SPLASH PLATE)

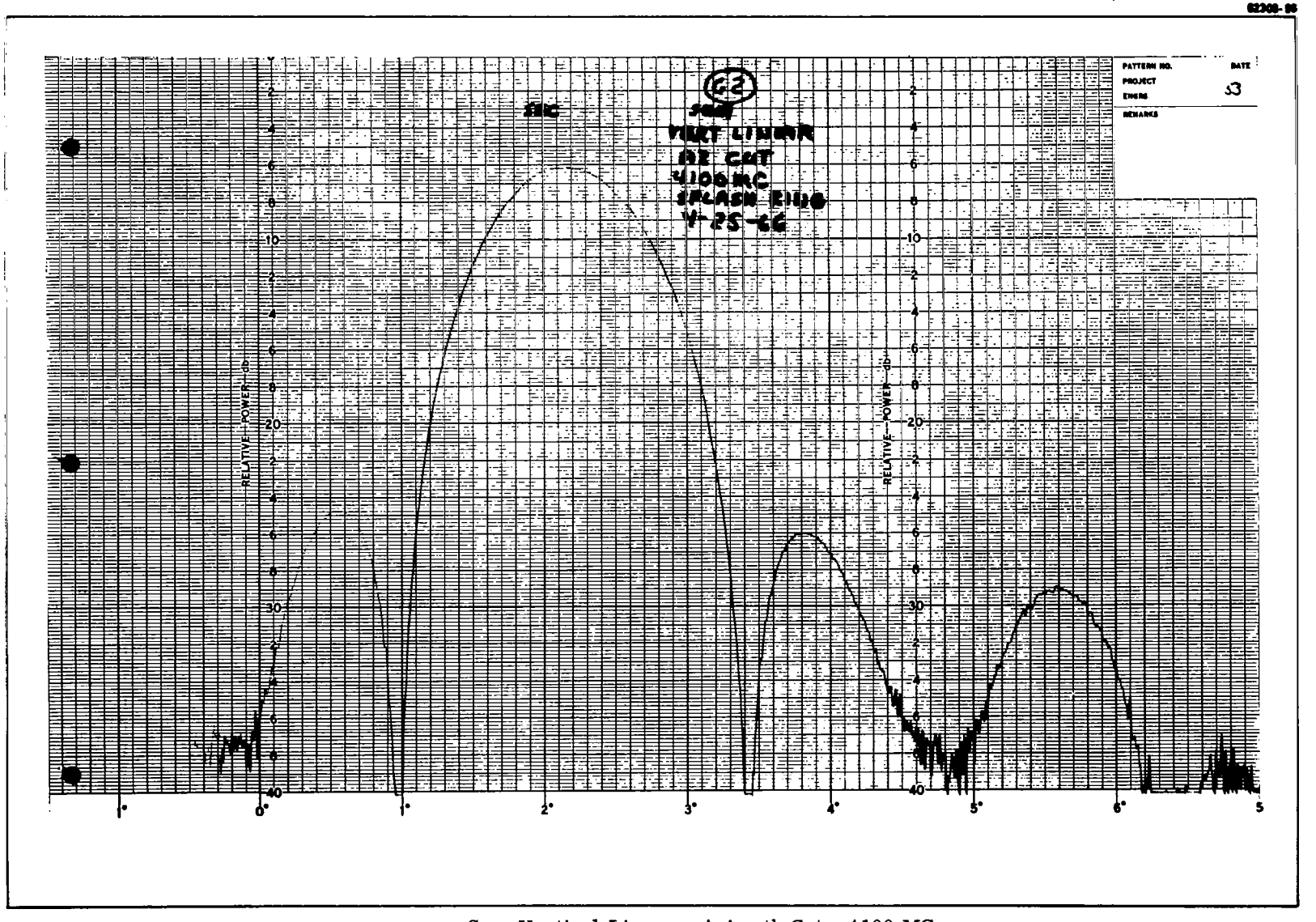


Sum-Vertical Linear – Azimuth Cut – 4100 MC

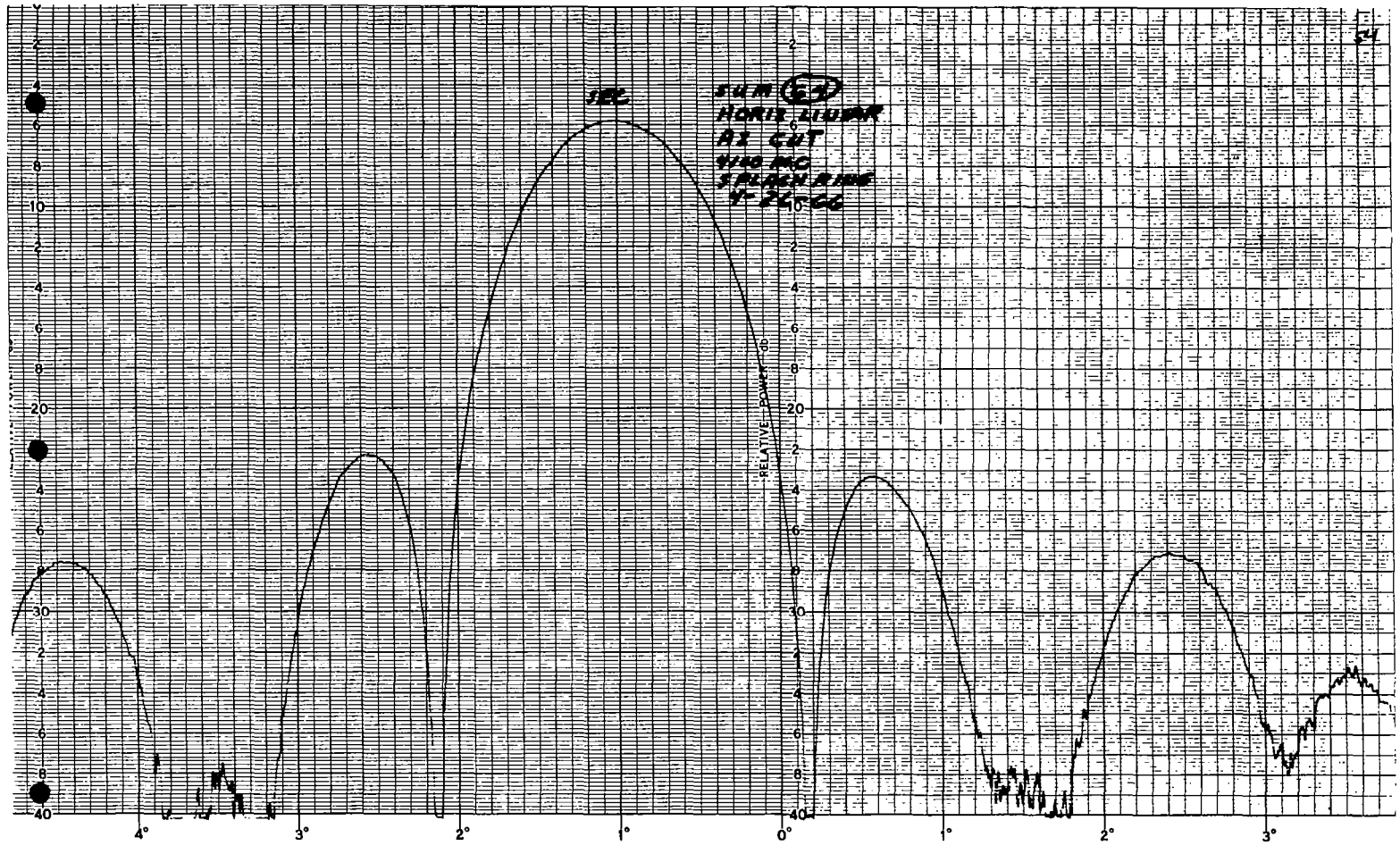


Sum – Horizontal Linear – Azimuth Cut – 4100 MC

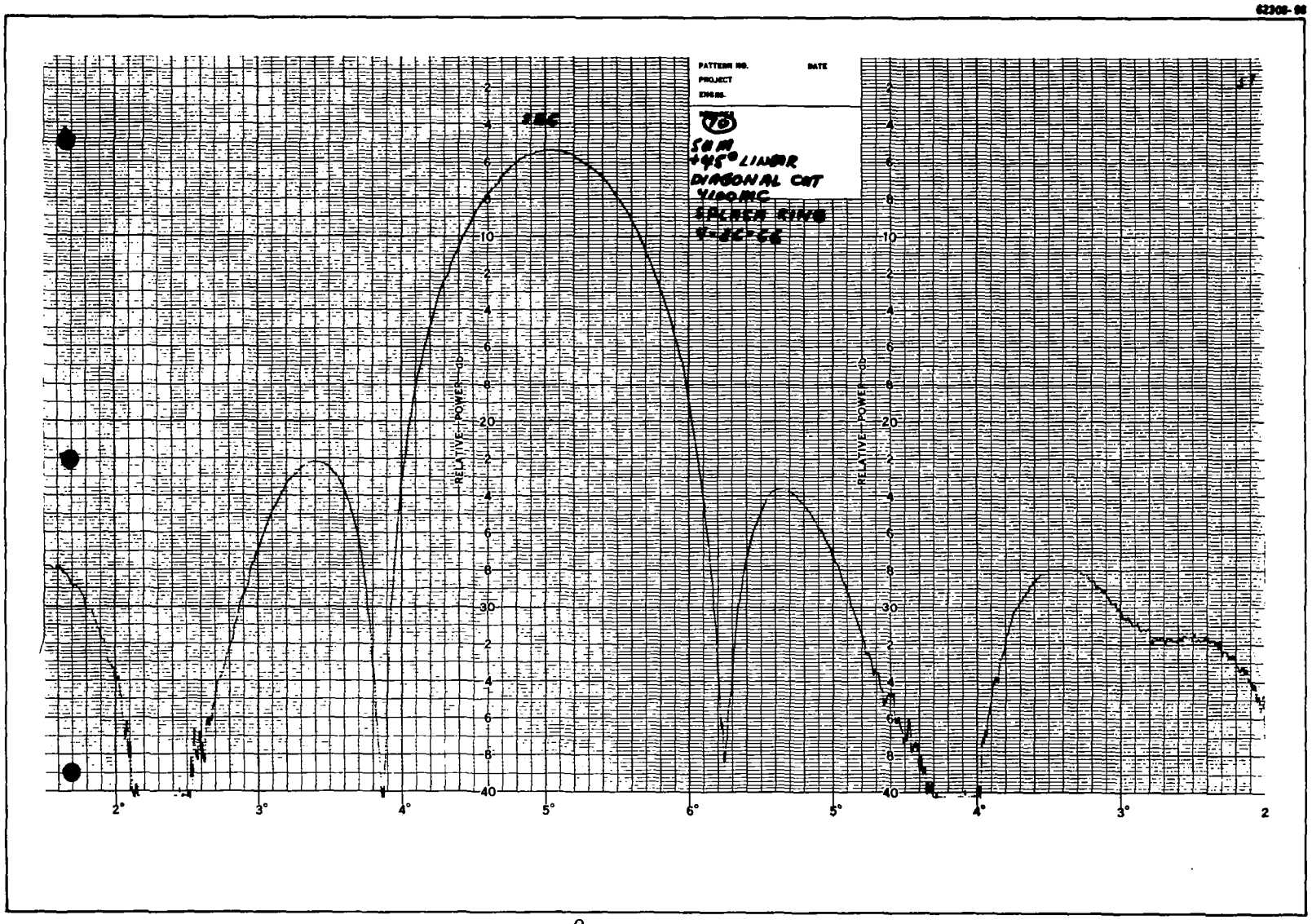


Sum – +45° Linear – Diagonal Cut – 4100 MC

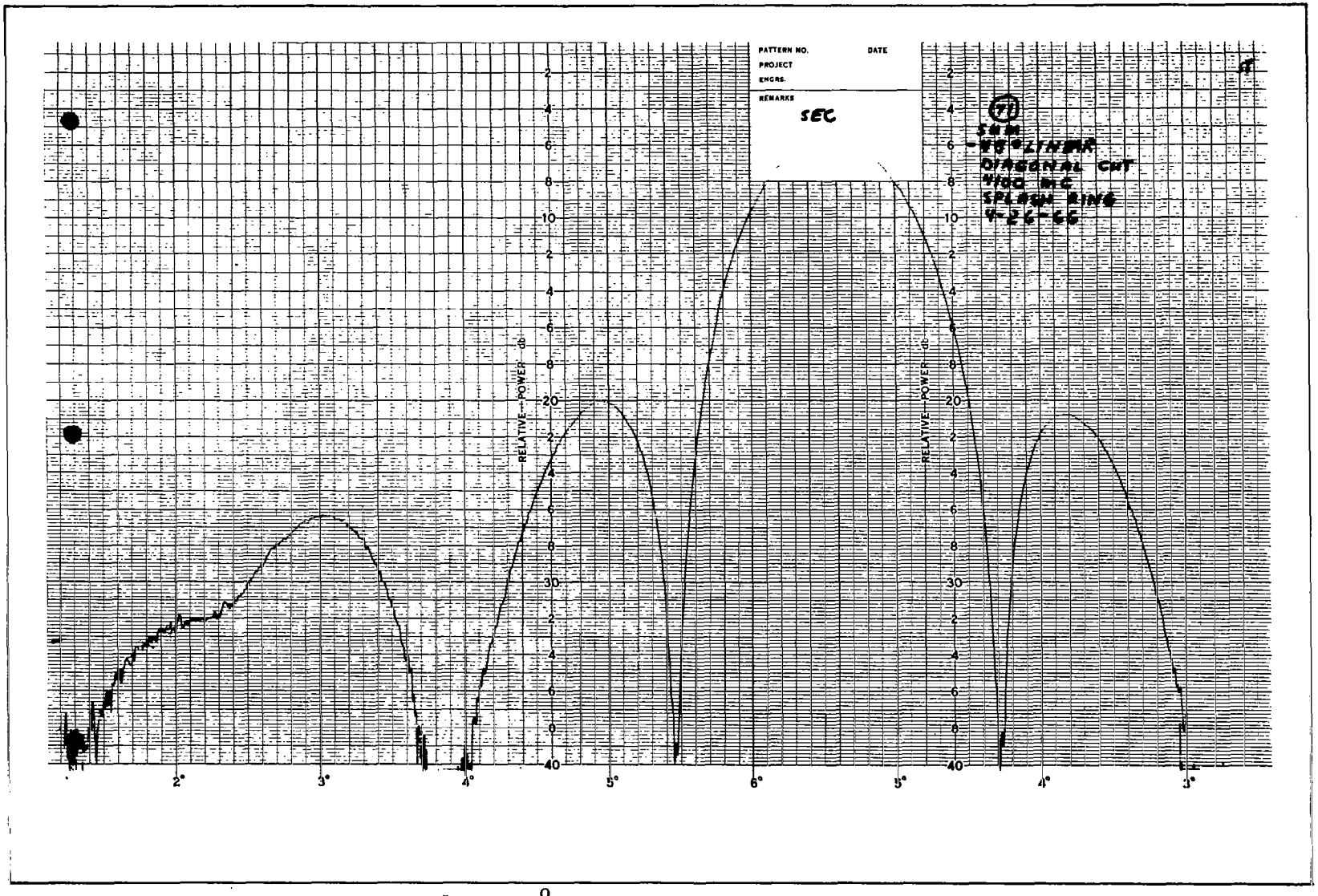


Sum – -45° Linear – Diagonal Cut – 4100 MC

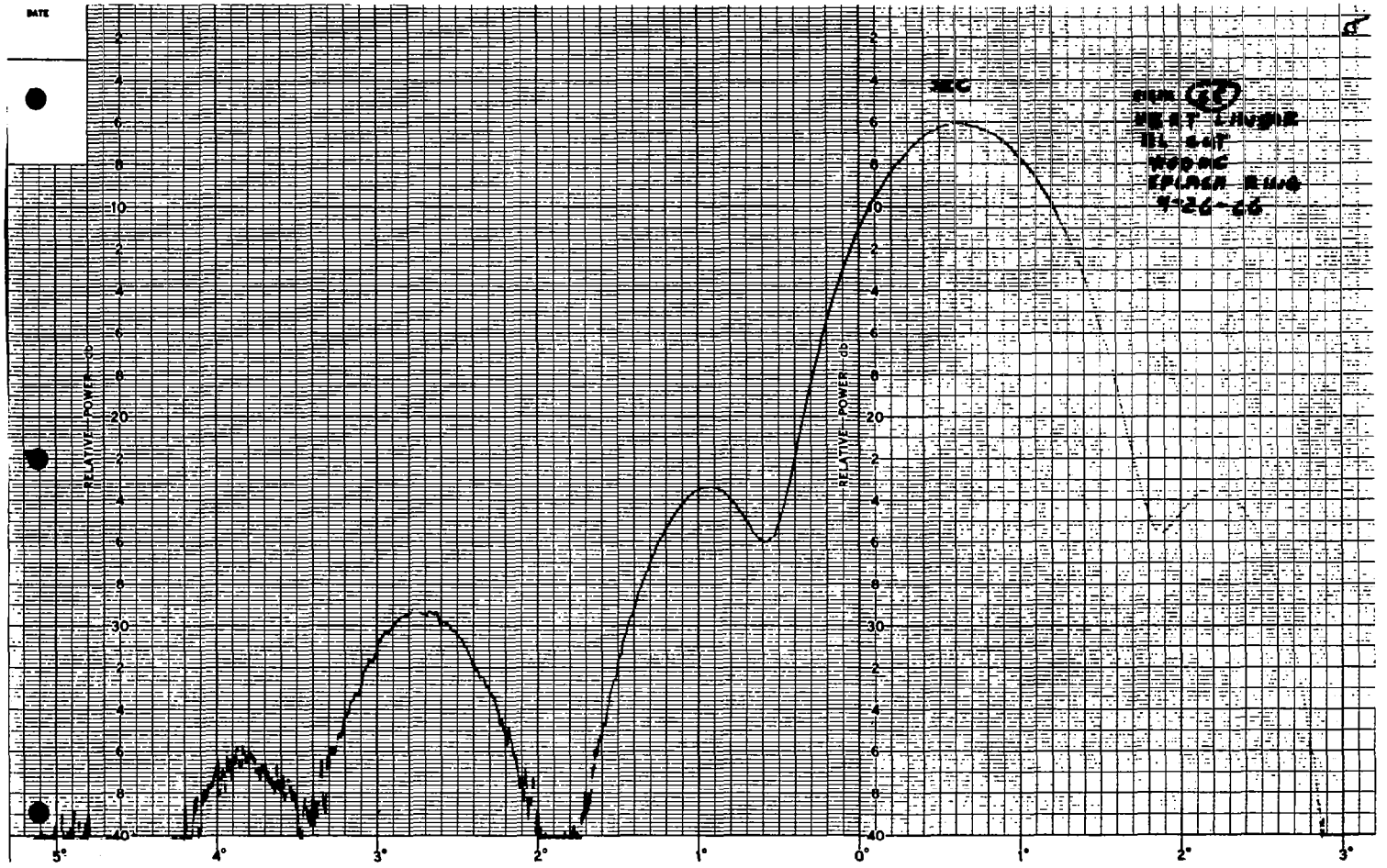


Sum – Vertical Linear – Elevation Cut – 4100 MC

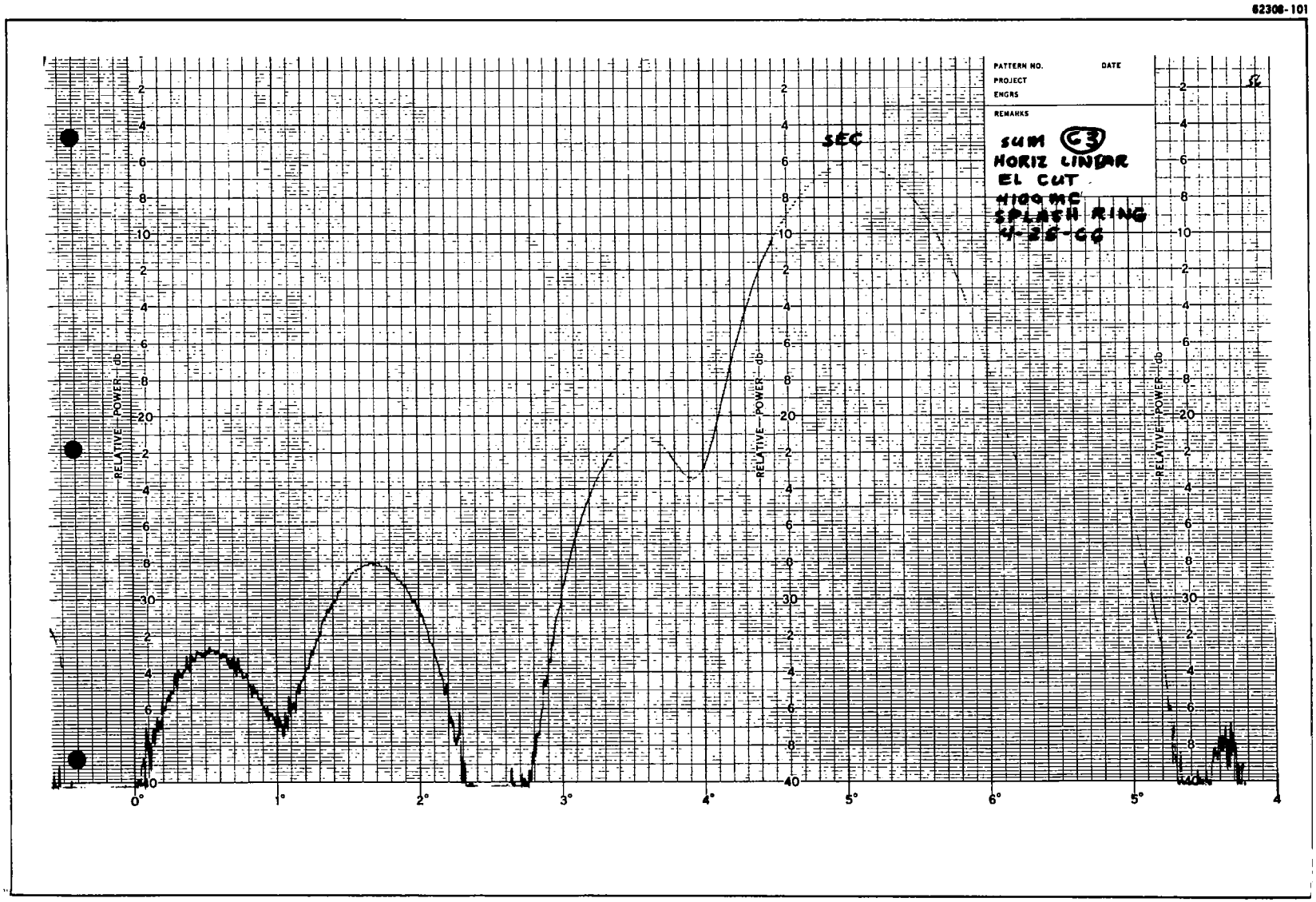


Sum – Horizontal Linear – Elevation Cut – 4100 MC

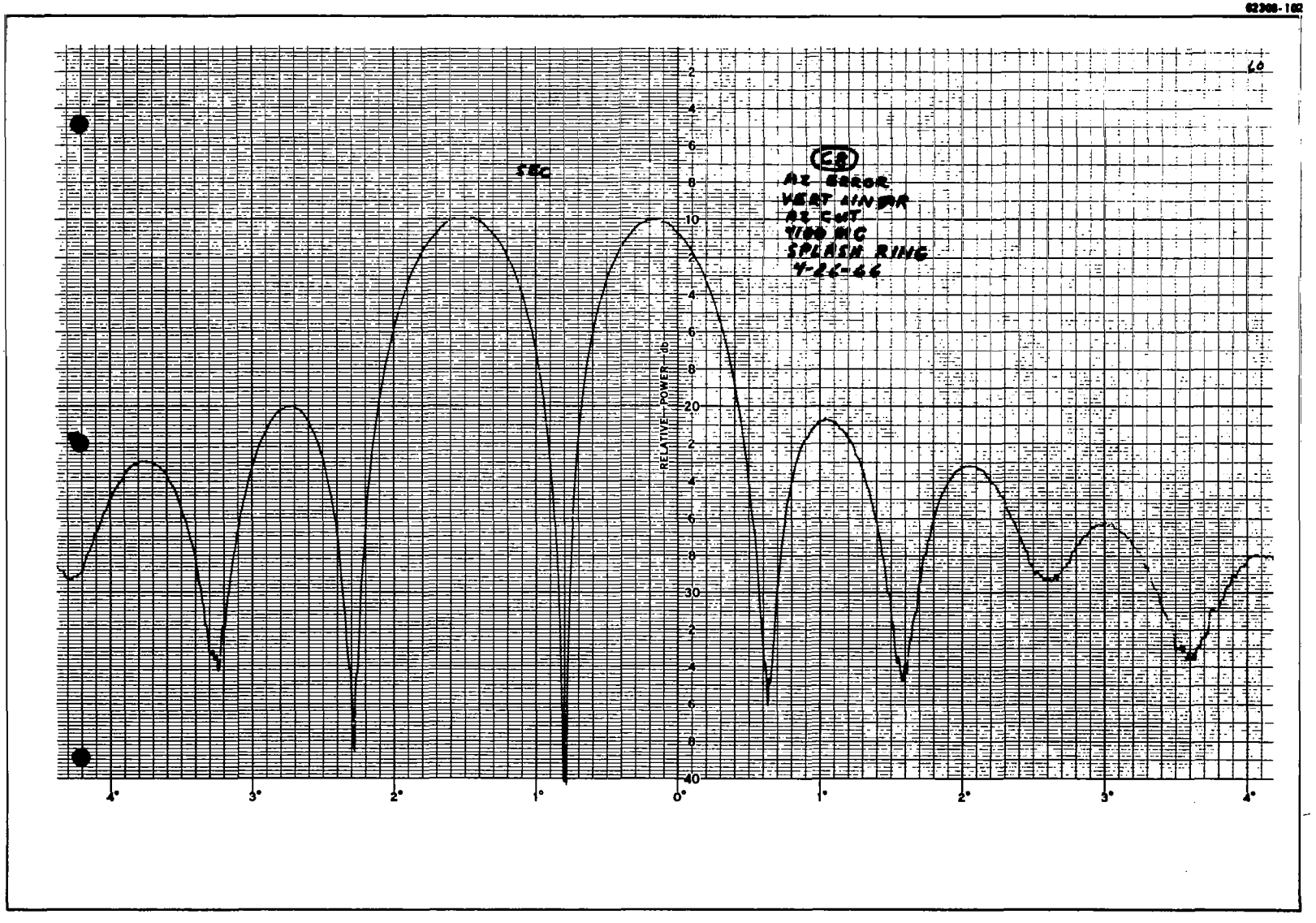


Azimuth Error – Vertical Linear – Azimuth Cut – 4100 MC

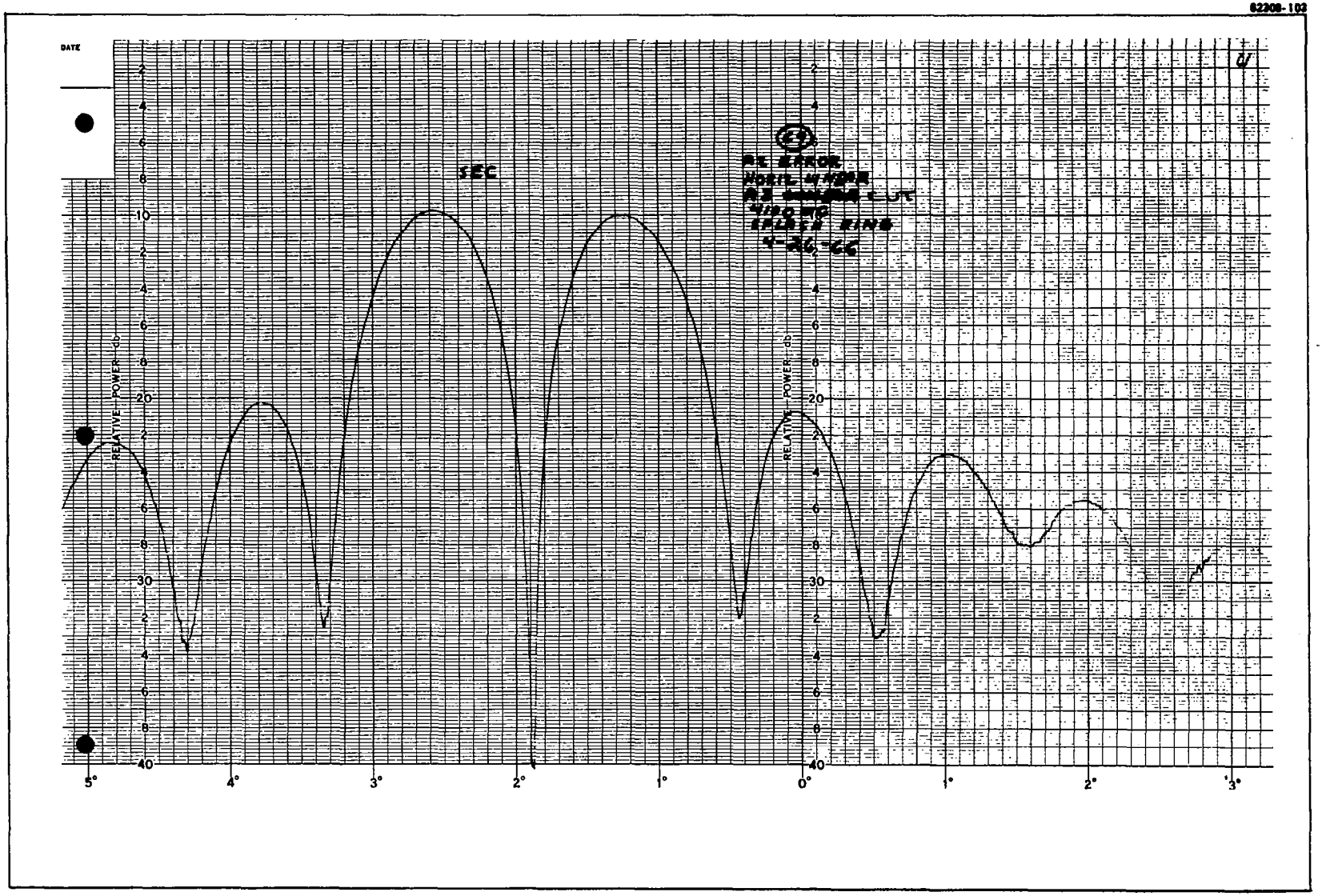


Azimuth Error – Horizontal Linear – Azimuth Cut – 4100 MC

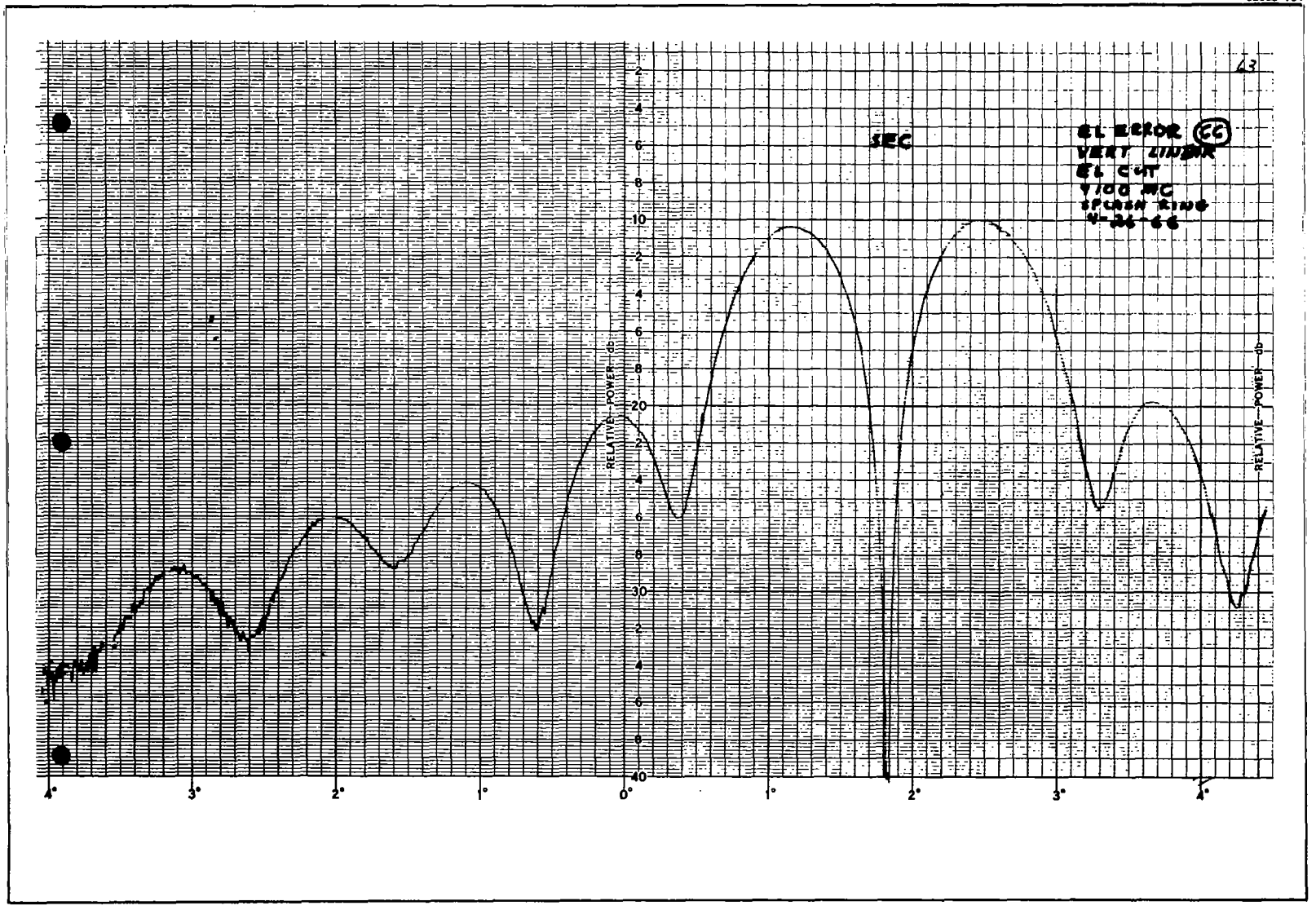


Elevation Error – Vertical Linear – Elevation Cut – 4100 MC

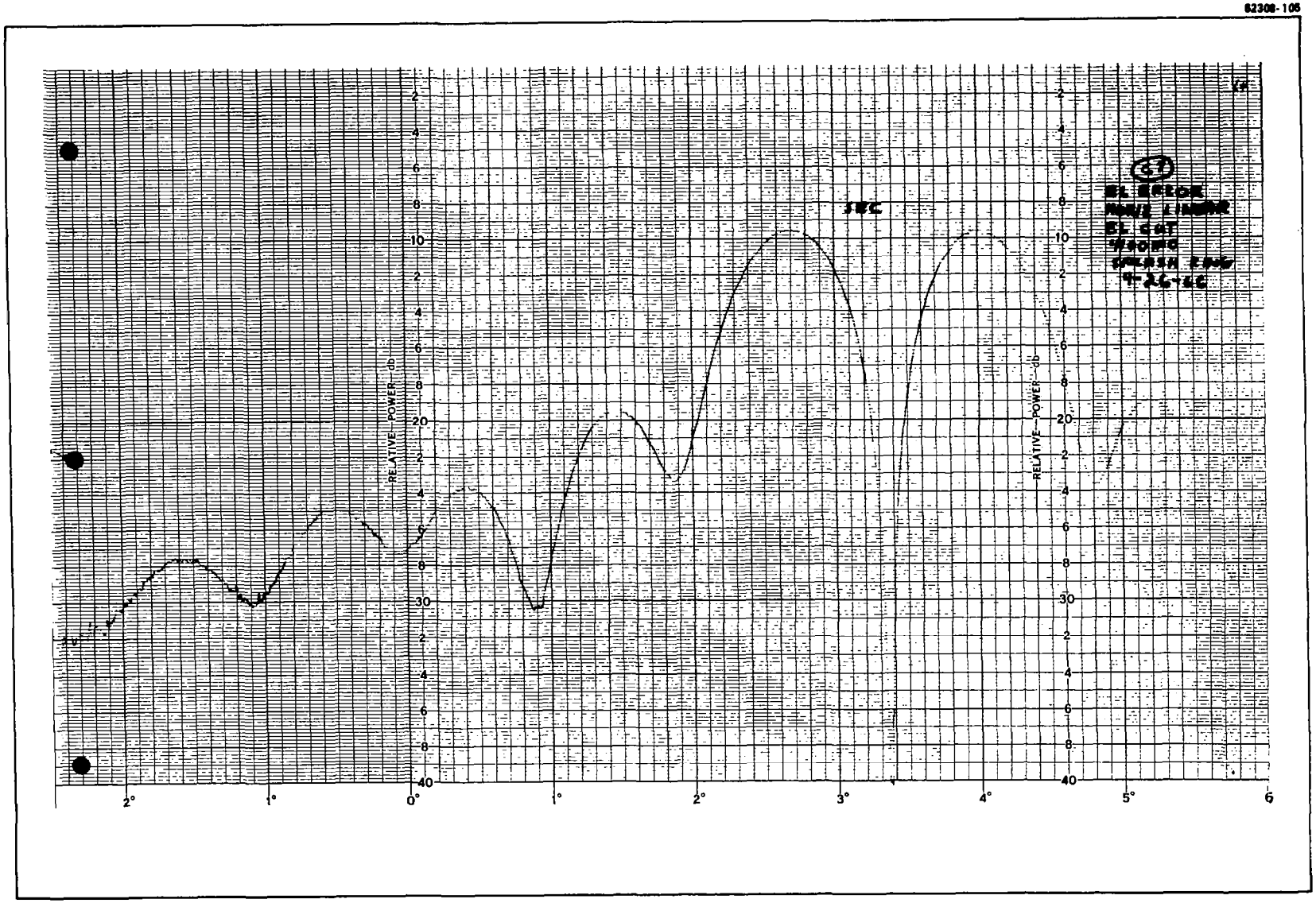


Elevation Error – Horizontal Linear – Elevation Cut – 4100 MC

## 12. DATA SHEET FOR SPERRY REFLEX-KLYSTRON

TUBE DATA SHEET

SPERRY ELECTRONIC TUBE DIVISION
Sperry Rand Corporation
GAINESVILLE, FLORIDA

Tube Type SRV-4403 Ser.No. 115

# TECHNICAL INFORMATION

Date 21 February 1966

## PERFORMANCE CHARACTERISTICS

Resonator Voltage . . . . . 700 volts*

Reflector Voltage Range . . . . . -- to -- volts*

Cathode Current . . . . . 78 milliamperes

Heater Voltage . . . . . 6.3 volts a.c.

Heater Current . . . . . .6 amperes

*Voltages are measured with respect to cathode.

At the above values of voltage and current this tube delivers maximum power output and electronic tuning as tabulated below:

| Frequency (Gc) | Reflector Voltage (Volts) | Power Output (Milliwatts) | Electronic Tuning (½ Power Bandwidth in Mc) | Mod. Sens. Mc/V |
|---|---|---|---|---|
| 30.65 | 262 | 520 | 100 | 1.50 |
| 30.50 | 256 | 600 | 110 | 1.65 |
| 30.35 | 250 | 580 | 110 | 1.85 |

## PHYSICAL CHARACTERISTICS

Flying lead color code

Resonator . . . . Black
Reflector . . . . Orange
*Cathode-Heater. . Yellow
Heater . . . . . Brown
Heater . . . . . ____
*Internal Connection

Output flange mates with waveguide flange UG-599/U

Dimensions . . . See Sperry drawing No. S-1785 A

Tuner turns required to cover tuning range 1-1/4

Turn tuner screw in clockwise direction to decrease frequency.

Be Careful No Stop

Remarks: ____

# 13. ANTENNA NOISE TEMPERATURE VERSUS AZIMUTH ANGLE

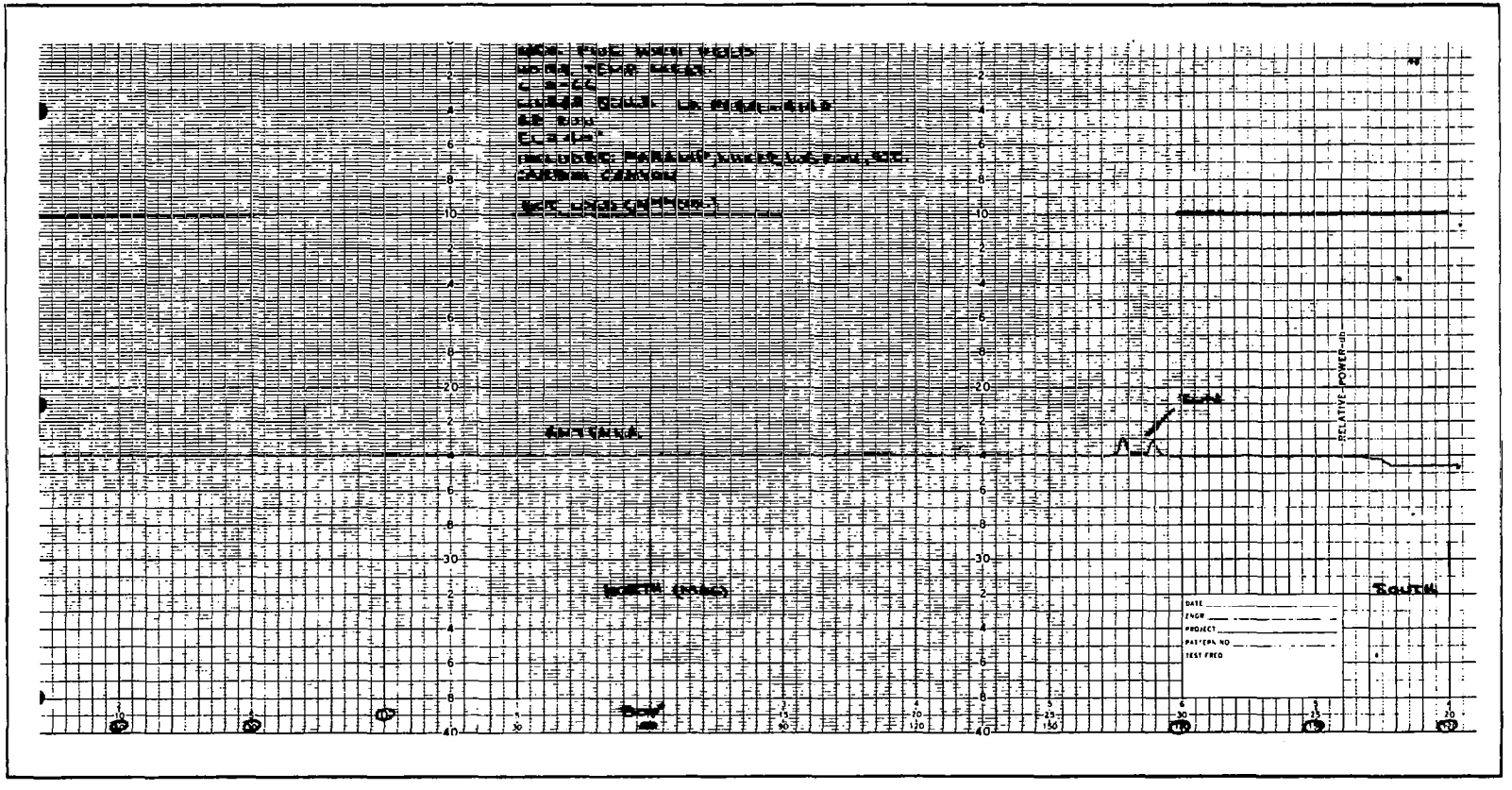


NASA Five Horn Feed Noise Temperature Azimuth Run – Elevation = $40^{o}$

MICROWAVE RELAY STATION
ANTENNA
SCALE
NORTH (0°)
SOUTH
RELATIVE POWER
DATE
ENGR
PROJECT
PATTERN NO
TEST FREQ

13A-2

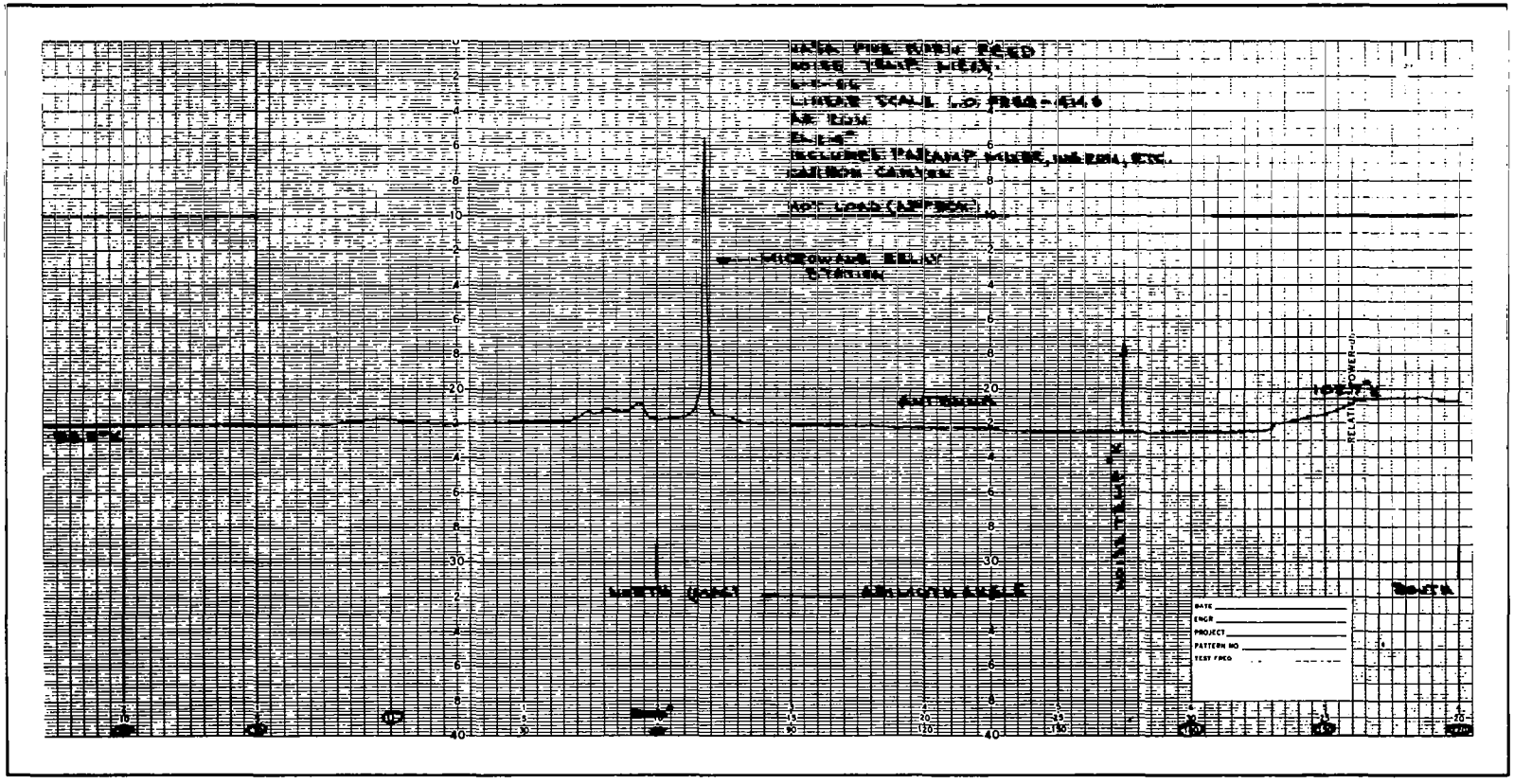


NASA Five Horn Feed Noise Temperature Azimuth Run – Elevation = $4^{o}$

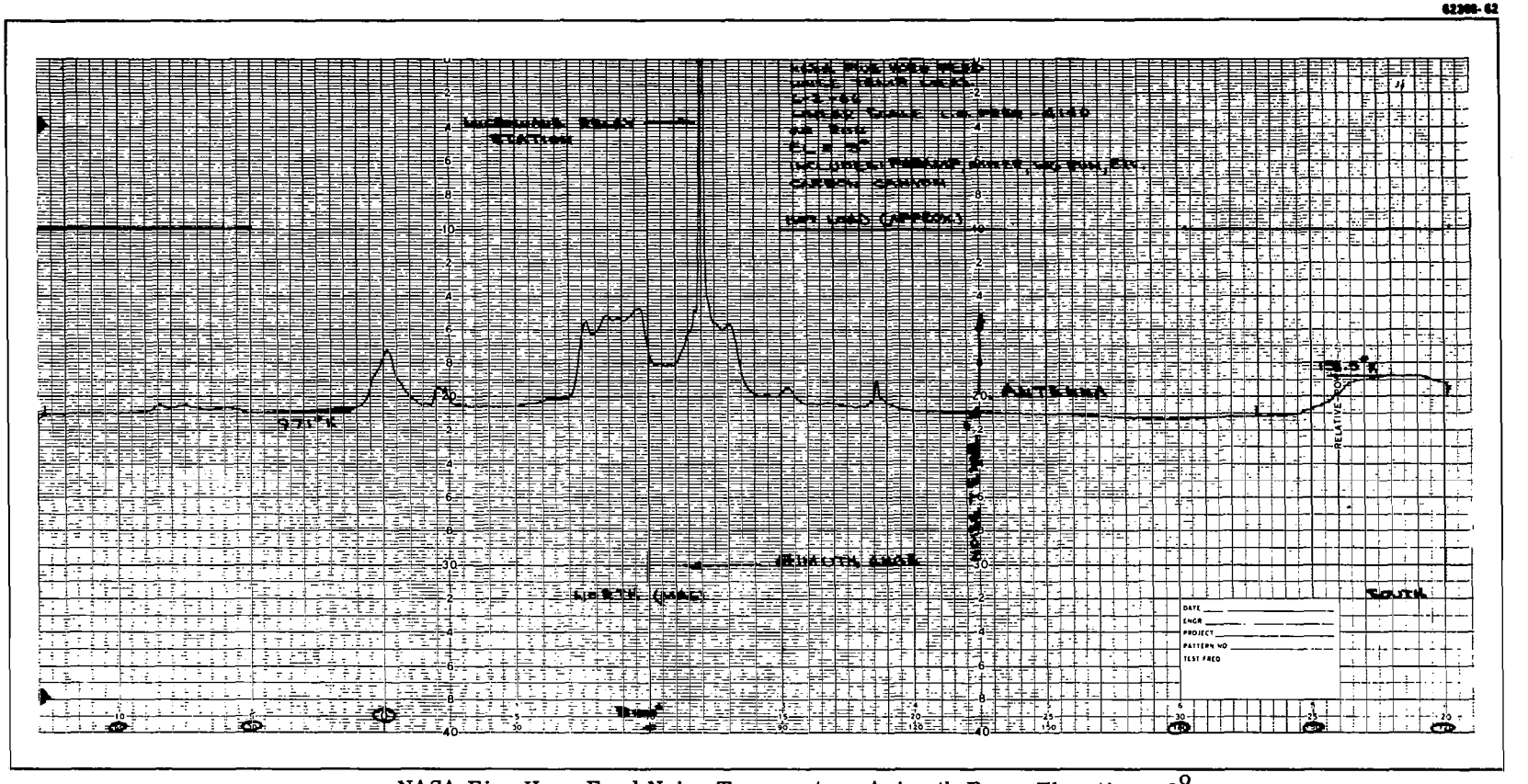


NASA Five Horn Feed Noise Temperature Azimuth Run – Elevation = $3^{o}$

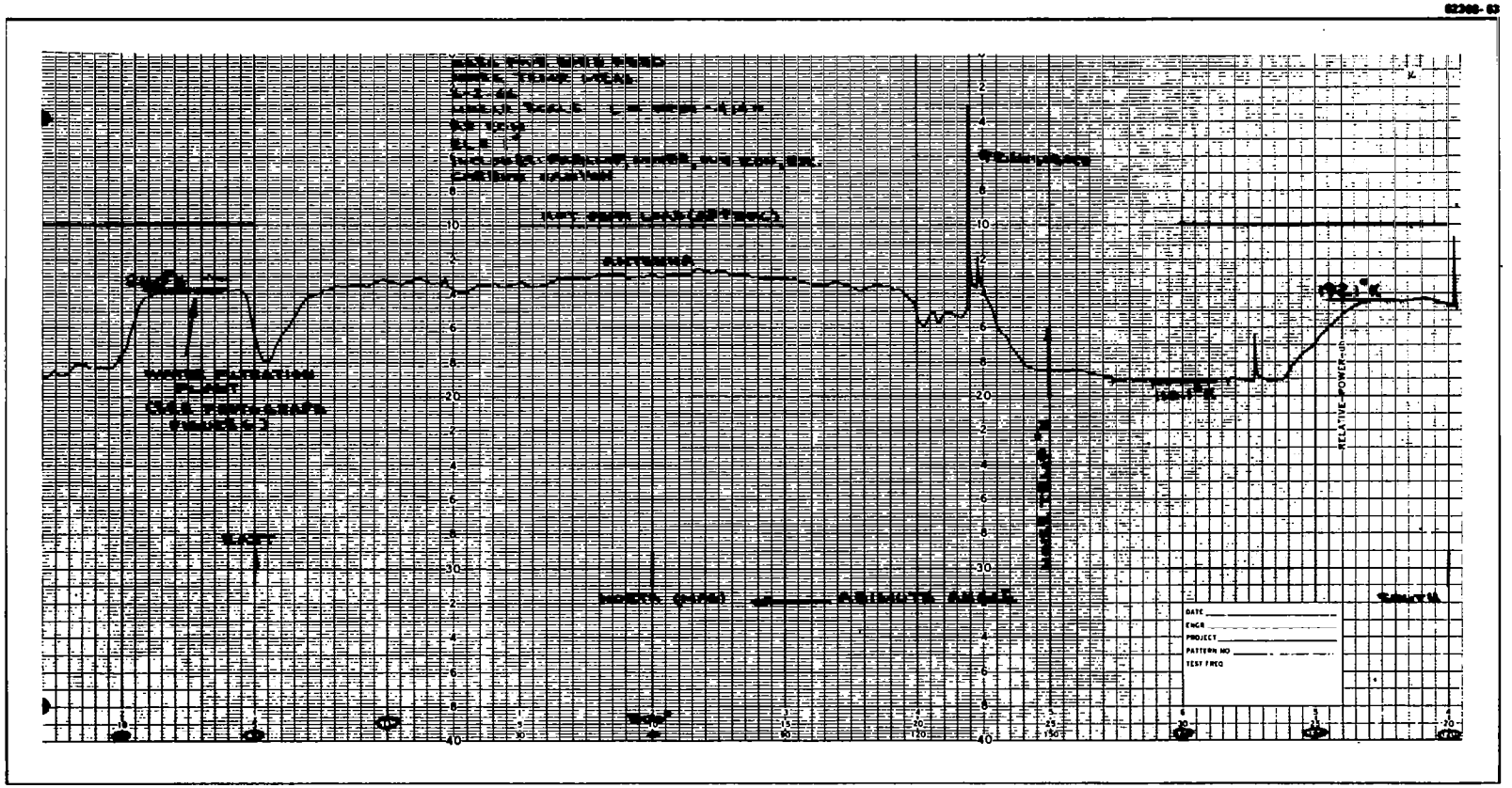


NASA Five Horn Feed Noise Temperature Azimuth Run – Elevation = $1^{0}$

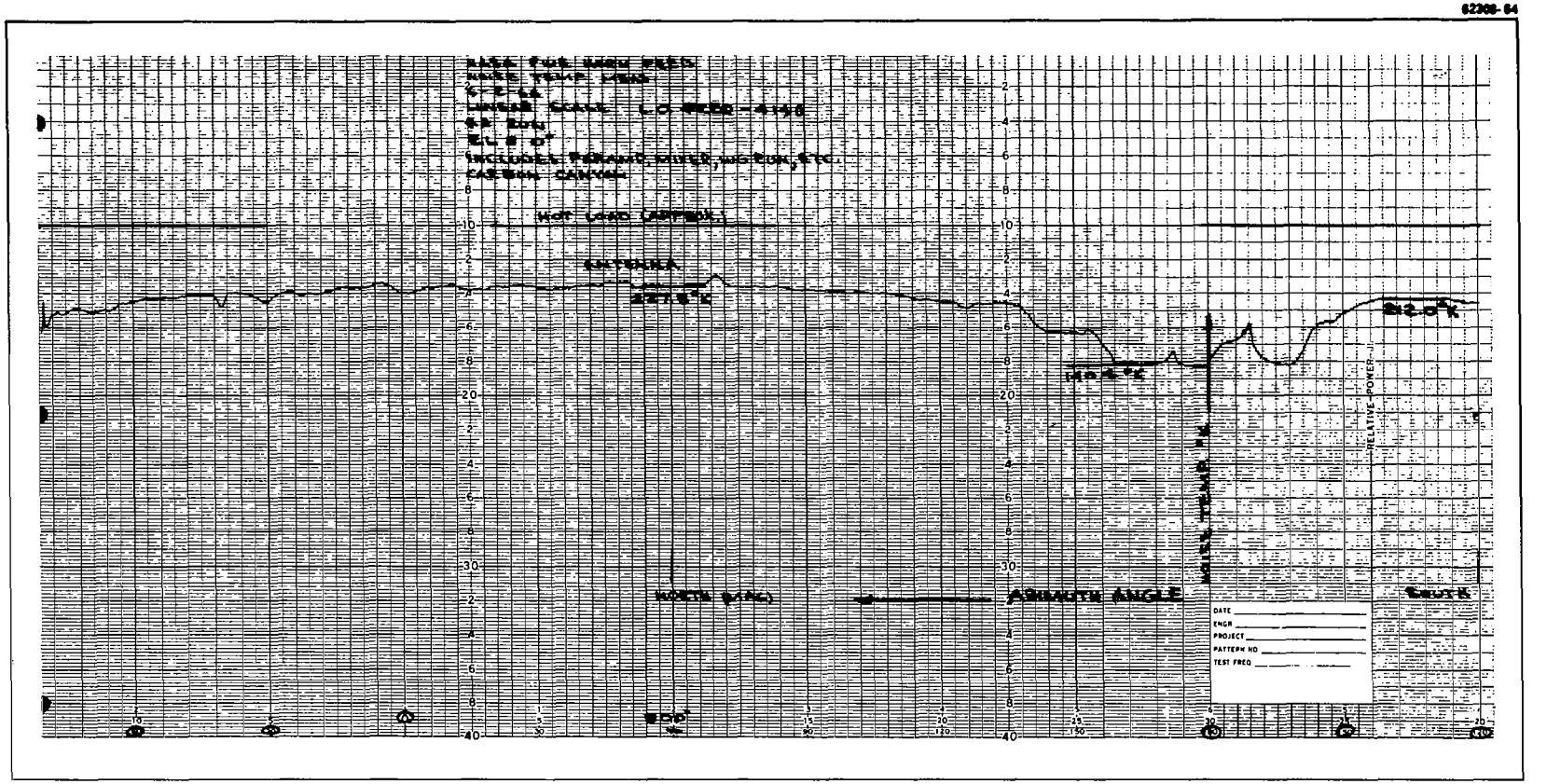


NASA Five Horn Feed Noise Temperature Azimuth Run – Elevation = $0^{o}$

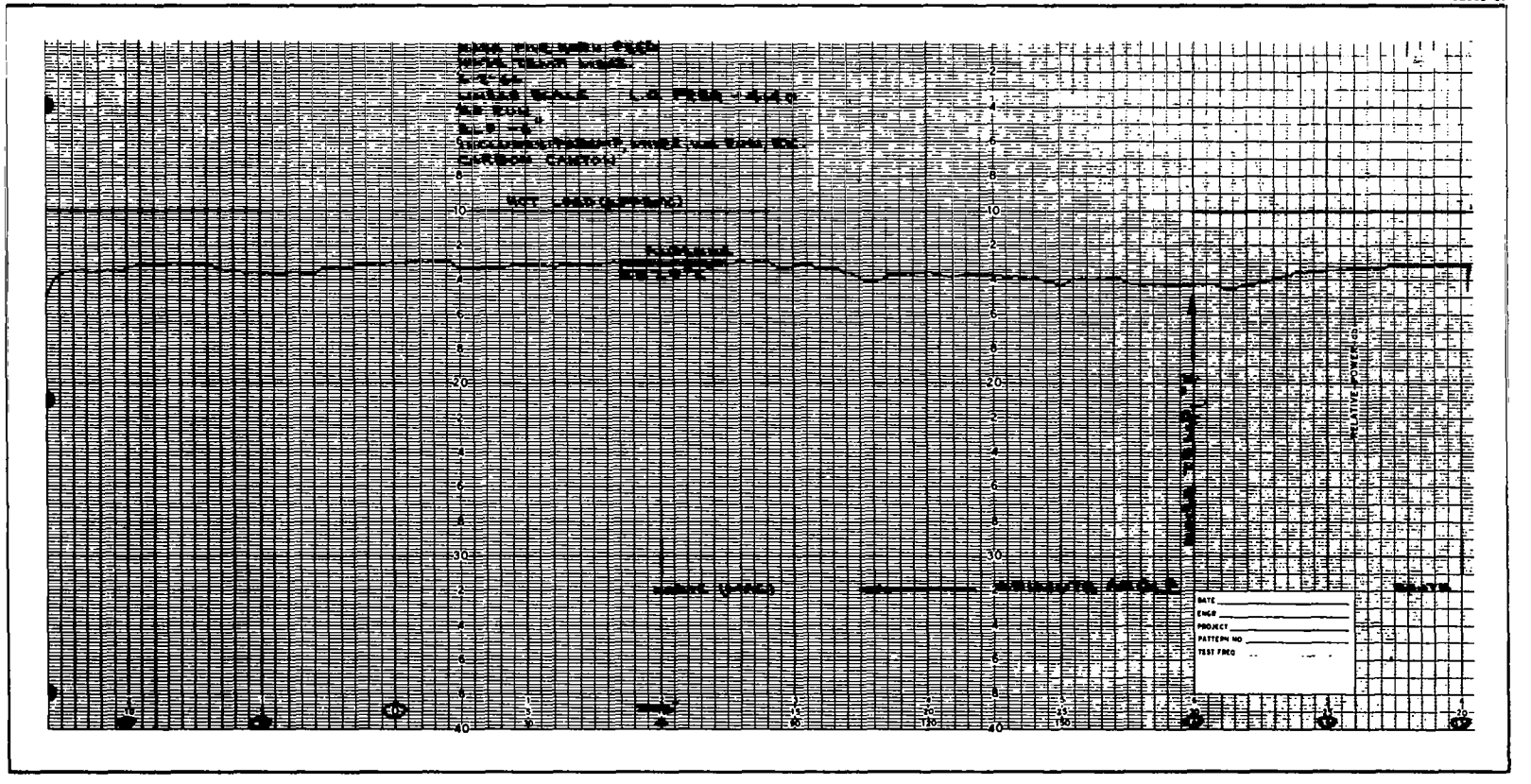

NASA Five Horn Feed Noise Temperature Azimuth Run – Elevation = $-6^{o}$

# 14. ANTENNA NOISE TEMPERATURE VERSUS ELEVATION ANGLE

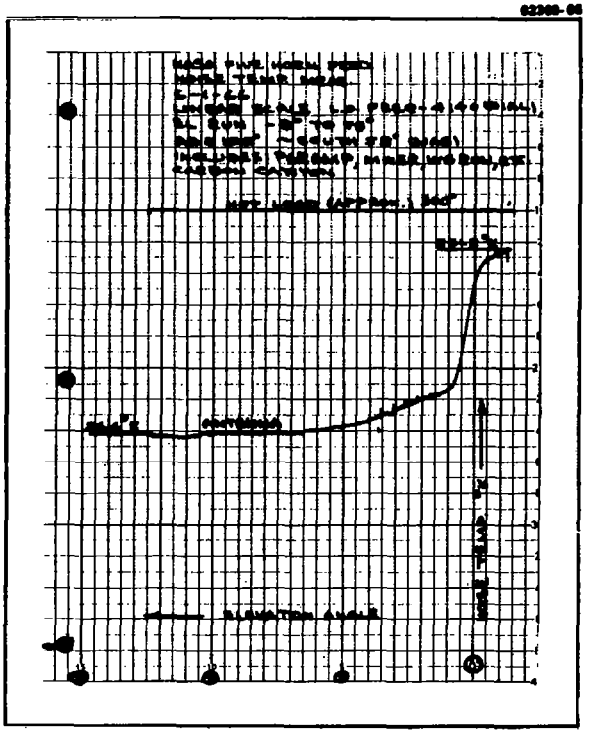

NASA Five Horn Feed Noise Temperature
Elevation Run = -8° to 75°, Azimuth = 120°

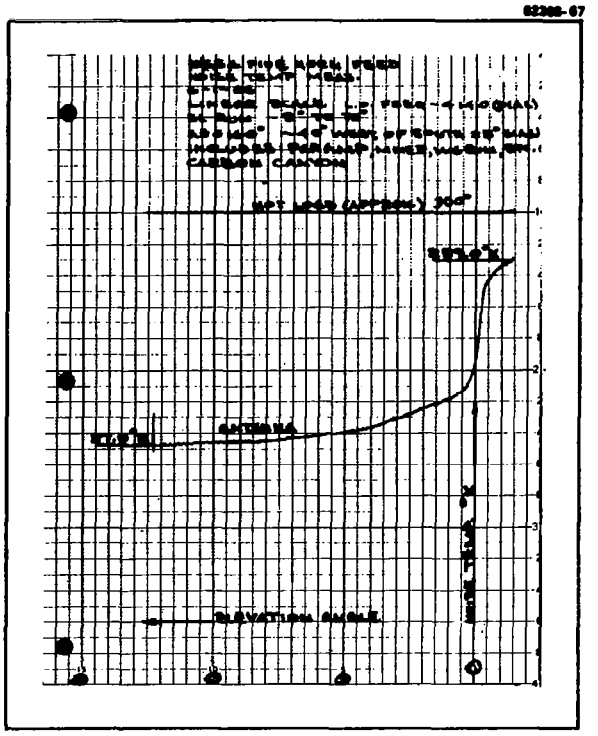

NASA Five Horn Feed Noise Temperature
Elevation Run = -8° to 75°, Azimuth Run = 160°

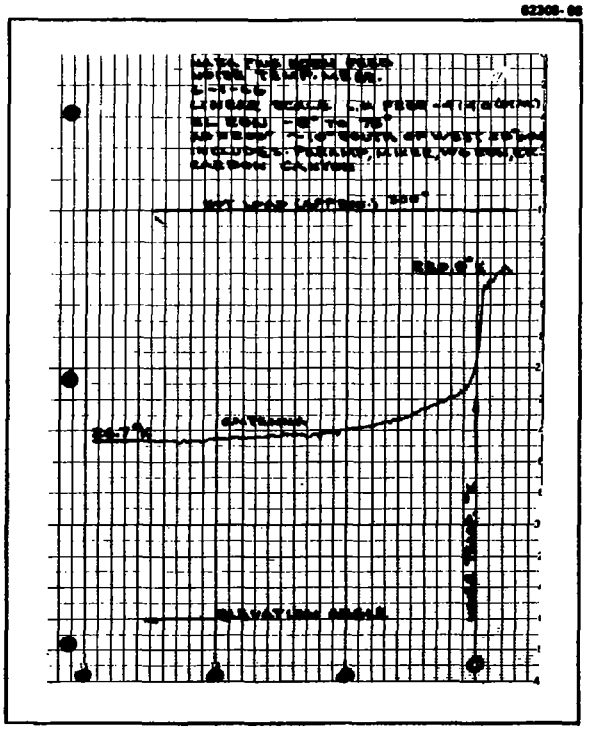

NASA Five Horn Feed Noise Temperature
Elevation Run = -8° to 75°, Azimuth = 200°

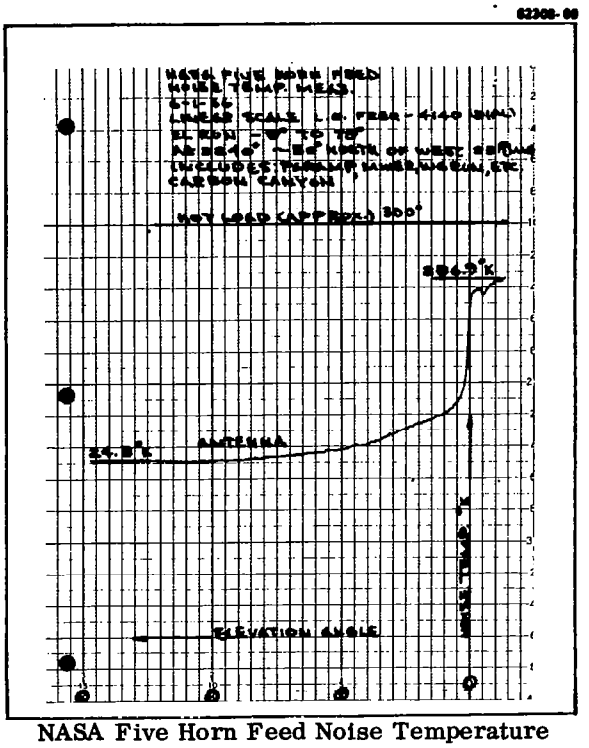

NASA Five Horn Feed Noise Temperature
Elevation Run = $-8^{o}$ to $75^{o}$, Azimuth = $240^{o}$

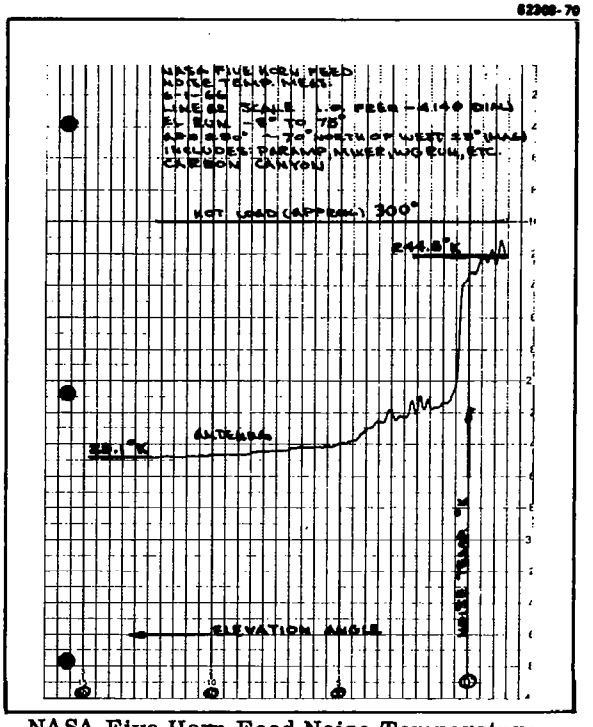

NASA Five Horn Feed Noise Temperature
Elevation Run = $-8^{o}$ to $75^{o}$, Azimuth = $280^{o}$

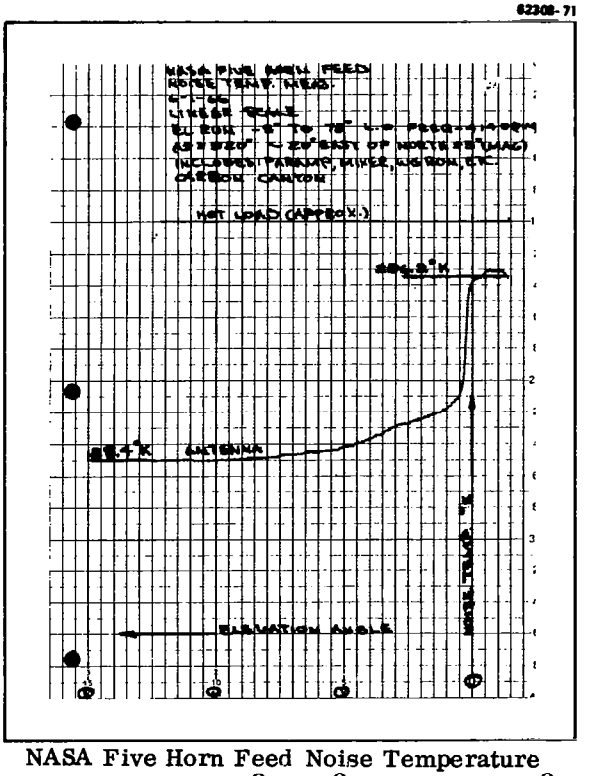

NASA Five Horn Feed Noise Temperature
Elevation Run = $-8^{o}$ to $75^{o}$, Azimuth = $320^{o}$

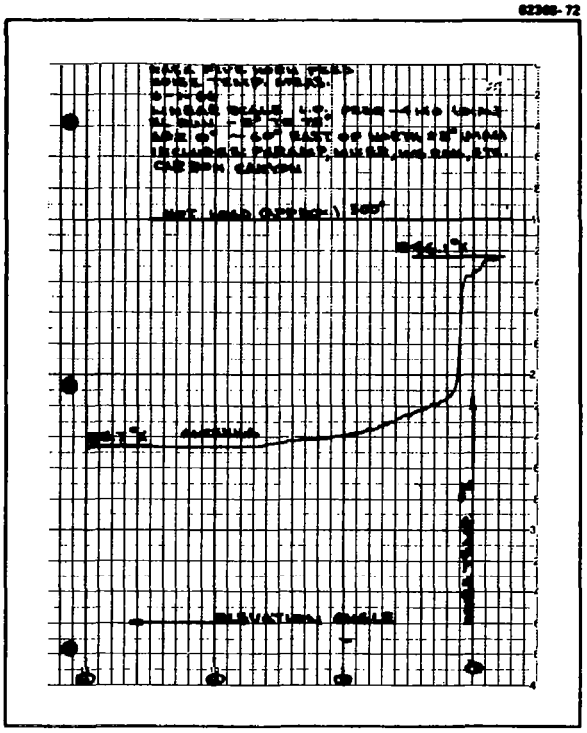

NASA Five Horn Feed Noise Temperature
Elevation Run = $-8^{o}$ to $75^{o}$, Azimuth = $0^{o}$

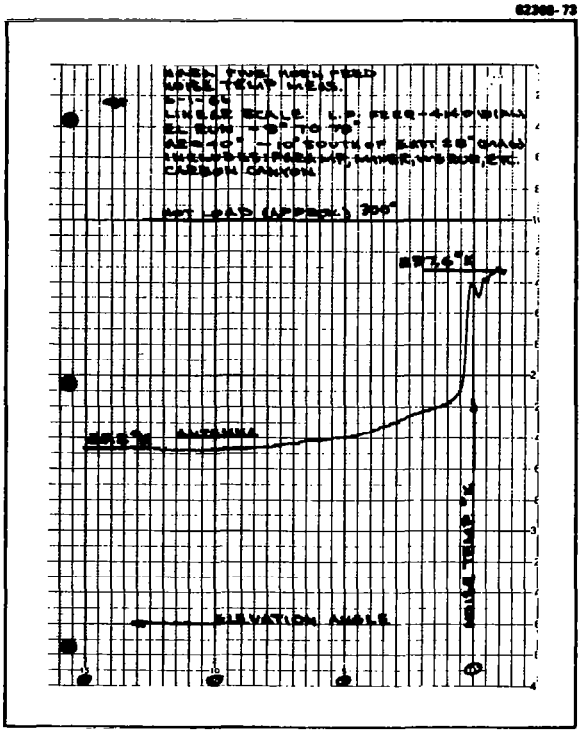

NASA Five Horn Feed Noise Temperature
Elevation Run = $-8^{o}$ to $75^{o}$, Azimuth = $40^{o}$

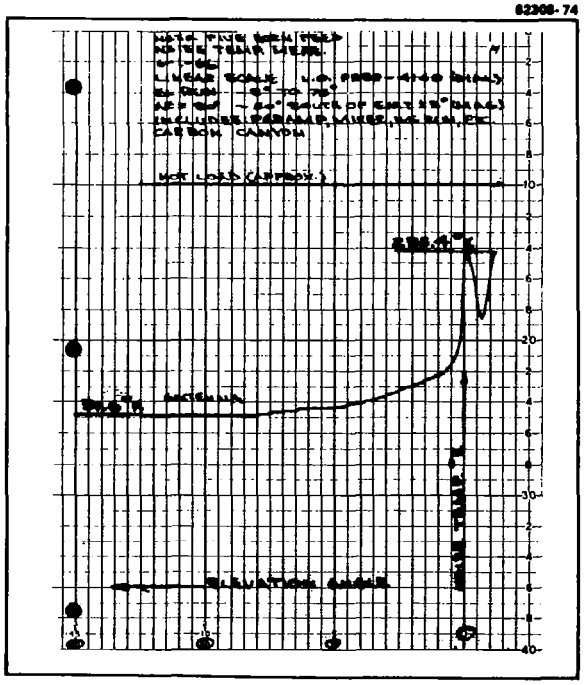

NASA Five Horn Feed Noise Temperature
Elevation Run = $-8^{o}$ to $75^{o}$, Azimuth = $80^{o}$

15. PHOTOGRAPH OF HORIZON AT CARBON CANYON TEST RANGE

66-07-101

Photo #1 – South-Hill Close to Antenna Mount

66-07-106

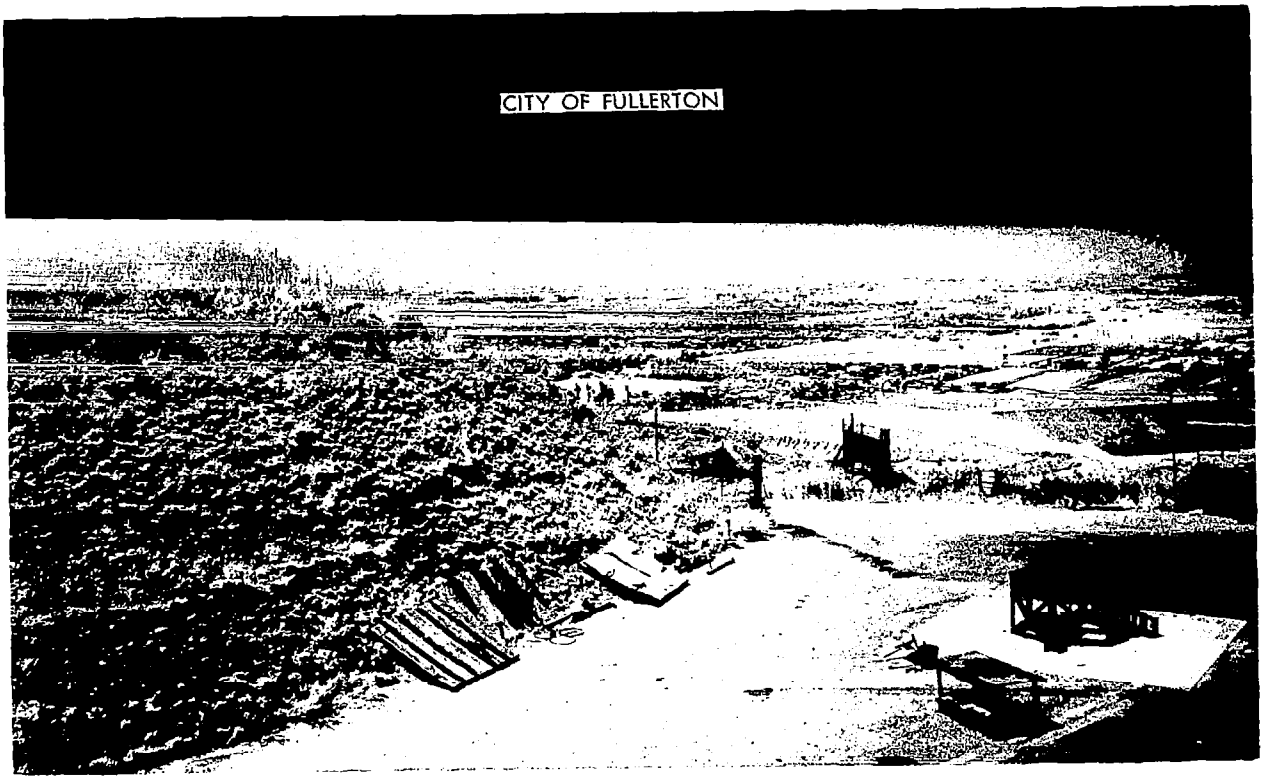


Photo #2 – 40° West of South – Looking Over City of Fullerton

66-07-109

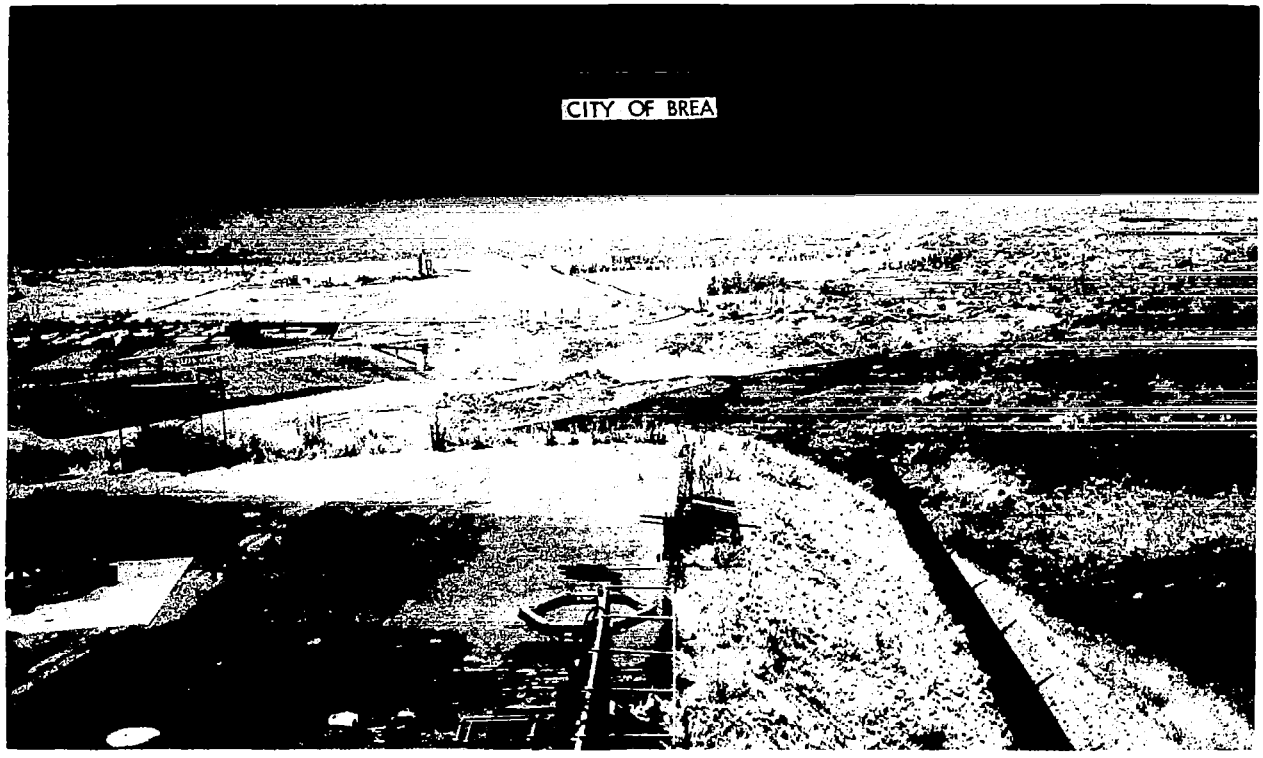


Photo #3 – 10° South of West – Looking Over City of Brea

66-07-103

Photo #4 – 30° North of West – Entrance to Carbon Canyon

66-07-117


Photo #5 – 20° East of North – Looking Down Carbon Canyon

66-07-108


Photo #6 – 70° North of West – Looking Across Canyon

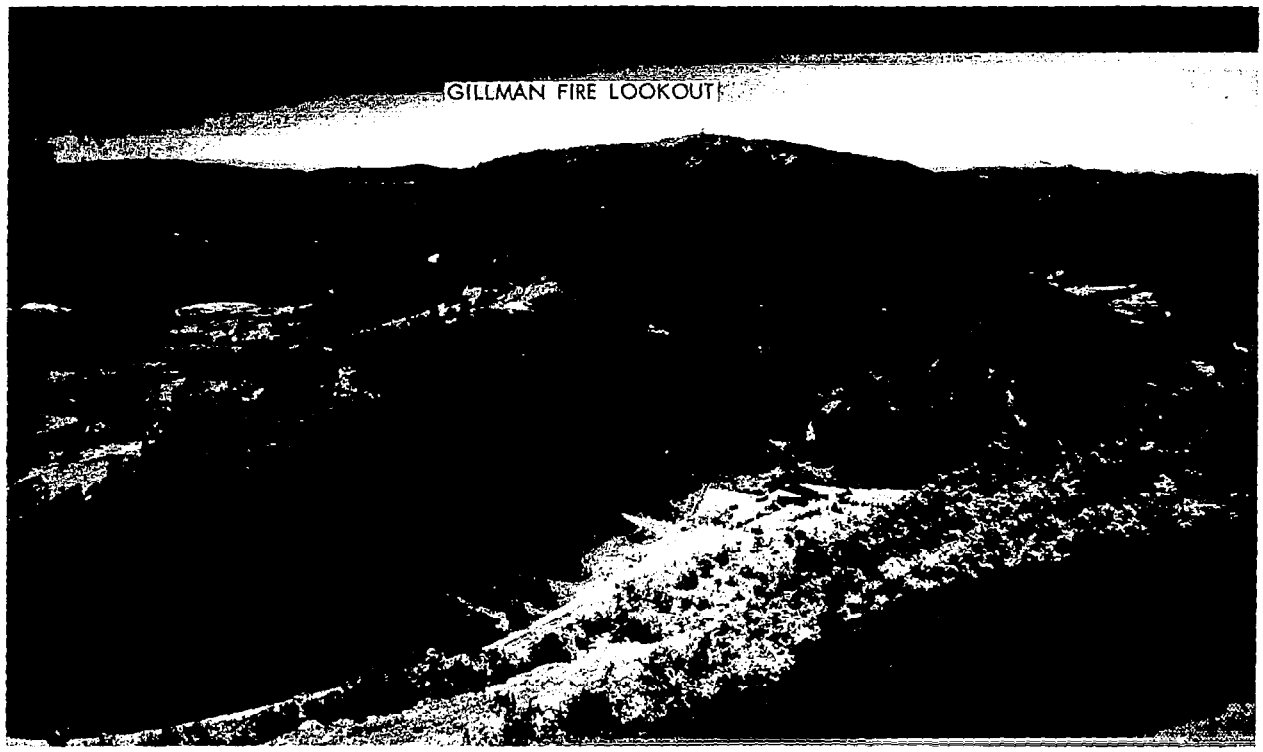


Photo #7 – 60° East of North – Looking Towards San Bernardino


Photo #8 – 10° South of East – Looking in the Direction of Corona

Photo #9 – 50° South of East – Looking Over City of Yorba Linda